



ALMA MATER STUDIORUM DI BOLOGNA
FACOLTÀ DI SCIENZE MM.FF.NN.

Tesi di Laurea Magistrale in
ANALISI E GESTIONE DELL'AMBIENTE

Study of a Wind-Wave Numerical Model and its
integration with an Ocean and an Oil-Spill
Numerical Models

Relatore
Prof.ssa Nadia Pinardi

Candidato
Diego Bruciaferri

Correlatori
Dott.ssa Michela De Dominicis
Dott. Francesco Trotta

Anno Accademico 2012/2013

*Given for one instant an intelligence
which could comprehend all the forces
by which nature is animated, ...
to it nothing would be uncertain,
and the future as the past
would be present to its eyes.*

Laplace, Oeuvres

Desidero ringraziare mio padre, mia madre e i miei fratelli che hanno sempre creduto in me e hanno sempre supportato le mie scelte.

Desidero inoltre ringraziare la Prof.ssa Nadia Pinardi, che, con il suo incoraggiamento e la sua contagiosa passione per la fisica e il mare, non ha mai smesso di motivarmi nel superare gli scogli piu' difficili incontrati durante questo lavoro.

Un ringraziamento speciale va alla Dott.ssa Michela De Dominicis, al Dott. Luca Giacomelli e al Dott. Francesco Trotta, senza l'aiuto dei quali questo lavoro non avrebbe potuto essere portato a termine.

Un grazie poi a tutti i Prof.ri del mio corso di Laurea, per l'entusiasmo che hanno messo nelle loro lezioni e per i loro insegnamenti.

Un grazie a Claudia, Giulia, Emanuela, Augusto e a tutti i ragazzi che hanno frequentato i laboratori del SINCEM, perche' tutti mi hanno lasciato qualcosa.

Un grazie poi va ai miei compagni di corso, al 'cruccho' Matteo, al 'terroncello' Roberto, a Francesco, Riccardo, Michela, Manuela, Caterina e tutti gli altri, per i bei due anni passati insieme.

Grazie.

Abstract

The ability to represent the transport and fate of an oil slick at the sea surface is a formidable task. By using an accurate numerical representation of oil evolution and movement in seawater, the possibility to assess and reduce the oil-spill pollution risk can be greatly improved. The blowing of the wind on the sea surface generates ocean currents due to turbulent stress and ocean waves, which give rise to wave-induced velocities that are known as Stokes' Drift velocities. The Stokes' Drift transport associated to a random gravity wave field is a function of the wave Energy Spectra that statistically fully describe it and that can be provided by a wave numerical model. Therefore, in order to perform an accurate numerical simulation of the oil motion in seawater, a coupling of the oil-spill model with a wave and turbulence current forecasting model is needed. In this Thesis work, the coupling of the MEDSLIK-II oil-spill numerical model with the SWAN wind-wave numerical model has been performed and tested. In order to improve the knowledge of the wind-wave model and its numerical performances, a preliminary sensitivity study to different SWAN model configuration has been carried out. The SWAN model results have been compared with the ISPRA directional buoys located at Venezia, Ancona and Monopoli and the best model settings have been selected. Then, high resolution turbulence currents provided by a relocatable model (SURF) have been used to force both the wave and the oil-spill models and its coupling with the SWAN model has been tested. The trajectories of four drifters have been simulated by the coupled wave-current and oil-spill model and results have been compared with the real drifters paths.

Contents

1	Introduction	9
1.1	Wave Modeling: the state-of-the-art	14
1.2	The Oil-spill models state-of-the-art	20
2	Numerical Modeling of Surface Waves	25
2.1	Linear Wave Theory	25
2.1.1	High Frequency Waves in The Ocean	26
2.1.2	The Wave Equation and Wave Parameters	27
2.1.3	Surface Gravity Waves	30
2.1.4	Wave Energy	35
2.1.5	Fluid Particle Path	37
2.1.6	Stokes' Drift	39
2.2	Statistical Wave Theory	43
2.2.1	Representative Wave Parameters	44
2.2.2	Wind Waves as a Stochastic Process	48
2.2.3	The Random Phase-Amplitude model	51
2.3	Description of the Wind-Wave SWAN Numerical Model	63
2.3.1	Wind-Wave Models	63
2.3.2	Spectral action balance equation	65
2.3.3	Sources and sinks	67
2.3.4	Numerical Schemes	78
3	Wave Model Experiments and Results	83
3.1	Sensitivity Experiments	84
3.1.1	Model Setup	84
3.1.2	Sensitivity Experiments to Numerical Parameters	97
3.1.3	Sensitivity Experiments to the Input Fields (Wind and Currents)	103
3.1.4	Sensitivity Experiments to Wave Physical Processes	109
3.2	SWAN Coupling with Ocean Relocatable Model	125

3.2.1	SURF Relocatable Model	125
3.2.2	NEMO-SWAN Coupling Experiments	129
3.3	SWAN Coupling with the Oil-Spill Model	140
3.3.1	MEDSLIK-II Model	140
3.3.2	Stokes Drift Calculation	144
3.3.3	SWAN-MEDSLI-II Coupling Experiments	157
4	Conclusions	171
A	Potential Velocity	185
A.1	Line Integral	185
A.2	Potential Velocity	187
B	Kelvin Theorem	189
C	Stochastic Processes	193

Chapter 1

Introduction

An oil spill is the release of any oily substance into the environment due to human activity, and is a form of pollution. The term is usually applied to marine oil spills, where oil is usually petroleum released into the ocean or coastal waters, and in this Thesis will be considered only the latter.



Fig. 1.1: The oil slick in the Gulf of Mexico is seen from a helicopter. (by Rick Loomis, Los Angeles Times, May 6, 2010)

They may be due to releases of crude oil from tankers, offshore platforms, drilling rigs and wells, as well as spills of refined petroleum products (such as gasoline, diesel) and their by-products or heavier fuels used by large ships

such as bunker fuel.

Oil spills endanger public health, imperil drinking waters, devastate natural resources, and disrupt the economy and when they occur human health and environmental quality are put at risk and every effort must be made to prevent or to clean them up promptly once they occur [75].

The ability to represent the transport and fate of an oil slick at the sea surface is a formidable task: by an accurate numerical representation of oil evolution and movement in seawater, the possibility to assess and reduce the oil-spill pollution risk can be greatly improved.

Many factors affect the motion and transformation of the slick. The most relevant of these are the meteorological and marine conditions at the air-sea interface (wind, waves and water temperatures); the chemical characteristics of the oil; its initial volume and release rates; and, finally, the marine currents at different space scales and timescales [25]. Therefore oil spill management strategies need to be developed together with the improvement of meteorological, ocean and wave forecasting models.

The first time that pioneering examples of oil spill response systems allowed operators to develop a response strategy rather than react only to observed information were during the Braer oil spill (Shetland Islands, UK, 1993) [82] and the Erika oil spill (Brittany coast in the Bay of Biscay, France, 1999) [22]. Further examples of operational forecasting system for developing proper response strategies to oil spill emergencies were available during the Prestige oil spill crisis (Galicia coast, Spain, 2002) [14] [13].

In the Mediterranean Sea, an oil-spill decision-support system was developed during the largest oil-release accident in the Eastern Mediterranean, the Lebanese oil-pollution crisis, which occurred in mid-July 2006 [20].

During the recent largest accidental marine oil spill in the history of the petroleum industry, effective oil spill monitoring and modeling systems were critical to the rapid responses achieved for the Deepwater Horizon event (Gulf of Mexico, 2010).

The wind induces currents in the ocean that are produced by tangential turbulent stresses: the classical example of such currents are called after Ekman, in addition to the geostrophic flow field that is generated by Ekman vertical velocities. These currents are normally generated by hydrodynamic models at the spatial scales of few km.

The blowing of the wind on the sea surface generates also ocean waves, which give rise to the transport of any kind of floating object placed on the sea surface in the direction of their propagation. This physical process is known as *Stokes' Drift*, in honor of George G. Stokes who was the first to identify and describe in 1847 this non-linear process [97]. *Stokes' Drift* velocities affect also the motion of oil-slicks.

As it will be shown in this work, the *Stokes' Drift* transport associated to a *random gravity wave field* is a function of the wave *Energy Spectra* that statistically fully describe it. Therefore, in order to perform an accurate numerical simulation of the oil motion in seawater, a coupling of the oil-spill model with a wave forecasting model is needed.

In this Thesis work, the coupling of the SWAN wind-wave numerical model with an hydrodynamic and the MEDSLIK-II oil-spill numerical models has been performed and tested. This research activity has been carried out at the SINCEM (*SImulazioni Numeriche del Clima e degli Ecosistemi Marini*) Laboratory of Department of Physics and Astronomy of the University of Bologna, with the collaboration of the *Istituto Nazionale di Geofisica e Vulcanologia* (INGV), Bologna section.

MEDSLIK-II is an oil spill model designed to predict the transport and weathering of an oil spill or to simulate the movement of a floating object and its code is a freely available community model which can be downloaded from <http://gnoo.bo.ingv.it/MEDSLIKII>.

SWAN is a third generation spectral wave model developed by Booij et al. [10] which can be applied in a wide range of coastal applications, being effective from high resolution coastal areas up to quasi oceanic scales.

Two kind of hydrodynamic models have been used in this Thesis to simulate turbulent ocean currents such as Ekman and geostrophic velocities.

Following *De Dominicis et al.* [24], high resolution and accurate forecasts of the ocean currents provided by a *Relocatable* ocean model greatly improve

the quality of the operational oceanography products. The Relocatable modeling method focus on the rapid implementation of a model nested into a coarser scale model and it aims to be a valuable tool to be used in support to any Decision Support System which might need hydrodynamics and wave data for short time forecasts and applications, such as oil spill monitoring, search and rescue operations, ship routing, ship traffic monitoring, etc.

In this Thesis work a new model, SURF (Structured Unstructured Relocatable ocean model for Forecasting) model, has been partially developed coupling SWAN with NEMO (Nucleus for European Modelling of the Ocean) model.

NEMO has been initially developed at the Laboratoire d’Oceanographie Dynamique et de Climatologie (LODYC) by the ‘Istituto Pierre Simon Laplace’ (IPSL), and now is run by a European Consortium created in 2008 between *CNRS* (France), *Mercator-Ocean* (France), *NERC* (UK), *UKMO* (UK) and, since, 2011 *CMCC* (Italy) and *INGV* (Italy).

NEMO is a finite differences free surface three-dimensional model; it solves the oceanographic approximated Navier-Stokes equations and it uses the following assumptions: the fluid is incompressible, the Boussinesq approximation, the Earth is spherical and the vertical component of the motion equation can be given by the simple hydrostatic balance. The NEMO code provides many different options to define the numerical grid, the boundary conditions, the equation of state, the parameterization of small-scale turbulent processes and numerical schemes for spatial and temporal discretization of the primitive equations. For a complete description of all the possible physical and numerical configurations allowed by NEMO see [66].

SURF is under development at SINCEM for TESSA project and there is only Technical documentation [100] [12].

This Thesis is organized as follows:

- In **Chapter 1**, after this brief introduction, a review of *the-state-of-the-art* of the wind-wave and oil-spill numerical models is given.
- In **Chapter 2**, the *Linear and Statistical Theories* developed to mathematically and physically describe ocean wind waves are exposed. A complete description of the SWAN wind-wave model is given, too.
- In **Chapter 3** the numerical experiments performed in this Thesis work are described.
- In **Chapter 4**, the conclusions are exposed.

1.1 Wave Modeling: the state-of-the-art

Wave modeling is involved with two aspects of human knowledge: the theory, often touching basic principles from more fundamental sciences, and practical applications.

In the last 60 years fundamental advances in wave modeling have taken place, followed by periods of application and a proliferation of small scale improvements. Unavoidably, the rate with which the knowledge advance tends to decrease.

The basic principles of wave modeling theory have been described and fully accepted by the scientific community, and, at the this time, wind wave models are able to provide satisfactory results on a large scale. Indeed, the bias and scatter index of the operational ECMWF global wave model are an impressive 4% and 0.11 (statistics of the first four months of 2006), or even lower once the error of the instrument we compare with, in the above case the altimeter, is taken into account [98].

Better results are occasionally achieved by local scale modeling, demonstrating that the improvements in the definition of the surface wind fields is substantial to have better simulations [98].

Although wave models are able to evaluate with good accuracy the integral properties of the sea (significant wave height, period and direction), results are definitely less impressive once we look at the shape of the one- and, more so, two-dimensional spectra. Peaks and extreme conditions are frequently not well reproduced, and not only because in these cases the meteorological input is not good enough. In such conditions, the validity of the physical assumptions needed to develop sea wave theories are often stretched to their limits. In the present state, wind wave models are still based on a substantial degree of empiricism, that unavoidably is due to fail at a more or less large degree once the usual range of conditions is exceed [98].

In this section, a picture of the present situation of the wind wave models state-of-the-art is given, following [98].

Wind-Wave generation: The problem of the growth of ocean waves by wind and the consequent feedback of the ocean waves on the wind has led to quite some controversy and many debates in the literature. it is an extremely

difficult problem because it involves the modelling of a turbulent airflow over a surface that varies in space and time. Although there has been much progress in understanding turbulence over a flat plate in steady-state conditions, modelling attempts of turbulent flow over (nonlinear) gravity waves are only beginning and there is still a considerable uncertainty regarding the validity of these models.

In addition, considering an experimental point of view, it is not an easy task to measure growth rates of waves by wind.

The commonly adopted cause of wave growth is the work done by the pressure on the surface. This assumption seems plausible in view of the work by *Miles* [72]. Miles' quasi-laminar theory was the first model to give a plausible explanation of the growth of waves by wind. Basically, this wave generation by wind mechanism is a resonant interaction of the gravity waves with a plane-parallel flow. Resonance occurs at a critical height z_c which follows from $U(z_c) = c(k)$, where U is the air velocity and $c(k)$ is the phase velocity of a wave with wave-number k .

The quasi-laminar approach was criticized because the effect of turbulence on the wave-induced motion was neglected, and nonlinear effects such as wave-mean flow interaction were not considered.

First attempts to describe the effects of turbulence by means of a mixing length model have been criticized as well, however, mainly because the eddies in the outer layer in the air are too slow to transfer a significant amount of momentum on the time scale of the wave motion. *Belcher* and *Hunt* [7] demonstrated why mixing-length modelling is not appropriate in rapidly varying circumstances such as occur for airflow over growing wind waves. In *Belcher* and *Hunt* [7] model, the main mechanism for wave growth in the is the so-called '*non-separated sheltering*': the Reynolds stresses close to the surface cause a thickening of the boundary layer on the leeside of the waves which results in flow separation when the slope is large enough.

Rapid distortion models, such as the one of [7], allows for a determination of the range of validity of Miles' theory. Depending on the assumption regarding how rapid eddies transfer momentum, Miles' approach may be justified for typical ocean conditions [46].

For a given wind profile, quasi-laminar theory is fairly successful in predicting growth rates and wave-induced profiles. It ignores, however, a possible

change of wind profile while the ocean waves are evolving [46].

The theory of the interaction of wind and waves was elaborated by *Fabrikant* [31] and *Janssen* [48]. The so-called ‘*quasi-linear theory*’ of wind-wave generation keeps track of the slow evolution of the sea state and its effects on the wind profile. At each particular time the wave growth follows from Miles’ theory. It turns out that quasi-linear theory permits an explanation of the observed dependence of the airflow on the sea state.

Nonlinear four-wave Interactions: It is nowadays widely accepted that resonant weakly nonlinear interactions between sets of four waves play an important role in the evolution of the energy spectrum of free surface gravity waves propagating at the ocean’s surface. This role became clear as a result of the JONSWAP project [41].

The basic equation describing these interactions is the Boltzmann integral proposed by *Hasselmann* [39] and a couple of years later by *Zakharov1968* who derived it in a form known as the *kinetic equation*. *Hasselmann* [39] developed the theoretical framework for nonlinear four wave interactions for homogeneous seas with a constant depth. He formulated an integral expression for the computation of these interactions, which is known as the Boltzmann integral for surface gravity waves.

Recent work by *Janssen* [52] suggests that quasi-resonant four-wave interactions play a major role in uni-directional wave field, in relation to the development of modulational instabilities and the occurrence of freak waves. Yet unclear is the role of non-resonant interactions in two-dimensional cases.

For nonlinear interactions in deep water the basic problem seems to be the practical implementation of an already well established theory. The struggle between the sheer volume of calculations implied by the theory and the practical possibilities of the present computers has been dominating the stage for a long while. The capability of routinely carrying out full exact computations is still far away. The present efforts aim at developing new methods (MDIA, neural, diffusion), while exploiting the ever increasing computer power, reducing the necessary time within manageable limits. These calculations are always compromises, and usually this appears as undesirable characteristics of the final results.

Spectral Wave Energy Dissipation: Spectral wave energy dissipation represents the least understood part of the physics relevant to wave modelling. There is a general consensus that the major part of this dissipation is supported by the wave breaking, but physics of this breaking process, particularly for the spectral waves, is poorly understood. Furthermore, there is also a poor understanding on the wave energy dissipation by whitecapping and its role in the spectra evolution.

There is hardly any agreement neither on the basic physics of the process nor on the best way, although empirical, to model it.

To summarize, there are several studies which offer different analytical models. None of the models deals with the dynamics of wave breaking, which is responsible for dissipation. Rather, they suggest hypotheses to interpret either pre-breaking or post-breaking wave field properties. All of the hypotheses lack experimental support or validation. Results vary from the dissipation being a linear function of the wave spectrum to the dissipation being quadratic, cubic or even a function of the spectrum to the fifth power.

Concluding, there is no consensus among analytical theories of the spectral dissipation of wave energy due to wave breaking, even with respect to the basic characteristics of the dissipation function. In addition, the theoretical dissipation functions strongly disagree with the experiments which, on the other hand, exhibit some common features in the results but, often, are in serious disagreement with each other.

Wave-Bottom Interactions: Dissipation associated to the interaction of waves with the bottom is another subject where we still have a lot to learn. The problem is associated with two basic characteristics of what is going on: the number of contemporary and alternative bottom mechanisms that can be active to dissipate the wave energy, and the difficulty of analysing and measuring a process while it is active. As a matter of fact practically all the data we have concern the measurements of wave characteristics at different progressive locations, in so doing providing information only on the integrated effect of the process, rather than on the physics and its details.

In general we can say we have a fair idea of the physics involved, but we lack a solid quantification of the energy lost in the process. The integrated characteristics of the surface are not always purely indicative of the bottom dissipation processes, simply because there are often other, not necessarily

bottom, processes at work, e.g. generation by wind and white-capping. On the other hand the true characteristics of the bottom are mostly unknown (dimensions of the ripples, sheet flow, etc.) or, at best, modelled only with large approximations, and they can easily change the estimate of the derived energy loss of an order of magnitude.

As waves approach shallower water they start to ‘feel the bottom’ and the spectrum adopts a new self-similar shape in which enhanced dissipation is evident.

Several bottom-related dissipative processes are known: percolation into a porous bottom, motion of a mobile bed or dissipation through turbulent bed shear stress with an associated bottom boundary layer. Most spectral wave models that take into account bottom dissipation as a source term, only model dissipation by bottom friction.

Luo and Monbaliu [64] summarized the work done on the bottom friction term used in spectral wave models:

$$S_{bf}(\sigma, \theta) = -C_f \frac{K}{\sinh(Kh)} S(\sigma, \theta) \quad (1.1)$$

where $S(\sigma, \theta)$ is the directional-frequency wave energy spectrum, K is the wave-number and h is the water depth. The coefficient C_f depends on the closure model used to solve the momentum equations of the bed boundary layer and several formulations (see for example *Hasselmann et al.* [41], *Collins* [19] and *Madsen et al.* [67]) are given in literature.

Nonlinear Interactions in Shallow Water: Nonlinear interactions in shallow water are characterized by the relevance of the third-order ones. Dealing with interactions, not only in resonant, but also in near-resonant conditions, is today an active field of research, and the associated wave modelling activity has different lines of attack in this respect.

In general triad interactions transfer energy from the incident wave components to higher and lower frequency components (see, e.g., *Freilich and Guza* [33], *Kaihatu and Kirby* [55], *Ruessink* [89], *Sheremet et al.* [92], *Janssen et al.* [52], and many others). These interactions not only broaden the frequency spectrum in shallow water, but also phase-couple the spectral components, causing the characteristic steepening and pitching forward of near-breaking

wave crests.

Shallow water wave propagation models can generally be divided in two major categories (see also *Agnon and Sheremet*, [1]):

- **Deterministic** (phase resolving) models are usually derived from the Euler equation for potential flows (Laplace equation + boundary conditions) under the hypothesis of weak nonlinearity and in the limit of shallow water. These models, including both the physical domain Boussinesq models and the complex amplitude evolution models (spectral models), resolve the phases of the individual waves.
- **Stochastic** (phase-averaged) models are derived from deterministic equations by applying a turbulence-like closure hypothesis to the infinite set of coupled equations governing the evolution of the spectral moments. For any given deterministic wave equation, with a suitable closure hypothesis, a stochastic model can be developed. Since the closure approximation invariably introduces errors, the underlying deterministic model is in principle more accurate than its stochastic counterpart.

As waves approach the shore, additional effects such as bottom friction and depth-induced wave breaking must be considered.

1.2 The Oil-spill models state-of-the-art

Oil spill modeling and understanding of some of the processes have advanced in the last two decades. However, for some of the other important processes our understanding remains poor and their modeling methods are ad-hoc. There is still much more research needed to understand the fundamental mechanisms of these processes.

These models can vary from simple trajectory type to models that attempt to comprehensively simulate the physical-chemical-biological processes that oil undergoes after a spill. Which type of model to use depends on the situation, model availability, and end objectives.

The most important processes that influence the time evolution of oil after a spill in marine environment are *advection and diffusion/dispersion, mechanical spreading, vertical mixing, evaporation, dissolution, emulsification, oil-sediment interaction, sedimentation* and *shoreline deposition* and *re-entrainment* of oil.

This review of the state of the knowledge on each process identified is carried out following [86] and [105].

Oil transport and dispersion: the transport and dispersion of oil on the water surface and in water column can be modeled by using a modified form of the advection-diffusion equations [4]. This modified form is much more complex than its standard form, because it deals with multi species both for source and sink terms. Multi species are the different sized oil droplets that can belong to surface layer or water column. Source and sink terms are evaporation, dissolution, oil break up from the surface, and resurfacing of oil. In addition buoyant velocity of oil droplets need to be accounted for each species.

Given the complexity of dealing with this multi-species problem with sources and sinks, Lagrangian methods are much more suitable for oil spill modeling. In addition, oil generally occupies a much smaller area than the modeling domain and oil droplets can appear anywhere in the system in scattered form.

The most common method is the *Lagrangian Parcel* (LP) method [107], where oil is initially represented as a large number of parcels. Then, these LPs may move around in the modeling domain according to ambient and buoyant velocities and turbulent diffusion/dispersion. A LP consists of large

number of droplets of a certain size, but can grow or shrink in mass. Further details can be found in [107].

Vertical Mixing and Resurfacing: Oil spilled on or near the water surface can be broken up into droplets by the turbulence caused by water current, wind, and waves. While there can be a coherent oil slick on the water surface, a significant portion of the oil can be in the form of oil droplets entrained in the water column.

Oil droplet surfacing will have a major impact on how the oil is transported.

The surfacing rate depends on the oil droplet/bubble size distribution (BSD). The BSD also depends on the droplet break up and coalescence due to turbulence.

The present knowledge does not allow the calculation of BSD with any confidence. The empirical methods developed by Delvigne and co-workers (e.g. [27]) are the most commonly implemented methods to calculate the break up amount, BSD, and the intrusion depth.

Bandara and Yapa [3] developed a more robust method to calculate oil droplet sizes and their distribution in deepwater plumes.

Evaporation and Dissolution: Depending on the type of oil, evaporation can be the process that causes the major loss of oil mass. In addition, it directly influences dissolution, emulsification and adsorption of oil dissolved to sediments.

The amount of oil evaporation depends on the oil type, wind condition, temperature, and slick area.

Evaporation and dissolution can be simulated using similar equations although the mass transfer coefficients vary [93]. Wind is not a factor affecting dissolution. Amounts of oil dissolution are much smaller than that of evaporation but, for impact assessment, dissolved amount of oil is important because of its direct effect on toxicity.

Mackay et al.'s [65] multi component method although dated, gives good estimates for oil evaporation and dissolution amounts. To use this method

oil vapor pressures (VP) are needed. [87] provides an improved method to calculate oil vapor pressures (VP).

More recent developments using other approaches and empirical methods can be found in a series of papers published in AMOP (Arctic Marine Oil Spill Program), technical seminars sponsored by Environment Canada.

Emulsification: This is a process that can take days to weeks to develop and it depends on both turbulence and oil chemistry. When stable emulsions are formed, the viscosity can increase by few orders of magnitude. The density can also change due to uptake of water which can be as high as 80% and in some cases can be even slightly higher than the water density.

Evaporation and weathering impact on emulsification. Emulsification can be enhanced by evaporation and dissolution [32].

Due to all these property changes, once emulsions are formed it can significantly impact the fate and transport of oil including changing some of the oil to transport inside the water column instead of on the water surface. *Xie et. al's* [104] model takes into account both oil chemistry and ocean turbulence to simulate emulsification.

Oil and Sediment Interaction: A main process of removal of oil from the water environment is oil sediment interaction. It results in an agglomerate which sinks to the bottom of the ocean.

Despite the importance of this process it is one of the poorly understood processes.

[4] is a very good attempt to model this process. It explains different processes within oil sediment interaction such as partitioning and adsorption. Further information can be found in [4].

Shoreline Deposition and Re-entrainment of Oil: Oil upon reaching a shoreline deposits either fully or partially and can have a devastating effect on the coastline. These effects can be on recreation, fishing, or ecology. This process is important for both short and long term impact assessment.

Although oil booms are used to protect shorelines, they are not always effective. The amount of oil retained in a coastline depends on the type of beach and its holding capacities. The type of beach has been categorized using an Environmental Sensitivity Index (ESI) by [37]. The ESI can be loosely connected with a half-life value for the beach retention capacity. This method has been used in models by a few (e.g. [17], [91]). ESI Atlases are available for many coastlines and inland shorelines in the United States and Canada. There has not been extensive research for this subject. [37] and [90] are a good sources for further readings.

Chapter 2

Numerical Modeling of Surface Waves

2.1 Linear Wave Theory

Almost all physical systems have the ability to perform free oscillations around an equilibrium configuration if disturbed by a small perturbation.

Waves are the way by which an oscillation caused by a perturbation originated by a source located at a some space-time defined point is transmitted in space and time across a physical system without movement of the medium: therefore energy travels with waves , while the motion of matter is generally small or absent.

The periodic behavior of waves is generated by the existence of some kind of *restoring force* which tries to bring the system back to its *undisturbed* state every time the perturbation causes the system exceeding of the equilibrium.

The most common wave motion experienced by anyone is that one that occurs at the free surface of a liquid disturbed by a some kind of perturbation and characterized by *gravity* as the most important restoring force: *ocean waves* belong to this category.

In this section the Linear Theory and some of its physical consequences will be examined. The analysis is carried following [60] and [26].

2.1.1 High Frequency Waves in The Ocean

Applying the concept of waves to the ocean it is possible to define ocean waves as the *vertical motions of the ocean surface* caused by some kind of perturbation.

Depending on the nature of the perturbation and of the restoring force and the temporal scale typical of the wave motion, it is possible to identify different kind of ocean waves:

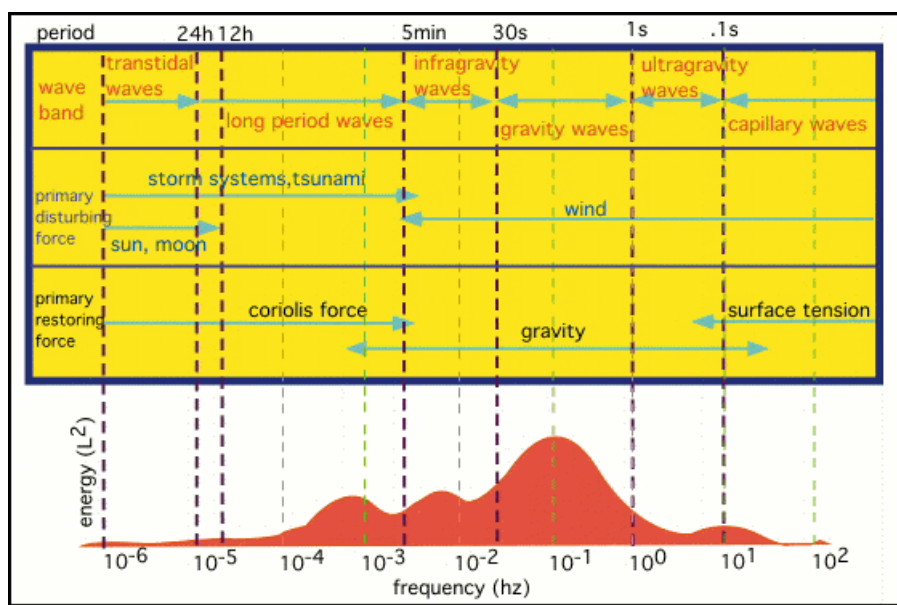


Fig. 2.1: Typical ocean wave spectrum (from [9])

Naturally all these phenomena are at time scales shorter than the day. For day-long or longer scales ocean currents are turbulence induced currents, not to be discussed further in this Thesis.

Considering the *nature of the perturbation*, it is possible to identify **Wind Waves**, which are forced by the local wind blowing on the air/water interface, **Tsunamis**, which are waves generated by a submarine ‘land’ slide or earthquake, **Tides**, sea surface oscillations due to fluctuating gravitational forces of the Moon and Sun, **Storm Surges**, the large-scale elevation of the ocean surface generated by the low atmospheric pressure and the high wind speeds associated to a severe storm.

On the other hand, thinking about the *nature of the restoring force* we define **Gravity Waves** and **Capillary Waves**, for which the restoring force is, respectively, the Gravity force and the Surface Tension.

Finally, the different temporal scales **Long Waves**, which include waves with a period between more than 24 hours and about 5 minutes, and **Short Waves**, which are sea surface oscillations with a period between about 5 minutes and 0.01 seconds.

2.1.2 The Wave Equation and Wave Parameters

Defining η as any type of disturbance, like the displacement of the free surface in a liquid, it is possible to show that the simplest equation which describes the evolving in time and space of such a perturbation is the *Wave Equation*

$$\frac{\partial^2 \eta}{\partial t^2} = c^2 \nabla^2 \eta \quad (2.1)$$

which is a linear second order partial differential equation of the hyperbolic type. Considering waves traveling only in the x -direction the Wave Equation 2.1 becomes

$$\frac{\partial^2 \eta}{\partial t^2} = c^2 \frac{\partial^2 \eta}{\partial x^2} \quad (2.2)$$

which has as general solution the so called *d'Alembert solution*

$$\eta = f(x - ct) + g(x + ct) \quad (2.3)$$

where f and g are any arbitrary functions and $f(x - ct)$ represents a wave propagating in the positive x -direction (see fig. 2.2) while $g(x + ct)$ propagates in the negative x -direction at speed c .

The simplest disturbance which can be thought is the sinusoidal wave with equation

$$\eta = a \sin \left[\frac{2\pi}{\lambda} (x - ct) \right] \quad (2.4)$$

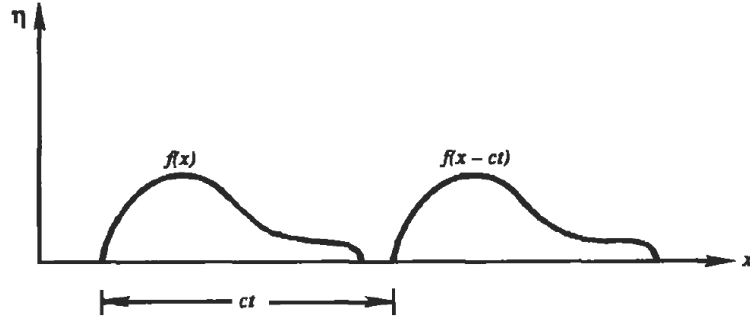


Fig. 2.2: Profile of progressive wave $f(x - ct)$ at two times (from [60])

where a is the *amplitude* of the wave, λ is the *wavelength* and c is the speed of propagation of the wave shape $\sin\left[\frac{2\pi}{\lambda}(x - ct)\right]$. Because of the argument $\sin\left[\frac{2\pi}{\lambda}(x - ct)\right]$ is called *phase*, c is commonly called *phase velocity*. It descends that points with equal phase present the same wave shape, for example crests or trough.

The *period* T of the wave is defined as the time needed by the wave to travel a space equal to λ with the *phase velocity* c :

$$T = \frac{\lambda}{c} \quad (2.5)$$

and the number of oscillations at a point per unit time is the *frequency* given by

$$f = \frac{1}{T} \quad (2.6)$$

Commonly, the equation 2.4 is written in function of the *wave number* k and the *angular frequency* ω instead of the *wavelength* λ and the *frequency* f , respectively. The *wave number* is defined as the number of complete waves in a length 2π

$$k \equiv \frac{2\pi}{\lambda} \quad (2.7)$$

while the *angular frequency*, also called *radian frequency*, is the rate of change of phase (in radians) per unit time.

$$\omega \equiv \frac{2\pi}{T} = 2\pi f = kc \quad (2.8)$$

and equation 2.4 can be written as

$$\eta = a \sin(kx - \omega t) \quad (2.9)$$

For horizontal plane sinusoidal waves equation can be generalized as

$$\eta = a \sin(\vec{K} \cdot \vec{x} - \omega t) = a \sin(kx + ly - \omega t) \quad (2.10)$$

where $\vec{K} = (k, l)$ is the *wave number vector* with magnitude

$$K^2 = k^2 + l^2 \quad (2.11)$$

and $\vec{x} = (x, y)$ is the *vector position*.

The *wavelength* of equation 2.10 is $\vec{\lambda} = (\lambda_x, \lambda_y)$, where $\lambda_x = 2\pi/k$ and $\lambda_y = 2\pi/l$ and the magnitude of $\vec{\lambda}$ is $\lambda = 2\pi/K$.

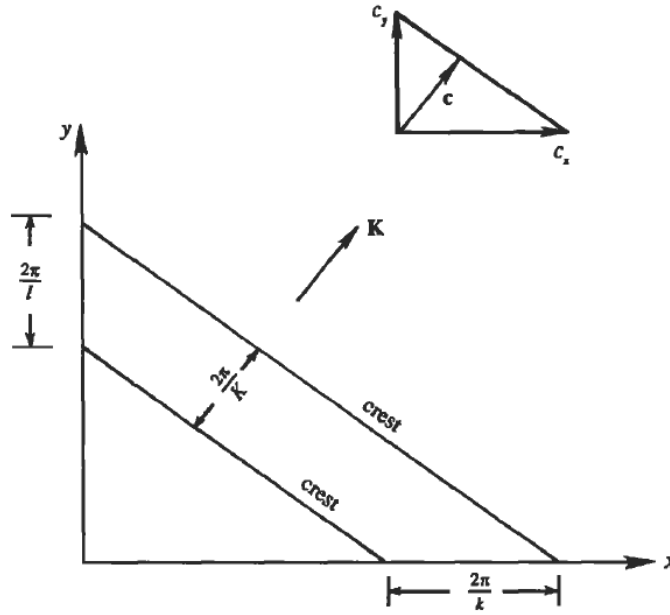


Fig. 2.3: Wave propagating in the xy -plane. In the right north corner it is shown how the components c_x and c_y are added to give the resultant \vec{c} (from [60])

The *phase velocity vector* has the direction of propagation parallel to that of \vec{K} one and can be written as

$$\vec{c} = \frac{\omega}{K} \frac{\vec{K}}{K} \quad (2.12)$$

The modulo of \vec{c} is $c = \omega/K$ and it is clear that the component of the phase velocity do not obey the rule of vector addition (in fig 2.3 the method to

calculate \vec{c} starting from components is shown).

If in the ocean is present a uniform mean flow \vec{U} , then the observed *phase velocity* is

$$\vec{c}_o = \vec{c} + \vec{U} \quad (2.13)$$

The dot product of the previous equation 2.13 with \vec{K} and the using of equation 2.12 allow to write

$$\omega = \sigma + \vec{U} \cdot \vec{K} \quad (2.14)$$

where ω is the *observed radian frequency* at a fixed point, also called *absolute frequency*, while σ is the *intrinsic radian frequency* measured by an observer moving with the mean flow and also called *relative frequency*. In other words, in the presence of a mean flow, the wave frequency is *Doppler shifted* by an amount of $\vec{U} \cdot \vec{K}$.

2.1.3 Surface Gravity Waves

In this sub section the equation describing gravity waves at the free surface of a sea of uniform depth H will be resulted.

To linearize the problem, let assume that the amplitude a of the free surface oscillation is small if it is compared with with the *wavelength* λ and the depth H ; then it means that

$$\frac{a}{\lambda} \ll 1 \quad (2.15)$$

$$\frac{a}{H} \ll 1 \quad (2.16)$$

where condition 2.15 means that the *slope* of the sea surface is small and condition 2.16 implies that the depth can be considered as constant in time.

In addition, let consider a wave with a frequency f large respect to the *Coriolis frequency*, so that the fluid is unaffected by the Earth rotation and can be considered *not in rotation*.

In the last, let think about a fluid with uniform density and small viscosity, so that it is relevant only at the boundaries and do not affect the wave propagation significantly. The last three conditions, according to *Kelvin's*

Circulation Theorem (see Appendix B), allow to consider the resulting motion of the fluid as *irrotational* and ensure the existence (see Appendix A) of the function *potential velocity* ϕ defined as

$$u = \frac{\partial \phi}{\partial x} \quad v = \frac{\partial \phi}{\partial y} \quad w = \frac{\partial \phi}{\partial z} \quad (2.17)$$

Now, for algebraic simplicity, let consider a case where the wave propagate only in the x -direction and the motion is only bi-dimensional in the $x - z$ plane.

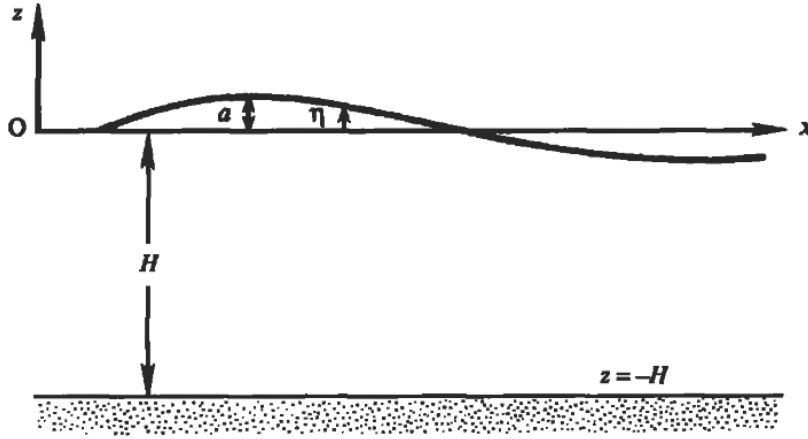


Fig. 2.4: Rapresentation of the Gravity Surface Wave physical problem [60]

Then, the substitution of identity 2.17 in the *continuity equation* $\vec{\nabla} \cdot \vec{u} = 0$ yields the *Laplace equation*

$$\frac{\partial^2 \phi}{\partial x^2} + \frac{\partial^2 \phi}{\partial z^2} = 0 \quad (2.18)$$

which is a well-known second order homogeneous linear partial derivative equation. In order to resolve this equation, it is needed to specify boundary conditions at the bottom and at the free surface.

At the *bottom*, the *kinematic boundary condition* is that the velocity field component normal to the bottom has to be zero, which means that

$$w|_{z=-H} = \frac{\partial \phi}{\partial z} \Big|_{z=-H} = 0 \quad (2.19)$$

The *kinematic boundary condition* at the surface is that the fluid particle never leaves it, that is

$$w|_{z=\eta} = \frac{D\eta}{Dt} \quad (2.20)$$

and, remembering that the *Total derivative* is defined as

$$\frac{D\bullet}{Dt} = \frac{\partial\bullet}{\partial t} + \vec{u} \cdot \vec{\nabla}\bullet \quad (2.21)$$

we can write, for our bi-dimensional problem,

$$\frac{\partial\eta}{\partial t} + u \frac{\partial\eta}{\partial x} \Big|_{z=\eta} = \frac{\partial\phi}{\partial z} \Big|_{z=\eta} \quad (2.22)$$

which can be simplified to

$$\frac{\partial\eta}{\partial t} = \frac{\partial\phi}{\partial z} \Big|_{z=0} \quad (2.23)$$

justifying it with the fact that, for small amplitude wave, both u and $\partial\eta/\partial x$ are small and, therefore, also the quadratic term $u(\partial\eta/\partial x)$ is an order smaller than the other terms and that, at the first order of accuracy, expanding $\partial\phi/\partial z$ in a Taylor series around $z = 0$, we can write that

$$\frac{\partial\phi}{\partial z} \Big|_{z=\eta} = \frac{\partial\phi}{\partial z} \Big|_{z=0} \quad (2.24)$$

On the surface, to ensure the coupling with the atmosphere, we have to declare a *dynamic boundary condition* too, which is

$$p \Big|_{z=\eta} = 0 \quad (2.25)$$

which can be simplified, as before, in

$$p \Big|_{z=0} = 0 \quad (2.26)$$

Substituting this in the *Bernoulli' equation* for a bi-dimensional motion

$$\frac{\partial\phi}{\partial t} + \frac{1}{2}(u^2 + w^2) + \frac{p}{\rho} + gz = 0 \quad (2.27)$$

we obtain, neglecting the non linear term $(u^2 + w^2)$,

$$\frac{\partial\phi}{\partial t} + g\eta = 0 \quad (2.28)$$

Hence, summarizing, the gravity surface wave physical problem is described by the *Laplace equation*

$$\frac{\partial^2 \phi}{\partial x^2} + \frac{\partial^2 \phi}{\partial z^2} = 0 \quad (2.29)$$

and the three boundary conditions

$$\frac{\partial \phi}{\partial z} = 0, \quad \text{at } z = -H \quad (2.30)$$

$$\frac{\partial \eta}{\partial t} = \frac{\partial \phi}{\partial z}, \quad \text{at } z = 0 \quad (2.31)$$

$$\frac{\partial \phi}{\partial t} = -g\eta, \quad \text{at } z = 0 \quad (2.32)$$

To solve the partial differential problem, let assume the simplest general solution for η of the form

$$\eta = a \cos(kx - \omega t) \quad (2.33)$$

For a cosine dependence of η on $(kx - \omega t)$, the two surface conditions 2.31 and 2.32 imply that ϕ must be a sine function of $(kx - \omega t)$. Assuming therefore a solution for ϕ in the form of *separated variable*, it is possible to write

$$\phi = f(z) \sin(kx - \omega t) \quad (2.34)$$

and the *Laplace equation* 2.29 become

$$\frac{\partial^2 f}{\partial z^2} - k^2 f = 0 \quad (2.35)$$

As a second order homogeneous linear partial differential equation, the general solution for 2.35 is

$$f(z) = Ae^{kz} + Be^{-kz} \quad (2.36)$$

and consequently the *potential velocity* is given by

$$\phi = (Ae^{kz} + Be^{-kz}) \sin(kx - \omega t) \quad (2.37)$$

Coefficients A and B have to be determined applying boundary conditions to equation 2.37. Applying conditions 2.30 and 2.31 to equation 2.37 and using the general solution for η 2.33 we obtain the linear system for A and B

$$\begin{cases} B = Ae^{-2kH} \\ k(A - B) = a\omega \end{cases} \quad (2.38)$$

which has solution

$$A = \frac{a\omega}{k(1 - e^{-2kH})} \quad B = \frac{a\omega e^{-2kH}}{k(1 - e^{-2kH})} \quad (2.39)$$

Using solutions for A and B in 2.37 we obtain that the *potential velocity* is given by

$$\phi = \frac{a\omega \cosh k(z + H)}{k \sinh kH} \sin(kx - \omega t) \quad (2.40)$$

and consequently the velocity components are

$$u = a\omega \frac{\cosh k(z + H)}{\sinh kH} \cos(kx - \omega t) \quad (2.41)$$

$$v = a\omega \frac{\cosh k(z + H)}{\sinh kH} \sin(kx - \omega t) \quad (2.42)$$

Finally, substituting 2.40 and 2.33 into dynamical surface condition 2.32 we have the *dispersion relation*

$$\omega^2 = gk \tanh kH \quad (2.43)$$

from which results the *phase speed*

$$c = \sqrt{\frac{g}{k} \tanh kH} \quad (2.44)$$

Waves for which c is a function of k are called *dispersive*, because wave with different length propagates with different speed, and therefore gravity surface waves for which the relation 2.43 applies are *dispersive*.

Considering that for *deep waters* result that

$$\frac{H}{\lambda} \gg 1 \quad (2.45)$$

and that for *shallow waters* applies

$$\frac{H}{\lambda} \ll 1 \quad (2.46)$$

remembering that $\tanh(x) \rightarrow 1$ for $x \rightarrow \infty$ and that $\tanh(x) \approx x$ for $x \rightarrow 0$, it is possible to write the following approximated *dispersion relation*:

$$\omega = \sqrt{gk}, \quad \text{for} \quad \text{deepwater} \quad (2.47)$$

$$\omega = k\sqrt{gH}, \quad \text{for} \quad \text{shallowwater} \quad (2.48)$$

Under these approximations, the *phase speed* becomes

$$c = \sqrt{\frac{g}{k}}, \quad \text{for} \quad \text{deepwater} \quad (2.49)$$

$$c = \sqrt{gH}, \quad \text{for} \quad \text{shallowwater} \quad (2.50)$$

Hence, in *deep waters* waves are dispersive while in *shallow waters* we find non dispersive waves.

2.1.4 Wave Energy

Surface gravity waves possess *Kinetic Energy* due to the motion of the fluid and *Potential Energy* due to the deformation of the free surface.

Consider a case where the waves propagate in the x direction only, and that the motion is two dimensional in the xz - *plane* (see figure 2.4). Let the vertical coordinate z be measured upward from the undisturbed free surface. The free surface displacement is $\eta = a \cos(kx - \sigma t)$.

As the Potential Energy of an element in the fluid (per unit length in y) is

$$dE_p = \rho g z dz dx \quad (2.51)$$

the *Potential Energy* per unit horizontal area of the wave system is

$$E_p = \frac{\rho g}{\lambda} \int_0^\lambda \int_{-H}^\eta z dz dx - \frac{\rho g}{\lambda} \int_0^\lambda \int_{-H}^0 z dz dx \quad (2.52)$$

$$= \frac{\rho g}{\lambda} \int_0^\lambda \int_0^\eta z dz dx = \frac{\rho g}{2\lambda} \int_0^\lambda \eta^2 dx = \frac{1}{2} \rho g \bar{\eta}^2 \quad (2.53)$$

while the average *Kinetic Energy* per unit horizontal area can be obtained integrating over the depth and averaging over a wave length the Kinetic energy associated with a small parcel of fluid with mass $dm = \rho dx dz$:

$$E_k = \frac{\rho}{2\lambda} \int_0^\lambda \int_{-H}^0 (u^2 + w^2) dz dx = \frac{1}{2} \rho g \bar{\eta}^2 \quad (2.54)$$

The total wave energy in the water column per unit horizontal area is :

$$E = E_p + E_k = \rho g \bar{\eta}^2 = \frac{1}{2} \rho g a^2 \quad (2.55)$$

considering that the average of $\cos^2 x$ over a wave length is $1/2$.

The *Energy* for unit surface area associated to a single sinusoidal wave is therefore

$$E = \frac{1}{2} \rho g a^2 \quad (2.56)$$

where ρ denotes *sea water density* at the surface.

It can be shown that in a *dispersive* system the energy of a wave component propagates at a *group velocity* c_g defined

$$c_g = \frac{\partial \omega}{\partial k} \quad (2.57)$$

instead of at the *phase speed* c .

Therefore, for surface gravity wave with dispersion relation 2.43 the group velocity is found to be

$$c_g = \frac{c}{2} \left[1 + \frac{2kH}{\sinh 2kH} \right] \quad (2.58)$$

and, using the *deep water* and *shallow water* approximations, the two limiting cases are

$$c_g = \frac{1}{2}c = \frac{1}{2}\sqrt{\frac{g}{k}} \quad \text{deep water} \quad (2.59)$$

$$c_g = c = \sqrt{gH} \quad \text{shallow water} \quad (2.60)$$

2.1.5 Fluid Particle Path

A water particle at rest will be displaced from its position by the wave-induced pressures. In order to examine particle orbits, we need to use a Lagrangian formalism to describe the motion of the particle.

Let (x_0, y_0) be the coordinates of a fluid particle at rest. Then, the coordinates of the particle during its wave-induced motion will be, as shown in figure 2.5, $(x_0 + \xi, y_0 + \zeta)$ which, in a Lagrangian formalism, can be written as $(\xi(x_0, z_0, t), \zeta(x_0, z_0, t))$.

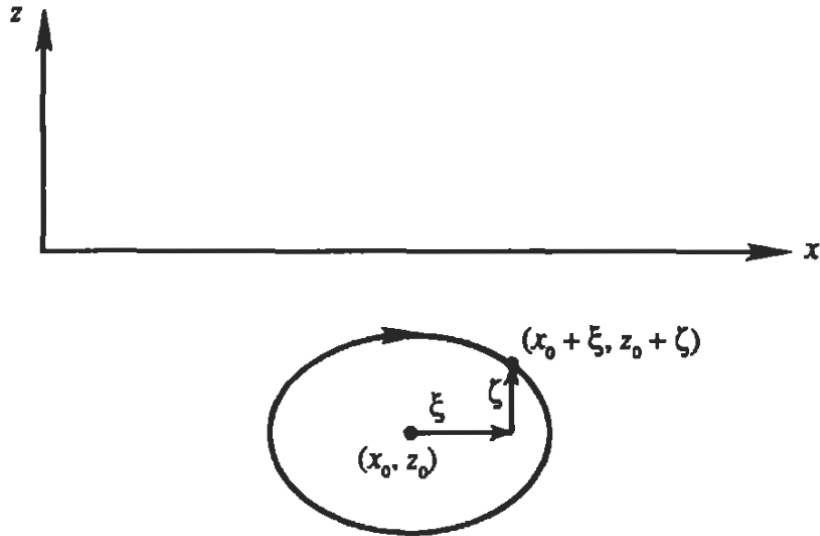


Fig. 2.5: Orbit of a fluid particle whose mean position is (x_0, z_0) [60]

The velocity components of the particle motion will be

$$u = \frac{\partial \xi}{\partial t} \quad (2.61)$$

$$v = \frac{\partial \zeta}{\partial t} \quad (2.62)$$

where the partial derivative symbol is used because in Lagrangian formalism the particle identity (x_0, z_0) is kept fixed in the time derivative.

Expanding the velocity components along the particle path with a Taylor expansion around the velocity of the particle at its rest position, for small amplitude waves we find that, at the first order of approximations, the velocity of the particle in the position $(\xi(x_0, z_0, t), \zeta(x_0, z_0, t))$ is equal to the velocity of the particle at its rest position $(\xi(x_0, z_0, t_0), \zeta(x_0, z_0, t_0)) = (x_0, y_0)$.

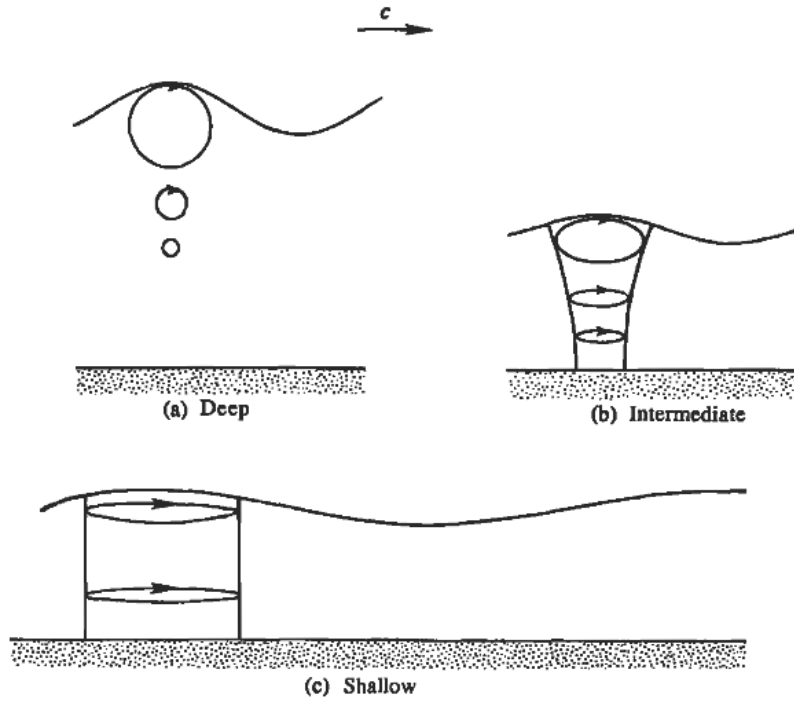


Fig. 2.6: Particle orbits of wave motion in deep, intermediate and shallow waters

Therefore, using equations 2.41 and 2.42, it is possible to write

$$\frac{\partial \xi}{\partial t} = a\omega \frac{\cosh k(z_0 + H)}{\sinh kH} \cos(kx - \omega t) \quad (2.63)$$

$$\frac{\partial \zeta}{\partial t} = a\omega \frac{\sinh k(z_0 + H)}{\sinh kH} \sin(kx - \omega t) \quad (2.64)$$

The time integration of 2.63 2.64 results in

$$\xi = -a \frac{\cosh k(z_0 + H)}{\sinh kH} \sin(kx - \omega t) \quad (2.65)$$

$$\zeta = a \frac{\sinh k(z_0 + H)}{\sinh kH} \cos(kx - \omega t) \quad (2.66)$$

By squaring 2.65 and 2.66, adding the two equations and using trigonometric identity we obtain

$$\xi^2 / \left[a \frac{\cosh k(z_0 + H)}{\sinh kH} \right]^2 + \zeta^2 / \left[a \frac{\sinh k(z_0 + H)}{\sinh kH} \right]^2 = 1 \quad (2.67)$$

which is the equation of an ellipse with both the semimajor and the semiminor axis that decrease with depth and with the semiminor axis which vanishes at $z = -H$ (see figure 2.6).

2.1.6 Stokes' Drift

Observing the motion of a floating object placed on the sea surface, it is clear that it is 'transported' by waves in the direction of their propagation.

This phenomenon is called *Stokes' Drift*, in honor of George G. Stokes who was the first to identify and describe in 1847 this non-linear process [97], and is due to the fact that the trajectory which describes the displacement of a near-surface fluid particle forced by wave motion is not closed but has the shape shown in fig 2.7 : essentially the particle moves forward faster (when it is at the top of its trajectory) than backward (when it is at the bottom of its path) and this fact generates the drift.

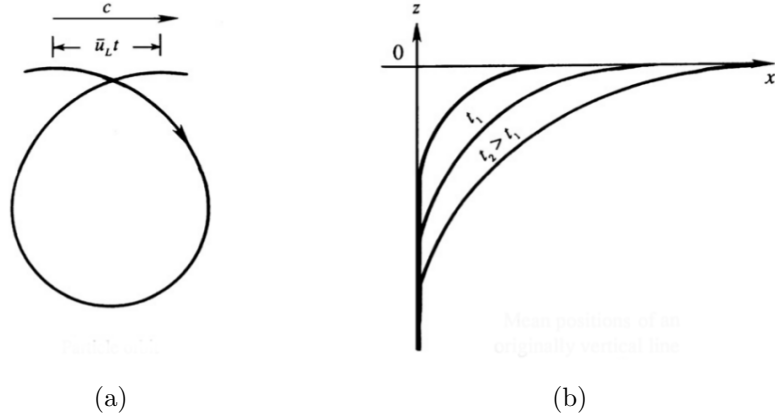


Fig. 2.7: Stoke's drift: **(a)**The not closed orbit which describes the path of a near-surface water particle displaced by wave motion; **(b)**The mean position of an initially vertical line of fluid particles extending downward from the liquid surface will increasingly bend in the direction of wave propagation with increasing time. (Modified from [60])

The Stokes' Drift is a second-order effect and, to find a mathematical formulation for it, we need to describe the motion of a water particle moved by waves both with a Lagrangian formalism that with an Eulerian one.

Let consider a water particle whose position at time $t_0 = 0$ is defined by the vector position $\vec{x}_0 = (x_0, y_0, z_0)$ and the position at any subsequent time is described by the vector $\vec{x} = (x, y, z)$. Therefore, in a Lagrangian formalism, we can write

$$\vec{x}(\vec{x}_0, t_0) = \vec{x}_0 \quad (2.68)$$

At any subsequent time t , Lagrangian velocity of the particle is given by

$$\frac{\partial \vec{x}}{\partial t} = \vec{u}_L(\vec{x}_0, t) \quad (2.69)$$

where the partial derivative operator means that the initial position (used as a particle tag in Lagrangian motion description) is kept fixed in the time derivative. The particle position at any time t can be found integrating 2.69:

$$\vec{x} = \vec{x}_0 + \int_{t_0}^t \vec{u}_L(\vec{x}_0, t) dt \quad (2.70)$$

Furthermore, indicating with u the Eulerian velocity of the same particle when it is collocated at the position \vec{x} at instant time t , if the relation 2.70 is true then we can write

$$\vec{u}_L(\vec{x}_0, t) = \vec{u}(\vec{x}, t) \quad (2.71)$$

Expanding the Eulerian velocity \vec{u} in a Taylor series about \vec{x}_0 it is possible to write

$$\vec{u}_L(\vec{x}_0, t) \approx \vec{u}(\vec{x}_0, t) + (\vec{x} - \vec{x}_0) \cdot \nabla_0 \vec{u}(\vec{x}_0, t) + \dots \quad (2.72)$$

where $\nabla_0 = (\partial/\partial x_0, \partial/\partial y_0, \partial/\partial z_0)$.

Approximating eq. 2.72 to the first order, it results that the Lagrangian velocity is equal to the Eulerian one and the trajectory of the particle is circular or ellipsoid (see 2.1.5).

Understanding on the other hand that the Stokes' drift is due to the fact that the particle velocity \vec{u}_L changes in magnitude and direction during its displacement trajectory, it is useful to approximate eq. 2.72 to the second order and consider the time mean value of it (the averaging operation is usually done over one wave period T):

$$\overline{\vec{u}_L(\vec{x}_0, t)} \approx \overline{\vec{u}(\vec{x}_0, t)} + \overline{(\vec{x} - \vec{x}_0) \cdot \nabla_0 \vec{u}(\vec{x}_0, t)} \quad (2.73)$$

where $\overline{\bullet}$ stands for the time averaging operation defined as

$$\overline{\bullet} = \frac{1}{T} \int_{t-T/2}^{t+T/2} \bullet dt \quad (2.74)$$

Equation 2.73 states that the mean particle velocity is equal to its initial velocity plus a correction (proportional to the distance traveled and to the spatial rate of change of the local velocity field) due to the fact that the particle moves in an environment where the velocity field varies.

Defining therefore the Stokes' drift velocity as

$$\vec{u}_S(\vec{x}_0, t) = \overline{\vec{u}_L(\vec{x}_0, t)} - \overline{\vec{u}(\vec{x}_0, t)} \quad (2.75)$$

it is possible to write

$$\vec{u}_S(\vec{x}_0, t) = \overline{(\vec{x} - \vec{x}_0) \cdot \nabla_0 \vec{u}(\vec{x}_0, t)} \quad (2.76)$$

To estimate the Stokes' drift for gravity waves, let consider a bi-dimensional $x - z$ space and the dispersion relationship in deep water approximation ($\omega = \sqrt{gk}$) for algebraic simplicity. The velocity components and particle displacements for this motion are given in 2.41, 2.42, 2.65 and 2.66 as

$$u(x_0, z_0, t) = a\omega e^{kz_0} \cos(kx_0 - \omega t) \quad (2.77)$$

$$x - x_0 = -ae^{kz_0} \sin(kx_0 - \omega t) \quad (2.78)$$

$$w(x_0, z_0, t) = a\omega e^{kz_0} \sin(kx_0 - \omega t) \quad (2.79)$$

$$z - z_0 = ae^{kz_0} \cos(kx_0 - \omega t) \quad (2.80)$$

Substituting 2.77, 2.78, 2.79 and 2.80 into 2.76 we obtain:

$$\begin{aligned} u_S &= \frac{a^2 k \omega e^{2kz_0}}{T} \int_{t-T/2}^{t+T/2} [\sin^2(kx_0 - \omega t) + \cos^2(kx_0 - \omega t)] dt \\ &= \frac{a^2 k \omega e^{2kz_0}}{T} \int_{t-T/2}^{t+T/2} dt \\ &= a^2 k \omega e^{2kz_0} \\ w_S &= \frac{a^2 k \omega e^{2kz_0}}{T} \int_{t-T/2}^{t+T/2} [\sin(kx_0 - \omega t) \cos(kx_0 - \omega t) - \sin(kx_0 - \omega t) \cos(kx_0 - \omega t)] dt \\ &= 0 \end{aligned}$$

The Stokes' drift velocity has therefore only the x component (in a 2-dimension space, while for a 3-dimension space it can be shown similarly that it has only the $x - y$ components) and, in deep water, its surface value ($z_0 = 0$) is $a^2 k \omega$ and the vertical decay rate is twice that for the Eulerian velocity components. It implies therefore that Stokes' drift is confined very close to the sea surface.

For arbitrary water depth, the dispersion relationship is $\omega^2 = gk \tanh kh$ and it can be shown that the Stokes' drift velocity is (using prosthaphaeresis formulas for the last identity)

$$u_S = a^2 \omega k \frac{\cosh 2k(h+z)}{2 \sinh^2 kh} = ga^2 k^2 \frac{\cosh 2k(h+z)}{\omega \sinh 2kh} \quad (2.81)$$

2.2 Statistical Wave Theory

Waves in the oceans are generated by winds, and their properties, as steepness, period or direction, depend on the wind speed, the fetch (i.e, the distance over which winds blow) and the wind duration [34].

Moreover, observing the sea surface in the presence of wind-generated waves, it can be noted that the sea surface seems an irregular collection of crests and troughs, often with neither a well-defined wavelength or wave direction, nor a fixed wave height; the crests are short, and aligned in different directions, the waves move, but not all in the same direction, and do not retain their shape: the position and height of an individual crest is not predictable for more than a few wavelengths [21] .



Fig. 2.8: Sea surface moved by wind generated waves. (by Diego Bruciaferri, MEDESS4MES Oceanographic cruise, Garcia del Cid Oceanographic Research Ship, 9 September, 2013)

In order to describe, and consequently modeling, the so called *wave conditions* of the sea (e.g, the properties at some time and place of the sea surface wind generated waves), because of a deterministic method is impossible to use due to the intrinsic random nature of wind and waves, a statistical approach is usually applied to estimate some parameters, as *significant wave height* and *mean period*, which can typify a wave condition respect to another [43].

However, any small number of statistical parameters would not, in general,

completely characterise the wave conditions [43].

Considering wind waves as a stochastic process, the *spectral technique* can be used and a complete statistical description of sea wave conditions can be carried out.

In this section, both classical *statistical parameters* used to describe wind waves and *the random phase-amplitude model* based on wave spectra are described.

2.2.1 Representative Wave Parameters

To define some objective statistical parameters which can typify a given sea wave condition, before it is needed to specify objectively what a *sea wave* is.

Let consider a *wave time record* from a wave gauge at a fixed space point in the ocean: the *surface elevation* is the elevation of the sea surface at any one moment time relative to some reference level while a *wave* is usually defined as the profile of the sea surface elevation between two successive *downward* zero-crossing of the elevation [43] (see figure 2.9). Therefore surface elevation can be negative while a wave cannot be and the last comprehends always a trough and a crest.

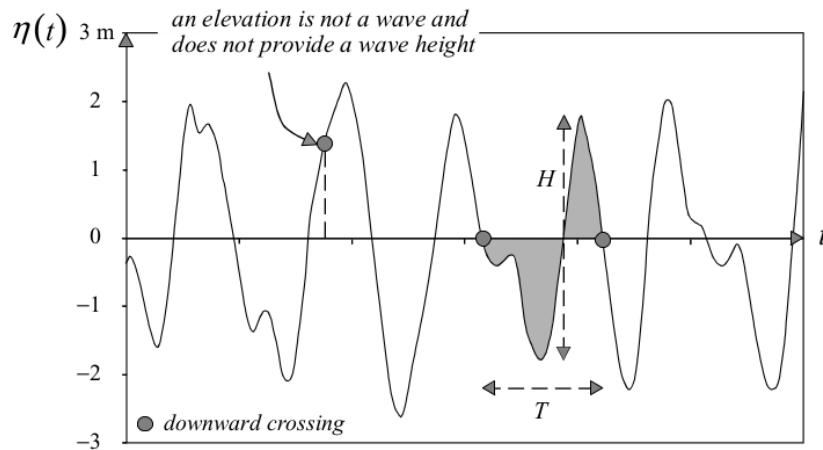


Fig. 2.9: Definition of sea wave in a time record with the downward zero-crossings method [43])

Given this practical definition of a *sea wave*, it is natural to define the *wave height* H of a wave as the vertical distance between the highest and lowest

surface elevation in a wave and the *wave period* T of the same wave as the time interval between one zero-down crossing and the next (i.e., between the start and the end of the wave)[43] [34] (see figure 2.9).

Based on such a definition, considering a long wave time record and the associated list of height and period data coming out from it, the following four kinds of *representative wave* of the wave condition during that time can be defined [34] :

- *Highest Wave, H_{max}, T_{max}* : it is the wave having as wave height H_{max} and period T_{max} the max height value and period value of the time record;
- *Mean wave, \bar{H}, \bar{T}* : In a wave record with N waves, the mean wave height \bar{H} and the mean wave period \bar{T} is defined as the arithmetic means of the heights and periods of all the wave in the record:

$$\bar{H} = \frac{1}{N} \sum_{i=1}^N H_i, \quad \bar{T} = \frac{1}{N} \sum_{i=1}^N T_i \quad (2.82)$$

where i is the sequence number in the record. An imaginary wave having height and period of \bar{H} and \bar{T} is defined as the mean wave.

- *Highest one-tenth wave, $H_{1/10}, T_{1/10}$* : The waves in the record are counted and selected in descending order of wave height from the highest wave, until one-tenth of the total number of waves is reached. The means of their heights and periods are calculated and denoted as $H_{1/10}$ and $T_{1/10}$, respectively:

$$H_{1/10} = \frac{1}{N/10} \sum_{j=1}^{N/10} H_j, \quad T_{1/10} = \frac{1}{N/10} \sum_{j=1}^{N/10} T_j \quad (2.83)$$

where j is not the sequence number in the record but the rank number of the wave based on wave height.

An imaginary wave having height and period of $H_{1/10}$ and $T_{1/10}$ is defined as the highest train one-tenth wave.

- *Significant wave (Highest one-third wave)*: The waves in the record are counted and selected in descending order of wave height from the highest wave, until one-third of the total number of waves is reached. The means of their heights and periods are calculated and denoted as

$H_{1/3}$ and $T_{1/3}$, respectively:

$$H_{1/3} = \frac{1}{N/3} \sum_{j=1}^{N/3} H_j, \quad T_{1/3} = \frac{1}{N/3} \sum_{j=1}^{N/3} T_j \quad (2.84)$$

An imaginary wave having height and period of $H_{1/3}$ and $T_{1/3}$ is defined as the highest train one-third wave.

Experiments have shown that the height value of this wave is close to the value of the *visually estimated* wave [43].

Distribution of Individual Wave Heights and Periods

In 1952 Longuet-Higgins demonstrated the applicability of the Rayleigh distribution (originally derived by Lord Rayleigh in the 19th century to describe the distribution of the intensity of sounds emitted from an infinite number of sources) to sea wave heights if waves are irregular and have very small fluctuations in the individual wave periods and whose heights exhibit a beat-like fluctuation [34].

The probability density function for the so-called *Rayleigh distribution* of individual wave heights is

$$p(x) = \frac{\pi}{2} x \exp \left[-\frac{\pi}{4} x^2 \right] \quad (2.85)$$

where x is the normalized wave height H/\bar{H} .

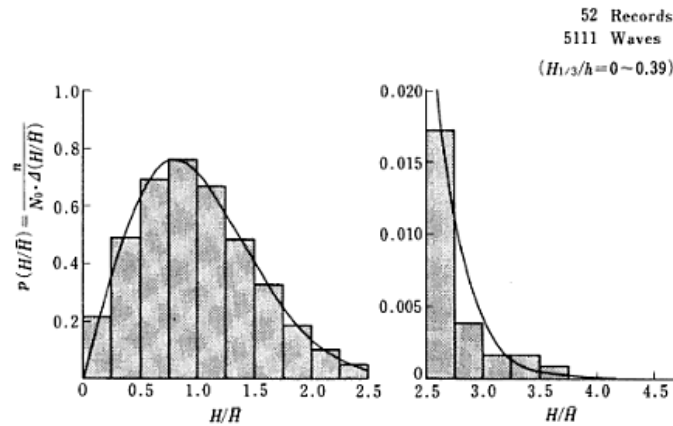


Fig. 2.10: Normalized histogram of wave heights (from [34])

An example of a distribution of wave heights obtained by assembling 52 wave records each containing about 100 waves is shown in figure 2.10 .

Here wave heights are normalized by the mean heights of the respective records and histogram is carried out by counting the relative frequencies of the normalized wave heights in their respective classes. The theoretical *Rayleigh distribution* is drawn with the solid line [34] .

The wave period does not show a universal distribution law such as the Rayleigh distribution for the wave heights. Periods of individual waves usually exhibit a distribution narrower than that of wave heights, even if it becomes broader or even bi-modal when wind and swell coexist [34] .

Relation between Representative Wave Heights and Periods

If the Rayleigh distribution is assumed to be a good approximation of the distribution of individual wave heights, it can be shown that, manipulating such probability density function, a relation between representative wave heights parameters can be found [34] . Thus, we have

$$H_{1/10} = 1.27H_{1/3} = 2.03\bar{H}, \quad H_{1/3} = 1.60\bar{H} \quad (2.86)$$

and

$$H_{max} = (1.6 \sim 2.0)H_{1/3} \quad (2.87)$$

Concerning the periods, it has been empirically found that the representative period parameters are interrelated with the following results [34] :

$$\begin{cases} T_{max} = (0.6 \sim 1.3)T_{1/3} \\ T_{1/10} = (0.9 \sim 1.1)T_{1/3} \\ T_{1/3} = (0.9 \sim 1.4)\bar{T} \end{cases} \quad (2.88)$$

For the most part of the wave records the following average value can be applied [34] :

$$T_{max} \approx T_{1/10} \approx T_{1/3} \approx 1.2\bar{T} \quad (2.89)$$

2.2.2 Wind Waves as a Stochastic Process

Viewing the sea surface elevation in presence of waves as a Stochastic Process (see appendix C for the definition of a Stochastic Process) means to consider the surface elevation at any one time and space location as a random variable [34] .

Let consider a laboratory tank where waves can be generated by an artificial wind and a fixed water gauge placed at *location A* in the tank (see figure 2.11): carrying out several experiments, let say N experiments, the value of the water surface level η measured by the water gauge at time t_1 , referred to the t_0 time which is the start time of wind blowing, will be generally different for every experiment , that is

$$\eta(i, t_1) \neq \eta(j, t_1), \quad 0 < i, j \leq N \quad (2.90)$$

where i, j indicates the experiment number [43] .

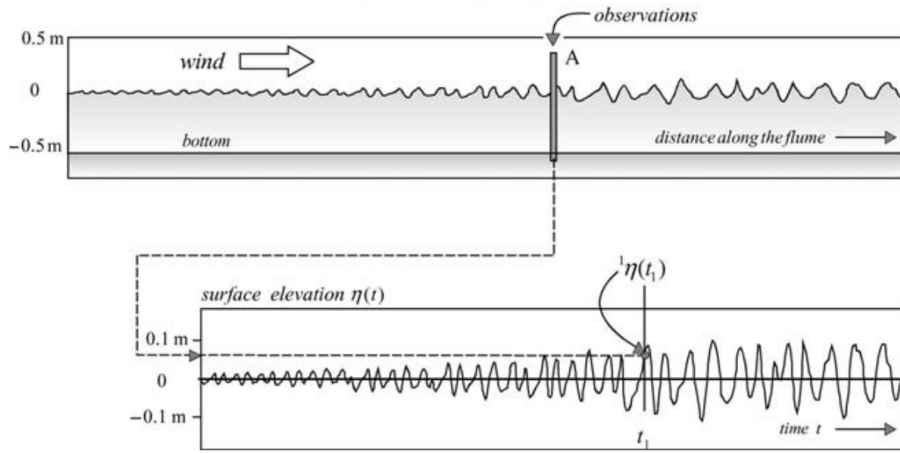


Fig. 2.11: Laboratory tank where artificial wind generates water waves and a fixed water gauge placed at *location A* in the tank where the surface η is measured at time t_1 during the experiment 1 (the subscript 1 indicates the number experiment)(modified from [43])

It follows that every experiment can be seen as a time ordered set of random variables which describes the time evolving of the sea surface at *location A*, that is as one of the possible *realization* of the *ensamble* of the realizations of a *Stochastic Process* which can carried out [43] [34]. Therefore, to indicate the Stochastic Process sea surface elevation in presence of waves η , it is possible to write

$$\eta(t) = \{\eta_1(t), \eta_2(t), \dots, \eta_i(t), \dots\} \quad (2.91)$$

with $0 < i \leq \infty$ and

$$\eta_i(t) = \{\underline{\eta}(t_1), \underline{\eta}(t_2), \dots, \underline{\eta}(t_j), \dots\} \quad (2.92)$$

with $0 < j \leq \infty$.

Identity 2.91 describes the general moved by waves surface Stochastic process and the braces $\{\}$ indicate the *ensamble* of all the possible i -th realizations, while equation 2.92 indicates that every η_i realization is an ordered set of the j -th random variables $\underline{\eta}(t_j)$ (the $\underline{\bullet}$ stands for random variable).

As anyone can easily verify, every realization is composed by random variables $\underline{\eta}(t)$ which are, at short time intervals, related and correlated: if the surface elevation $\underline{\eta}(t_i)$ at time t_i is large, then, at time t_j , with $j > i$ and $t_i - t_j$ enough small, the surface elevation $\underline{\eta}(t_j)$ will be large too; only when the time interval $t_i - t_j$ become large the correlation between $\underline{\eta}(t_i)$ and $\underline{\eta}(t_j)$ will be lost.

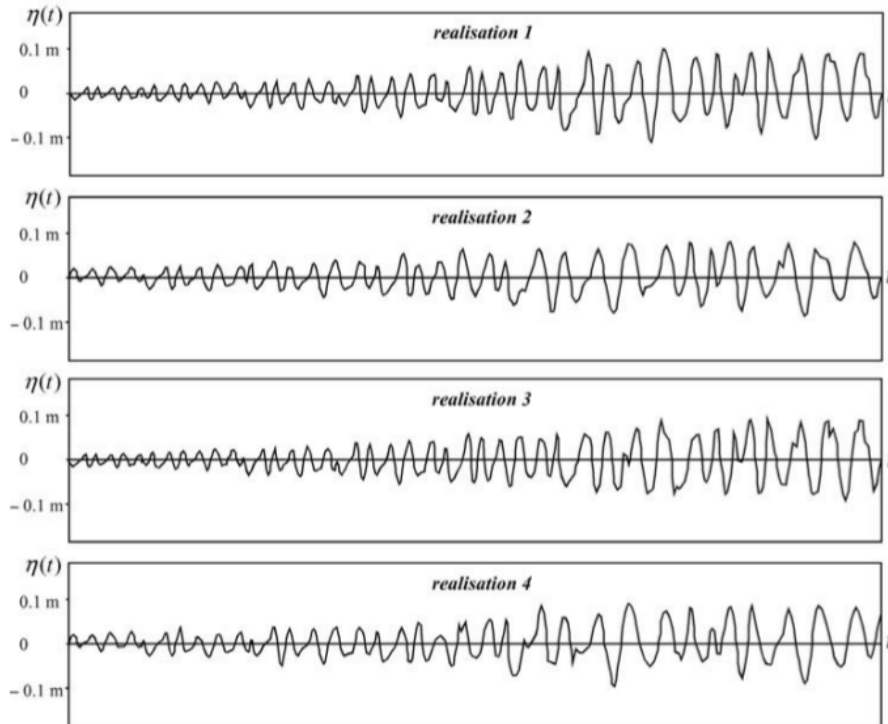


Fig. 2.12: Time series of four statistically identical realizations of the surface elevation at location A, in the laboratory tank of figure 2.11 (modified from [43]).

The validity of the *Random Phase-Amplitude model* described in the next paragraph is based on the fact that the surface elevation of wind-generated

waves can be considered as a *Stationary, Gaussian, Ergodic* stochastic process.

The applicability of the above three conditions for random sea waves has not been rigorously verified [34].

Talking about *Stationarity* and *Ergodicity*, the validity of their assumption is impossible to verify because it is impossible to collect a true ensemble of wave record for a prescribed sea state, due to the fact that the sea state is intrinsically random and it is always changing in time and space [34].

However, it is not very far from reality if the sea state is expected to be constant for a short duration of several minutes to a few tens of minutes and therefore, for such short wave record, *Stationarity* is assumed.

Concerning to *Ergodicity*, it is usually assumed that it holds for sea waves because there is no evidence that it does not [34].

Thinking about surface elevation of wind-waves as a *Gaussian* process can be considered reasonable if some assumptions are made.

The surface elevation at any moment in time t_i can be seen as the sum of the elevations at that time of a large number of simple sinusoidal waves, each of which has been generated and has traveled independently from the others: therefore, according to the *Central Limit Theorem*, the sea surface elevation should be *Gaussian distributed*. There are problems with this reasoning when we think about the correlation between random variables $\underline{\eta}(t_i)$ and $\underline{\eta}(t_j)$ separated in time by a short time lag: in this situations the variables can not be defined as independent and the *Central Limit Theorem* does not hold.

Hence, sea wave surface displacement can be considered a *Gaussian* stochastic process if we are not in the surf zone (i.e., in shallow water) and the waves are not too steep: waves in these conditions can be reasonable seen as independent one from each other [43].

2.2.3 The Random Phase-Amplitude model

The *Random Phase-Amplitude model* leads to the *Ocean Wave Spectrum* concept, which is a way to describe the sea surface as a stochastic process, characterizing all possible *realizations* that could have been made under the same conditions, rather than to describe in detail a given observation (i.e., a single realization) [43] .

Assuming that sea surface gravity waves can be treated as a *Stationary, Gaussian, Ergodic* stochastic process, which means to consider as true the three conditions exposed in 2.2.2, the random sea waves surface can be interpreted as a superposition of sinusoidal free progressive waves generated by wind in different times and places (see figure 2.13) and, according to Fourier series Theory, it is possible to write, for a given location on the ocean surface [43] [34] :

$$\underline{\eta}(t) = \sum_{n=1}^N \underline{a}_n \cos(2\pi f_n t + \underline{\varepsilon}_n) \quad (2.93)$$

where N is a large number, \underline{a}_n and $\underline{\varepsilon}_n$ are, respectively, the *amplitude* and *phase* random variables of each discrete *frequency* $f_n = n/D$, with $n = 1, 2, \dots, N$ and D as the time length of the stochastic process (therefore $\Delta f = 1/D$).

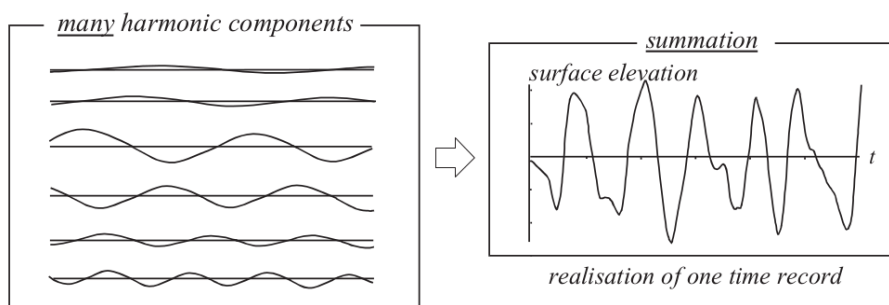


Fig. 2.13: Superposition of many harmonic waves, with constant but randomly chosen amplitudes and phases, to create a random sea surface (modified from [43]).

The phases $\underline{\varepsilon}_n$ and amplitudes \underline{a}_n , being random variables, are fully described by their respective probability density function.

As the amplitude of an ocean wave is

$$a = \frac{H}{2}, \quad (2.94)$$

where H is the *wave height* defined in section 2.2.1, and H is Rayleigh distributed (see always 2.2.1), also \underline{a}_n is Rayleigh distributed with the following probability density function:

$$p(\underline{a}_n) = \frac{\pi \underline{a}_n}{2 \mu_n^2} \exp\left(-\frac{\pi \underline{a}_n^2}{4 \mu_n^2}\right) \quad \text{for} \quad \underline{a}_n \geq 0 \quad (2.95)$$

where μ_n is the *expected value* of the amplitude \underline{a}_n

$$\mu_n = E\{\underline{a}_n\} \quad (2.96)$$

Since μ_n is the only parameter in equation 2.95, \underline{a}_n is fully statistically described by this one parameter.

Concerning to $\underline{\varepsilon}_n$, the *Random Phase-Amplitude model* assumes that the phase at each frequency f_n is uniformly distributed between 0 and 2π (i.e., it is treated as a *white noise*).

Considering densely distributed frequencies f_n (i.e., $f_{n+1} - f_n$ is small if compared to some characteristic wave frequencies), it is possible to write the function that describes the spreading of this mean amplitude $E\{\underline{a}_n\}$ along the frequencies axis, and it is called the *amplitude spectrum* (see figure 2.14).

Consider now the *variance* of the sea surface elevation $\underline{\eta}(t)$; by definition, it is the expected value of the squared surface elevation (relative to its mean)

$$\sigma_t^2 = E\{(\underline{\eta}(t) - \mu_t)^2\} \quad (2.97)$$

where the subscript \bullet_t means that the variance and the mean are referred to the *ensemble* of all the possible realizations of $\underline{\eta}$ which can be made at time t .

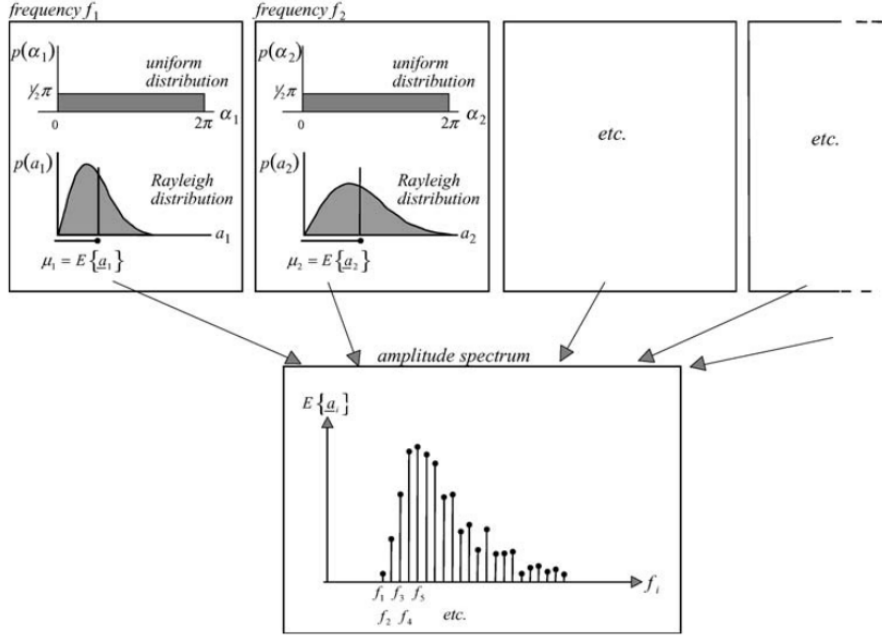


Fig. 2.14: According to the *Random Phase-Amplitude model*, for each frequency f_n there is a uniformly distributed random phase and one Rayleigh distribution for the random amplitude. The expected value of the amplitude as a function of frequency is shown in the bottom panel. (modified from [43]).

Usually, the mean value of the surface is taken to be 0, so that the variance become

$$\sigma_t^2 = E\{\underline{\eta}^2(t)\} \quad (2.98)$$

and it is related directly with the amplitude of the wave. Assuming now that the hypothesis of stationarity yields, we can write

$$\sigma^2 = E\{\underline{\eta}^2(t)\} = \overline{\eta^2(t)} \quad (2.99)$$

where the overbar indicates time averaging over the time length D of the stochastic process which is considered to be a multiple of the wave period. Therefore, we can write

$$\sigma^2 = \overline{\eta^2(t)} = \frac{1}{D} \int_0^D \underline{\eta}^2(t) dt = \frac{1}{2} a^2 \quad (2.100)$$

with $D = nT$ and remembering that the time average of the $\cos^2 x$ over a wave length is $1/2$.

In the *Random Phase-Amplitude model* a large number of harmonic waves is superimposed: the *variance of this sum*, i.e. the variance $E\{\underline{\eta}^2(t)\}$ of the surface elevation, is equal to *the sum of the individual variances* $E\{\frac{1}{2}a_n^2\}$:

$$E\{\underline{\eta}^2(t)\} = \sum_{n=1}^N E\{\frac{1}{2}a_n^2\} \quad (2.101)$$

Considering therefore equation 2.101 and remembering that the *Linear Theory* for surface gravity waves shows that the energy of the wave is proportional to the variance (see 2.56), it is clear that it is more meaningful to distribute the variance of each wave component $E\{\frac{1}{2}a_n^2\}$ over the frequencies f_n rather than the amplitude $E\{a_n\}$, i.e., it is more helpful to use the *variance spectrum* instead of the *amplitude spectrum*.

Since both the *variance spectrum* and the *amplitude spectrum* are based on discrete frequencies, in order to obtain a function which fully describes sea surface waves (where all frequencies are present), it is needed to distribute the variance $E\{\frac{1}{2}a_n^2\}$ over the frequency interval Δf_n for each frequency f_n and to impose that the frequency band Δf_n approach to 0.

By doing so, the function *variance density spectrum* $S(f)$ is defined as

$$S(f) = \lim_{\Delta f \rightarrow 0} \frac{1}{\Delta f} E\{\frac{1}{2}a^2\}, \quad m^2/Hz \quad (2.102)$$

and it gives a complete statistical description of the surface elevation of the ocean waves if they are assumed to be a *Stationary, Ergodic, Gaussian* stochastic process.

The *variance density spectrum* provides information on how much variance a given frequency f_n contributes to the total variance, and, extending equation 2.101 to the continuous, it is possible to write

$$E\{\underline{\eta}^2(t)\} = \overline{\eta^2}(t) = \int_0^\infty S(f)df \quad (2.103)$$

From equation 2.56, it is possible to link the *variance density spectrum* to the *total energy* of a wave and write:

$$E_{tot} = \rho g \int_0^\infty S(f)df \quad (2.104)$$

allowing to define the frequency spectrum $S(f)$ as the *variance density spectrum* or as the *energy density spectrum* indiscriminately.

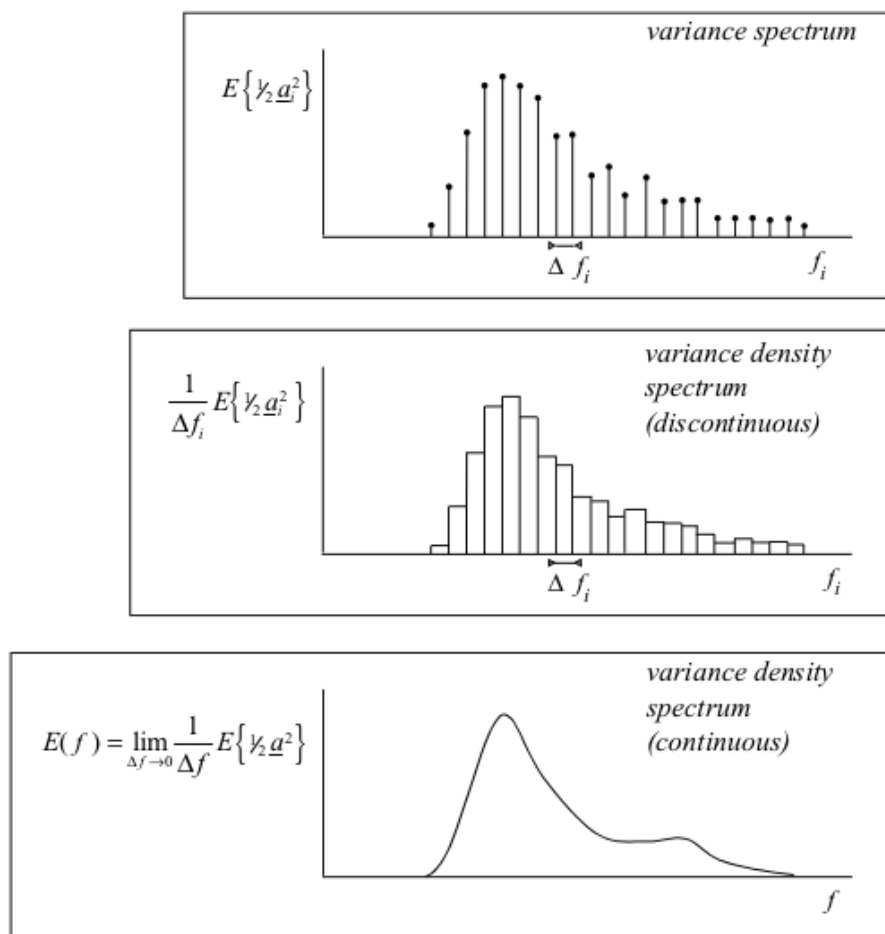


Fig. 2.15: The transformation of the discrete *variance spectrum* to the continuous *variance density spectrum*(modified from [43]).

The Frequency-Directional Spectrum

The frequency spectrum defined in 2.102 is a function of the lonely time and fully described the Stationary, Ergodic, Gaussian surface elevation process at one given location in the ocean.

In order to describe the real *three-dimensional* random sea waves, it is needed to extend the *Random Phase-Amplitude model* to the 3 – *D* case.

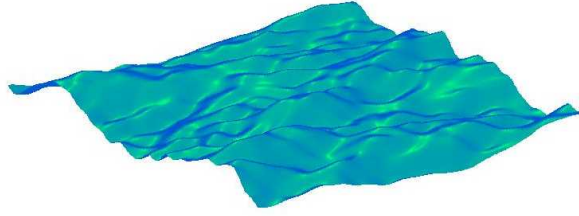


Fig. 2.16: Computer Simulation of Random Sea Waves surface displacement

According to the *Linear Theory*, the random sea waves surface can be interpreted as a superposition of sinusoidal free progressive waves generated by wind in different times and places:

$$\underline{\eta}(\vec{x}, t) = \sum_{n=1}^N \sum_{m=1}^M \underline{a}_{n,m} \cos(K_n \cos \theta_m \hat{i} + K_n \sin \theta_m \hat{j} - \omega_n t + \underline{\varphi}_{n,m}) \quad (2.105)$$

where $\underline{a}_{n,m}$ is the *amplitude*, K_n is the magnitude of the wavenumber vector (i.e., $|\vec{K}_n|$), θ_m is the angle between the x -axis and the direction of wave propagation and \hat{i} and \hat{j} are the fundamental versors in the x and y direction respectively, ω_n is the *absolute* or *intrinsic* frequency defined as $\omega_n = 2\pi f_n + \vec{U} \cdot \vec{K}_n$ and $\varphi_{n,m}$ is the *phase* of the $(n, m)^{th}$ wave component.

If the harmonic wave components are independent their *dispersion relationship* is:

$$\omega_n^2 = gK_n \tanh(K_n h) \quad (2.106)$$

where g is the *gravity acceleration* and h is the total mean *water depth* defined as $h = \bar{\zeta} + h_b$, where $\bar{\zeta}(\vec{x}, t)$ is the mean free surface displacement and

$h_b(\vec{x})$ is the depth of the bottom with respect to the unperturbed surface level.

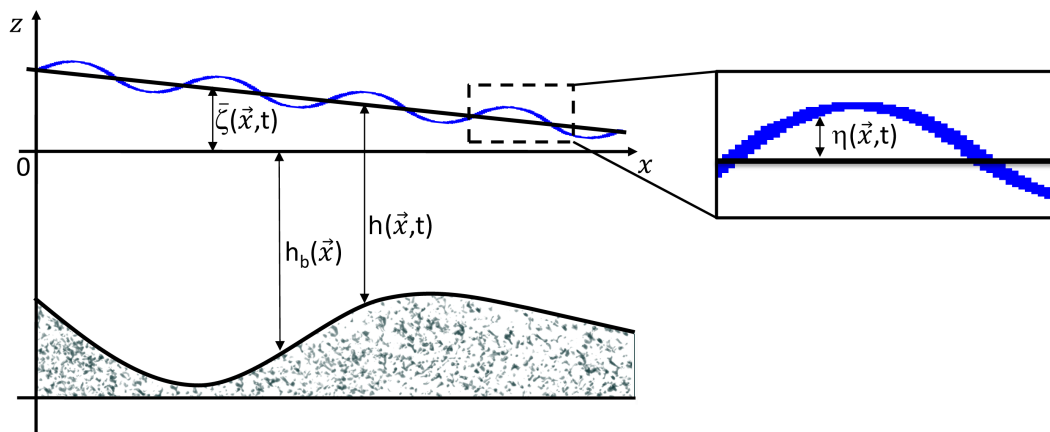


Fig. 2.17: Wave system physical problem in the xz - plane

As in the one dimensional model, every random amplitude $\underline{a}_{n,m}$ is Rayleigh distributed and each random phase $\underline{\varphi}_{n,m}$ is uniformly distributed between $0 - 2\pi$.

Considering frequencies and directions densely distributed between their properly ocean range, following the same techniques as before, a continuous *two-dimensional* variance density spectrum can be defined, so that, for all n and m , we have

$$S(f, \theta) = \lim_{\Delta\theta \rightarrow 0} \lim_{\Delta f \rightarrow 0} \frac{1}{\Delta\theta} \frac{1}{\Delta f} E\left\{\frac{1}{2}a^2\right\}, \quad m^2/Hz/rad \quad (2.107)$$

or, in terms of *absolute* frequency ω

$$S(\omega, \theta) = \lim_{\Delta\theta \rightarrow 0} \lim_{\Delta\omega \rightarrow 0} \frac{1}{\Delta\theta} \frac{1}{\Delta\omega} E\left\{\frac{1}{2}a^2\right\}, \quad (2.108)$$

where

$$S(\omega, \theta) = \frac{1}{2\pi} S(f, \theta) \quad (2.109)$$

The *two-dimensional* spectrum $S(f, \theta)$ shows how the variance of $\underline{\eta}(\vec{x}, t)$ is distributed over frequencies and directions just as the *one-dimensional* spectrum $S(f)$ shows how the variance of $\underline{\eta}(t)$ is distributed over frequencies. Therefore, the volume of $S(f, \theta)$ is the total variance $\underline{\eta}^2$ of the sea surface elevation

$$E\{\underline{\eta}^2(\vec{x}, t)\} = \overline{\eta^2}(\vec{x}, t) = \int_0^{2\pi} \int_0^\infty S(f, \theta) d\theta df \quad (2.110)$$

and, obviously yields,

$$S(f) = \int_0^{2\pi} S(f, \theta) d\theta \quad (2.111)$$

An example of the energy wave spectrum expressed in function of frequency $S(f)$ and in function of frequency and direction $S(f, \theta)$ is shown in fig. 2.18.

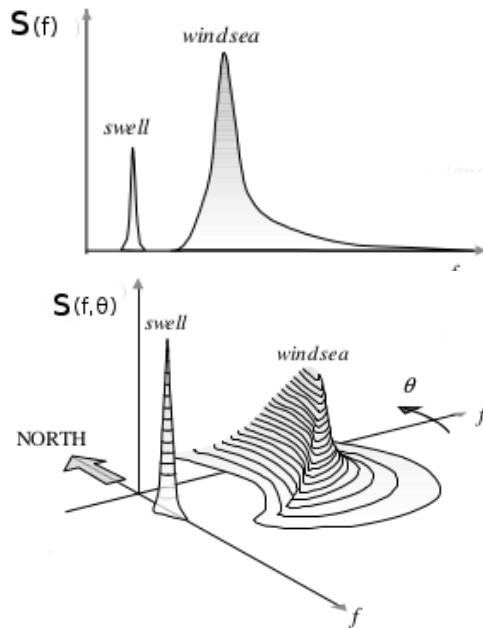


Fig. 2.18: Variance Density Spectrum $S(f)$ and $S(f, \theta)$ (modified from [76]).

Statistical Theory of Irregular Waves enables to calculate some statistical integral wave parameters, like *Significant Wave Height* and *Mean Wave Period*, from *Energy Density Spectra*. Defining the n -th moment of the *Energy Density Spectrum* as

$$m_n = \int_0^{\infty} f^n S(f) df \quad (2.112)$$

it can be proved that the *Significant Wave Height*, $H_{1/3}$, and the *Mean Wave Period*, \bar{T} are given by

$$H_{1/3} \simeq H_{m_0} = 4\sqrt{m_0} \quad (2.113)$$

$$\bar{T} = \sqrt{\frac{m_0}{m_2}} \quad (2.114)$$

where H_{m_0} indicates the significant wave height estimated from the Rayleigh energy spectrum distribution, and $m_0 = \langle \eta^2 \rangle$ is the variance of the sea surface elevation.

Parametric Spectra

The frequency-direction spectrum for a random gravity waves field $S(f, \theta)$ can be directly calculated using a third generation wind-wave model, as SWAN, or parameterized using some empirical formulas.

One of these is the **Pierson-Moskowitz model spectrum**, which is based on the assumption that if the wind blow steadily for a long time over a large area the waves would come into equilibrium with the wind. This is the concept of a *fully developed sea* (a sea produced by winds blowing steadily over hundreds of miles for several days) [78].

In order to obtain a spectrum of a fully developed sea, Pierson and Moskowitz measured sea waves by accelerometers on British weather ships in the North Atlantic.

First, they selected wave data for times when the wind had blown steadily for long times over large areas of the North Atlantic.

Then they calculated the wave spectra for various wind speeds, founding that the frequency spectra were of the form

$$S_P(\omega) = \frac{\alpha g^2}{\omega^5} \exp\left(-\beta\left(\frac{\omega_0}{\omega}\right)^4\right) \quad (2.115)$$

where $\omega = 2\pi f$, f is the wave frequency in Hertz, $\alpha = 8.1 \times 10^{-3}$, $\beta = 0.74$, $\omega_0 = g/U_{19.5}$ and $U_{19.5}$ is the wind speed at a height of 19.5 m above the sea surface (i.e., the height of the anemometers on the weather ships used by Pierson and Moskowitz, [78]).

The frequency of the peak of the Pierson-Moskowitz spectrum can be calculated by solving $dS/d\omega = 0$ for ω_p , to obtain

$$\omega_p = \frac{0.877g}{U_{19.5}} \quad (2.116)$$

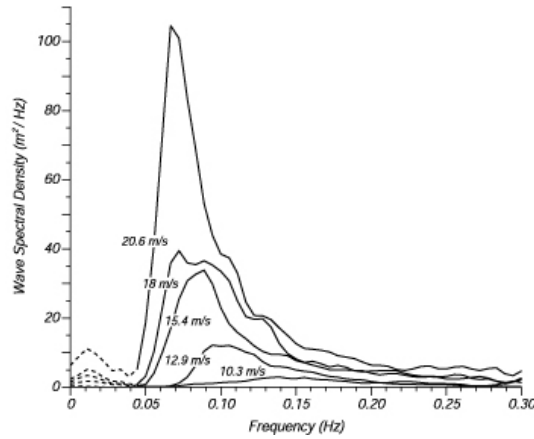


Fig. 2.19: Wave spectra of a fully developed sea for different wind speeds according to [78]

For practical reasons, it has become standard to relate the variables to the main sea state parameters rather than wind speed, and to use slightly different values so that the Pierson-Moskowitz spectrum can be expressed as

$$S_P(\omega) = \frac{\alpha g^2}{\omega^5} \exp\left[-\frac{5}{4}\left(\frac{\omega_p}{\omega}\right)^4\right] \quad (2.117)$$

where ω_p is the frequency of the peak and α is Phillips constant.

Hasselmann *et al.* [41], after analyzing data collected during the Joint North Sea Wave Observation Project JONSWAP, found that the wave spectrum is never fully developed: it continues to develop through non-linear wave-wave interactions even for very long times and distances. In order to consider this interactions, an extra and somewhat artificial factor was added to the Pierson-Moskowitz spectrum to improve the fit to their measurements.

The JONSWAP spectrum is therefore a Pierson-Moskowitz spectrum multiplied by an extra peak enhancement factor γ^r

$$S_J(\omega) = \frac{\alpha g^2}{\omega^5} \exp \left[-\frac{5}{4} \left(\frac{\omega_p}{\omega} \right)^4 \right] \gamma^r \quad (2.118)$$

with

$$r = \exp \left[-\frac{(\omega - \omega_p)^2}{2\sigma^2\omega_p^2} \right] \quad (2.119)$$

Wave data collected during the JONSWAP experiment were used to determine the values for the constants in equations 2.118 and 2.119:

$$\alpha = 0.076 \left(\frac{U_{10}^2}{F g} \right)^{0.22} \quad (2.120)$$

$$\omega_p = 22 \left(\frac{g^2}{U_{10} F} \right)^{1/3} \quad (2.121)$$

$$\gamma = 3.3 \quad (2.122)$$

$$\sigma = \begin{cases} 0.07 & \omega \leq \omega_p \\ 0.09 & \omega > \omega_p \end{cases} \quad (2.123)$$

where F is the distance over which the wind blows with constant velocity (*the fetch*).

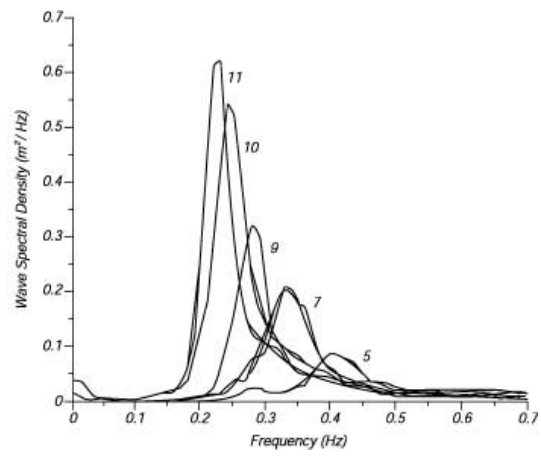


Fig. 2.20: Wave spectra of a developing sea for different fetches according to [41]

2.3 Description of the Wind-Wave SWAN Numerical Model

The aim of this chapter is to describe the main structure and features of the SWAN wind-wave model.

The remainder of this chapter presents the main features of the SWAN model, focusing on the governing equations, physical processes which are important in wind wave generation and dissipation and numerical schemes adopted by SWAN to solve the equations.

SWAN is a third generation spectral wave model developed by Booij et al. [10] which can be applied in a wide range of coastal applications, being effective from high resolution coastal areas up to quasi oceanic scales.

In order to comprehend how such a model works a brief description of the developments in wave forecasting over the past 50 years is given in the next paragraph.

2.3.1 Wind-Wave Models

Wind-waves represent that portion of the ocean wave spectrum that is generated by wind forcing at the sea surface.

A typical wind-wave spectrum at the ocean surface is generally composed by the so called 'swell' part, waves with a period range of 4 - 20 sec generated by remote winds, and the 'wind sea' part, which describes waves generated by local winds with frequencies between 4 and 1 sec.

Due to the specific random and irregular nature of wind blowing, a deterministic approach to describe the sea surface displacement is generally not possible.

During the Second World War, the interest of the scientific community in ocean waves and operational prediction increased because of marine military operations, and it was in the early 1960s that many experiments proved that statistical properties of the ocean surface, like average wave height, periods and directions, seem to vary more slowly than the magnitude of temporal

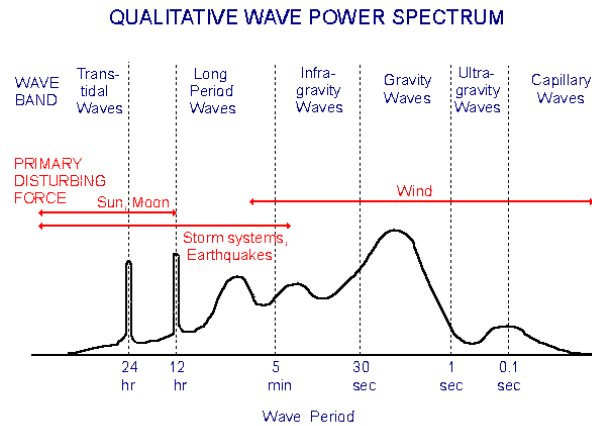


Fig. 2.21: Typical ocean wave spectrum (from [9])

and spatial scales typical of wind waves, laying the basis for the development of the statistical theory of ocean waves and suggesting the energy balance equation as the governing evolution equation for the ocean wave spectrum (see [47]).

The energy balance equation states that wave spectrum evolution is determined both by the effects of advection and refraction and by the sum of physical processes that contribute to generate (i.e. wind input) and dissipate (i.e wave breaking and nonlinear interactions) wave energy.

Although the energy balance equations are demonstrated and fully accepted by all the community, researchers, forced by the low computational power of computers in those years, in 1960 developed the so called first-generation spectral wave models, which were based only on wave energy advection, wind input and a primitive kind of white-capping dissipation, neglecting nonlinear interactions considered not so important in waves spectra evolution.

These kind of forecasting models were used for many years with important results, but since the beginning it was clear that their formulation was not suitable to represent all the physical processes implied in wave generation.

Even if in the earlier 1970s many field surveys proved the importance of non-linear wave-wave interactions for the rapid growing of the low-frequency part of the spectrum and that non-linear interactions take part in control the shape of the spectrum, computational power still represented a limiting factor and researchers developed the so called second-generation models.

The theory behind these models was based on the fact that time scales of

non-linear interactions are faster than those of the other processes that controls spectral shape and that for relatively steady forcing conditions (fully developed wind wave) spectra can be approximated by a standard quasi-equilibrium parametric spectral distribution, like JONSWAP or Pierson-Moskowitz ones.

The formulation of these kind of model was certainly more correct and accurate than the first-generation ones, but they could not be applied in rapidly changing wind forcing situations.

In the 1980s, with the rise of super computers and radar technologies, the scientific community began to develop full spectral models based on explicit representation of all physical processes implied in sea waves, the so called third-generation models. Nowadays third-generation models are used in many operational fields, from engineering to sea state forecasting and the most used are WAM, WAVEWATCH III and SWAN, respectively developed by the WAMDI Group, NOAA/NCEP and Delft University of Technology.

2.3.2 Spectral action balance equation

Random sea waves, at a fixed point of the sea surface and at a certain time, are completely described by the variance density spectrum $S(\sigma, \theta)$ (see section 2.2.3).

The evolution in time, space and spectral space of the energy density spectrum $S(\vec{x}, t; \sigma, \theta)$ is given by the *energy balance equations*

$$\frac{DS(\vec{x}, t; \sigma, \theta)}{Dt} = S_{tot} \quad (2.124)$$

where the operator D/Dt denotes the total derivative which is defined as

$$\frac{D\bullet}{Dt} = \frac{\partial\bullet}{\partial t} + \nabla_h \cdot [(\vec{c}_g + \vec{u}) \bullet] + \frac{\partial[\vec{c}_\sigma \bullet]}{\partial \sigma} + \frac{\partial[\vec{c}_\theta \bullet]}{\partial \theta} \quad (2.125)$$

in which $\vec{c}_g = \partial\sigma/\partial\vec{k}$ is the relative group velocity, \vec{u} is the current velocity field, the quantities $c_\sigma = d\sigma/dt$ and $c_\theta = d\theta/dt$ represents propagation velocities in spectral space (σ, θ) and the operator ∇_h is defined as $\nabla_h = \left(\frac{\partial}{\partial x}, \frac{\partial}{\partial y}\right)$. S_{tot} stands for the net *source* term resulting from the sum of source and sink terms which parameterize all physical processes involved in the generation, dissipation and redistribution of wave energy and which will be briefly described in the following section.

Usually, third generation models resolve the *action balance equation* instead of the energy balance equation, where the *action density* N is defined as

$$N = \frac{S}{\sigma} \quad (2.126)$$

The action balance equation can be written therefore as

$$\frac{\partial N}{\partial t} + \frac{\partial(c_x N)}{\partial x} + \frac{\partial(c_y N)}{\partial y} + \frac{\partial(c_\sigma N)}{\partial \sigma} + \frac{\partial(c_\theta N)}{\partial \theta} = \frac{S_{tot}}{\sigma} \quad (2.127)$$

where, using *dispersion relationship* and *conservation of number of wave crest equation* (see [69]),

$$\frac{d\vec{x}}{dt} = (c_x, c_y) = \vec{c}_g + \vec{u} = \frac{1}{2} \left(1 + \frac{2|\vec{k}|h}{\sinh(2|\vec{k}|h)} \right) \frac{\sigma \vec{k}}{|\vec{k}|^2} + \vec{u} \quad (2.128)$$

$$\frac{d\sigma}{dt} = c_\sigma = \frac{\partial \sigma}{\partial h} \left(\frac{\partial h}{\partial t} + \vec{u} \cdot \nabla_h h \right) - c_g \vec{k} \cdot \frac{\partial \vec{u}}{\partial s} \quad (2.129)$$

$$\frac{d\theta}{dt} = c_\theta = -\frac{1}{k} \left(\frac{\partial \sigma}{\partial h} \frac{\partial h}{\partial m} + \vec{k} \cdot \frac{\partial \vec{u}}{\partial m} \right) \quad (2.130)$$

where c_x , c_y are the propagation velocities of wave energy in x - y space, c_σ and c_θ are the propagation velocities in spectral space, h is the total mean depth defined as $h = \bar{\zeta} + h_b$, being $\bar{\zeta}(\vec{x}, t)$ the mean free surface displacement and $h_b(\vec{x})$ the depth of the bottom with respect to the unperturbed surface level, s is the space coordinate in the wave propagation direction of θ and m is a coordinate perpendicular to s . The expression for c_θ is presented here without diffraction effects.

The left hand side of 2.127 is the kinematic part. In particular the second term represents the propagation of wave energy due to advection, the third term denotes the effect of shifting of the relative frequency σ due to variations in mean currents and depth and the fourth term stands for depth-induced and current-induced refraction.

For coastal-small scales problems equation 2.127 is used.

For oceanic or shelf sea scales applications, equation 2.127 for $N(x, y; \sigma, \theta)$ can be related to spherical coordinates longitude (λ) and latitude (φ), considering that θ is the wave direction taken counterclockwise from geographic

East, as

$$\frac{\partial N}{\partial t} + \frac{\partial c_\lambda N}{\partial \lambda} + \frac{1}{\cos \phi} \frac{\partial c_\varphi \cos \varphi N}{\partial \varphi} + \frac{\partial c_\sigma N}{\partial \sigma} + \frac{\partial c_{\bar{\theta}} N}{\partial \theta} = \frac{S_{tot}}{\sigma} \quad (2.131)$$

where the propagation velocities in x - y and σ - θ space are given by

$$c_\lambda = \frac{d\lambda}{dt} = (c_g \cos \theta + u_\lambda)(R \cos \varphi)^{-1} \quad (2.132)$$

$$c_\varphi = \frac{d\varphi}{dt} = (c_g \sin \theta + u_\varphi)R^{-1} \quad (2.133)$$

$$c_\sigma = \frac{d\sigma}{d\bar{h}} \left(\frac{\partial \bar{h}}{\partial t} + \vec{u} \cdot \nabla_h \bar{h} \right) - c_g \vec{k} \cdot \frac{\partial \vec{u}}{\partial s} \quad (2.134)$$

$$c_{\bar{\theta}} = c_\theta - \frac{c_x \cos \theta + c_y \sin \theta}{R} \cos \theta \tan \varphi \quad (2.135)$$

2.3.3 Sources and sinks

In *deep water*, the net source term S_{tot} is the result of the sum between the wind-wave interaction S_{in} and the non-linear four-wave interactions S_{nl4} input terms and the whitecapping dissipation S_{wc} term

$$S_{tot} = S_{in} + S_{nl4} + S_{whc} \quad (2.136)$$

while in *shallow water* it includes also the non-linear three-wave interactions S_{nl3} source term and the wave decay due to bottom friction S_{bot} and depth-induced wave breaking S_{wbr}

$$S_{tot} = S_{in} + S_{nl4} + S_{nl3} + S_{whc} + S_{bot} + S_{wbr} \quad (2.137)$$

In the following sections, for each term a brief summary of the theory behind the parameterization and the complete mathematical formulation used in the relocatable model is given.

Input by Wind

According to Phillips-Miles *Theory of Wave Generation*, the wind-wave energy transfer can be described by the sum of two processes, an initial *resonance mechanism*, which is responsible for the early stages of wave growth

and which provides a linear in time energy input, and a following *feed-back mechanism*, which states that wind-wave interaction is responsible for an energy transfer which varies exponentially in time allowing the wave grows as it gets larger. Hence, wave growth due to wind can be written as

$$S_{in}(\sigma, \theta) = A + BS(\sigma, \theta) \quad (2.138)$$

where A describes the linear growth and BS the exponential growth and both depend on wave frequency and direction, and wind speed and direction.

For wave growth parameterization SWAN uses wind friction velocity U_* while it is driven by the wind speed at 10m elevation U_{10} . Friction velocity U_* is obtained by

$$U_*^2 = C_D U_{10}^2 \quad (2.139)$$

where C_D is the drag coefficient expressed according to Wu as

$$C_D = \begin{cases} 1.2875 \times 10^{-3}, & \text{if } U_{10} < 7.5 \text{ m s}^{-1} \\ (0.8 + 0.065 \text{ s m}^{-1} \times U_{10}) \times 10^{-3}, & \text{if } U_{10} \geq 7.5 \text{ m s}^{-1} \end{cases} \quad (2.140)$$

The linear growth term A is expressed using the Cavaleri and Melanotte-Rizzoli [16] formulation with a filter to eliminate wave growth at frequencies lower than the Pierson-Moskowitz frequency:

$$A = \frac{1.5 \times 10^{-3}}{2\pi g^2} (U_* \max[0, \cos(\theta - \theta_w)])^4 H \quad (2.141)$$

where θ_w is the wind direction and H is the filter defined as

$$H = \exp \left\{ - \left(\frac{\sigma}{\sigma_{PM}^*} \right)^{-4} \right\} \quad (2.142)$$

using the peak frequency of the fully developed sea σ_{PM}^* defined as

$$\sigma_{PM}^* = \frac{0.13g}{28U_*} 2\pi \quad (2.143)$$

Three optional expressions for the exponential growth by wind B are available:

- 1) The first expression is due to Snyder et al. [95] rescaled in terms of friction velocity U_* by Komen et al. [59]:

$$B = \max \left[0, 0.25 \frac{\rho_a}{\rho_w} \left(28 \frac{U_*}{c_{ph}} \cos(\theta - \theta_w) - 1 \right) \right] \sigma \quad (2.144)$$

in which c_{ph} is the phase speed and ρ_a and ρ_w are the air and water density, respectively.

2) The second is due to Janssen [49][51]; it is based on a quasi-linear wind-wave theory and is given by

$$B = \beta \frac{\rho_a}{\rho_w} \left(\frac{U_*}{c_{ph}} \right)^2 \max[0, \cos(\theta - \theta_w)]^2 \sigma \quad (2.145)$$

where β is the Miles constant estimated in Janssen's theory from the non-dimensional critical height λ as

$$\begin{cases} \lambda = \frac{gz_e}{c_{ph}^2} e^r, & r = \kappa c / |U_* \cos(\theta - \theta_w)| \\ \beta = \frac{1.2}{\kappa^2} \lambda \ln^4 \lambda, & \text{for } \lambda \leq 1 \\ \beta = 0, & \text{for } \lambda > 1 \end{cases} \quad (2.146)$$

where $\kappa = 0.41$ is the Von Karman constant and z_e is the effective surface roughness. Janssen in his theory assumes a logarithmic wind profile given by

$$U(z) = \frac{U_*}{\kappa} \ln \left[\frac{z + z_e + z_0}{z_e} \right] \quad (2.147)$$

in which $U(z)$ is the wind speed at height $z = 10m$ above the mean water level, z_0 is the roughness length which is expressed by the Charnock-like relation

$$z_0 = \hat{\alpha} \frac{U_*^2}{g}, \quad \hat{\alpha} = 0.01 \quad (2.148)$$

and z_e is the effective roughness length which is given by

$$z_e = \frac{z_0}{\left(1 - \frac{|\vec{\tau}_w|}{\vec{\tau}} \right)^{\frac{1}{2}}} \quad (2.149)$$

where $\vec{\tau}_w$ is the wave induced stress and $\vec{\tau}$ is the total surface stress defined as

$$\vec{\tau}_w = \rho_w \int_0^{2\pi} \int_0^\infty \sigma B S(\sigma, \theta) \frac{\vec{k}}{k} d\sigma d\theta \quad (2.150)$$

$$\vec{\tau} = \rho_a |\vec{U}_*| \vec{U}_* \quad (2.151)$$

and which both parameterize the *sea state*. The value of U_* can be determined for a given wind speed U_{10} and a given wave spectrum $S(\sigma, \theta)$ from the above set of the equations and therefore in this formulation of the exponential wave growth the computation of U_* is an integral part of the source term.

- 3) The third formulation is a modified version of that by Yan [106], which is based on the fact that field observations of wave growth demonstrate that estimates of wind input rates follow the parameterizations of Snyder et al. [95] for weakly forced waves ($u_*/c < 0.1$) and that one of Plant [79] for strongly forced waves ($u_*/c > 0.1$). Because of this fact Yan proposes an analytical fit through these two wind-induced growth rates of waves given by

$$B = \left[D \left(\frac{u_*}{c} \right)^2 + E \left(\frac{u_*}{c} \right) + F \right] \cos(\theta - \alpha) + H \quad (2.152)$$

where D, E, F and H are coefficients of the fit. In SWAN the values of these parameters are somewhat different from those proposed by Yan and are:

$$\begin{cases} D = 4.0 \times 10^{-2} \\ E = 5.52 \times 10^{-3} \\ F = 5.2 \times 10^{-5} \\ H = -3.02 \times 10^{-4} \end{cases} \quad (2.153)$$

White-Capping

As waves grow, their steepness increases till a critical point when they break. This process is highly non linear and limits the wave growth with the lost of energy. This process depends on the existing energy in the waves and on the wave steepness.

Three optional formulations of whitecapping dissipation term are available, two based on the *pulse-based model* by Hasselmann [40] and one on the *saturation-based model* by Alves and Banner [2].

Pulse-Based Model

Whitecapping depends primarily on waves steepness and is formulated as

$$S_{ds,w}(\sigma, \theta) = -\Gamma \tilde{\sigma} \frac{k}{\tilde{k}} S(\sigma, \theta) \quad (2.154)$$

where $\tilde{\sigma}$ and \tilde{k} are the mean frequency and the mean wave number, respectively, and Γ is a steepness dependent coefficient.

The mean frequency $\tilde{\sigma}$ and the mean wave number \tilde{k} are defined as a function of the total wave energy E_{tot} as

$$\tilde{\sigma} = \left(E_{tot}^{-1} \int_0^{2\pi} \int_0^\infty \frac{1}{\sigma} S(\sigma, \theta) d\sigma d\theta \right)^{-1} \quad (2.155)$$

$$\tilde{k} = \left(E_{tot}^{-1} \int_0^{2\pi} \int_0^\infty \frac{1}{\sqrt{k}} S(\sigma, \theta) d\sigma d\theta \right)^{-2} \quad (2.156)$$

$$E_{tot} = \int_0^{2\pi} \int_0^\infty S(\sigma, \theta) d\sigma d\theta \quad (2.157)$$

The steepness dependent coefficient Γ , according to Günter formulation based on Janssen [51], is given by

$$\Gamma = C_{ds} \left((1 - \delta) + \delta \frac{k}{\tilde{k}} \right) \left(\frac{\tilde{s}}{\tilde{s}_{PM}} \right)^p \quad (2.158)$$

where C_{ds} , δ and p are 'wind input formulation' dependent coefficients, \tilde{s} is the overall wave steepness defined as

$$\tilde{s} = \tilde{k} \sqrt{E_{tot}} \quad (2.159)$$

and \tilde{s}_{PM} is the value of \tilde{s} for the Pierson-Moskowitz spectrum [78]:

$$\tilde{s}_{PM} = \sqrt{3.02 \times 10^{-3}} \quad (2.160)$$

Since the values of C_{ds} , δ and p depend on wind input formulation, two sets of coefficient are used:

- 1) For wind input by Komen et al. [59]:

$$C_{ds} = 2.36 \times 10^{-5} \quad (2.161)$$

$$\delta = 0 \quad (2.162)$$

$$p = 4 \quad (2.163)$$

- 2) For wind input by Janssen [51][50]:

$$C_{ds} = 4.10 \times 10^{-5} \quad (2.164)$$

$$\delta = 0.5 \quad (2.165)$$

$$p = 4 \quad (2.166)$$

Saturation-Based Model

Experimental findings seems to relate whitecapping dissipation to wave group hydrodynamics, involving to define a dissipation term that primarily depends on quantities that are local in the frequency spectrum.

Alves and Banner (2003) have given a formulation of this dissipation term which depends also on mean spectral steepness and wavenumber, while in SWAN the adaptation of Van der Westhuysen et al. [102] and Van der Westhuysen [101] is used, in which the dependencies on mean spectral steepness and wavenumber are removed allowing to give the following formulation:

$$S_{ds,break} = -C'_{ds} \left(\frac{B(k)}{B_r} \right)^{p/2} (\tanh(kh))^{(2-p_0)/4} \sqrt{gk} S(\sigma, \theta) \quad (2.167)$$

in which $B(k)$ is the azimuthal-integrated spectral saturation calculated as

$$B(k) = \int_0^{2\pi} c_g k^3 S(\sigma, \theta) d\theta \quad (2.168)$$

$B_r = 1.75 \times 10^{-3}$ is a threshold saturation level, $C'_{ds} = 5.0 \times 10^{-5}$ is a proportionality coefficient and p depends on a calibration parameter p_0 and on the $B(k)/B_r$ ratio, which is a measure of waves breaking or not-breaking.

To provide general background whitecapping dissipation of non-breaking waves, Van der Westhuysen [101] formulation uses the parameter settings of Komen et al. [59].

Bottom Friction

SWAN allows three optional bottom friction models all of which can be expressed in the following form:

$$S_{ds,b} = -C_b \frac{\sigma^2}{g^2 \sinh^2 kd} S(\sigma, \theta) \quad (2.169)$$

in which C_b is a bottom friction coefficient that generally depends on the bottom orbital motion represented by U_{rms} :

$$U_{rms}^2 = \int_0^{2\pi} \int_0^{\infty} \frac{\sigma^2}{\sinh^2 kd} S(\sigma, \theta) d\sigma d\theta \quad (2.170)$$

The three options are:

- 1) The empirical model of JONSWAP (Hasselmann *et al.* [41])
which uses $C_b = 0.038 \text{ m}^2\text{s}^{-3}$ for *swell conditions* and, according to Bouws and Komen [11], $C_b = 0.067 \text{ m}^2\text{s}^{-3}$ for *depth-limited wind-sea conditions*.
- 2) The drag law model of Collins [19]
which is based on a conventional formulation for periodic waves with the appropriate parameters adapted to suit a random wave field. The bottom friction coefficient is $C_b = C_f g U_{\text{rms}}$ with $C_f = 0.015$ (Collins, 1972).
- 3) The eddy-viscosity model of Madsen *et al.* [67]
which is based on a bottom friction factor which is a function of the bottom roughness height and the actual wave conditions. Their bottom friction coefficient is given by:

$$C_b = f_w \frac{g}{\sqrt{2}} U_{\text{rms}} \quad (2.171)$$

in which f_w is a non-dimensional friction factor estimated by using the formulation of Jonsson [53] and Madsen *et al.* [67].

Depth-Induced Wave Breaking

When the ratio of wave height over water depth exceeds a certain limit, waves start to break, dissipating energy rapidly. In extreme shallow water (surf zone), this process becomes dominant over all other processes.

In SWAN, the energy dissipation due to depth-induced breaking is expressed by the *bore-based model* of Battjes and Janssen [6] in which the mean rate of energy dissipation per unit horizontal area due to wave breaking D_{tot} is given by

$$D_{\text{tot}} = -\frac{1}{4} \alpha_{BJ} Q_b \left(\frac{\tilde{\sigma}}{2\pi} \right) H_{\text{max}}^2 = -\alpha_{BJ} Q_b \tilde{\sigma} \frac{H_{\text{max}}^2}{8\pi} \quad (2.172)$$

where α_{BJ} is the proportionality coefficient of the rate of dissipation which is set equal to 1 in SWAN, Q_b is the fraction of breaking waves, H_{max} is the maximum wave height that can exist at the given depth and $\tilde{\sigma}$ is a mean frequency defined as:

$$\tilde{\sigma} = E_{\text{tot}}^{-1} \int_0^{2\pi} \int_0^{\infty} \sigma S(\sigma, \theta) d\sigma d\theta \quad (2.173)$$

The fraction of depth-induced breakers (Q_b) is determined in SWAN with

$$Q_b = \begin{cases} 0, & \text{for } \beta \leq 0.2 \\ Q_0 - \beta^2 \frac{Q_0 - \exp(Q_0 - 1)/\beta^2}{\beta^2 - \exp(Q_0 - 1)/\beta^2}, & \text{for } 0.2 < \beta < 1 \\ 1, & \text{for } \beta \geq 1 \end{cases} \quad (2.174)$$

where $\beta = H_{rms}/H_{max}$, for $\beta \leq 0.5$, $Q_0 = 0$ and for $0.5 < \beta \leq 1$, $Q_0 = (2\beta - 1)^2$.

Including the spectral directions in the formulation of Eldeberky and Battjes [30], the dissipation for a spectral component per unit time is calculated in SWAN with:

$$S_{ds,br}(\sigma, \theta) = \frac{D_{tot}}{E_{tot}} S(\sigma, \theta) = -\frac{\alpha_{BJ} Q_b \tilde{\sigma}}{\beta^2 \pi} S(\sigma, \theta) \quad (2.175)$$

In SWAN, the maximum wave height H_{max} is given by

$$H_{max} = \gamma d \quad (2.176)$$

in which γ is the breaker parameter and d is the total water depth. According to Battjes and Janssen [6], a default value of $\gamma = 0.8$ is used.

Nonlinear Wave-Wave Interactions

Quadruplets

The quadruplet wave-wave interactions are computed with the Discrete Interaction Approximation (DIA) as proposed by Hasselmann et al. [42]. For the DIA of two quadruplet, frequencies configuration of wave number vectors of each quadruplet is:

$$\sigma_1 = \sigma_2 = \sigma, \sigma_3 = \sigma(1 + \lambda) = \sigma^+, \sigma_4 = \sigma(1 - \lambda) = \sigma^- \quad (2.177)$$

where λ is a coefficient with a default value of 0.25.

To satisfy the resonance conditions, wave number vectors of the first quadruplet with frequency σ_3 and σ_4 lie at an angle of $\theta_3 = -11.48^\circ$ and $\theta_4 = 33.56^\circ$ to the angle of the wave number vectors with frequencies σ_1 and σ_2 while in the second quadruplet, which is the mirror image of the first quadruplet, relative angles of wave number vectors with frequency σ_3 and σ_4 are

$\theta_3 = \theta^+ = 11.48^\circ$ and $\theta_4 = \theta^- = -33.56^\circ$.

The source term $S_{\text{nl4}}(\sigma, \theta)$ for the nonlinear transfer rate is given by:

$$S_{\text{nl4}}(\sigma, \theta) = S_{\text{nl4}}^*(\sigma, \theta) + S_{\text{nl4}}^{**}(\sigma, \theta) \quad (2.178)$$

where S_{nl4}^* refers to the first quadruplet and S_{nl4}^{**} to the second quadruplet. Using the DIA, which exchanges wave variance at all three wave number vectors involved in a quadruplet wave number configuration, the rate of change of wave variance due to the quadruplet interaction at the three frequency-direction bins can be written as (note that the expressions for S_{nl4}^{**} are identical to those for S_{nl4}^* for the mirror directions):

$$\begin{pmatrix} \delta S_{\text{nl4}}^*(\sigma, \theta) \\ \delta S_{\text{nl4}}^*(\sigma^+, \theta^+) \\ \delta S_{\text{nl4}}^*(\sigma^-, \theta^-) \end{pmatrix} = \begin{pmatrix} 2 \\ -1 \\ -1 \end{pmatrix} C_{\text{nl4}} (2\pi)^2 g^{-4} \left(\frac{\sigma}{2\pi}\right)^{11} \times \left[S^2(\sigma, \theta) \left\{ \frac{S(\sigma^+, \theta^+)}{(1+\lambda)^4} + \frac{S(\sigma^-, \theta^-)}{(1-\lambda)^4} \right\} - 2 \frac{S(\sigma, \theta) E(\sigma^+, \theta^+) S(\sigma^-, \theta^-)}{(1-\lambda^2)^4} \right] \quad (2.179)$$

where $C_{\text{nl4}} = 3 \times 10^7$ by default.

The wave variance density at the frequency-direction bins $S(\sigma^+, \theta^+)$ and $S(\sigma^-, \theta^-)$ is obtained by bi-linear interpolation between the four surrounding frequency-direction bins. Similarly, the rate of change of variance density is distributed between the four surrounding bins using the same weights as used for the bi-linear interpolation.

In the DIA algorithm, Eq. (2.179) (and its mirror image) is applied to all spectral bins in a discrete frequency-direction spectrum. An extended spectral grid is applied to compute the interactions in the frequency range affected by the parametric spectral tail.

Quadruplet interactions in shallow water with depth d , as suggested by WAMDI group [35], are obtained by multiplying the deep water nonlinear transfer rate with a scaling factor $R(k_p d)$:

$$S_{\text{nl4}}^{\text{finite depth}} = R(k_p d) S_{\text{nl4}}^{\text{deep water}} \quad (2.180)$$

where R is given by:

$$R(k_p d) = 1 + \frac{C_{sh1}}{k_p d} (1 - C_{sh2} k_p d) e^{C_{sh3} k_p d} \quad (2.181)$$

in which k_p is the peak wave number of the frequency spectrum. WAMDI group [35] proposes the following values of the coefficients: $C_{sh1} = 5.5$, $C_{sh2} = 5/6$ and $C_{sh3} = -5/4$.

In the shallow water limit, $k_p \rightarrow 0$ and the nonlinear transfer rate tends to infinity, allowing to define a lower limit of $k_p = 0.5$ which results in a maximum value of $R(k_p d) = 4.43$.

To increase the model robustness in case of arbitrarily shaped spectra, the peak wave number k_p is replaced by $k_p = 0.75\tilde{k}$.

Triads

In each spectral direction SWAN uses a slightly adapted version of the Discrete Triad Approximation (DTA) of Eldeberky and Battjes [30], the Lumped Triad Approximation (LTA) of Eldeberky [29], which can be written as

$$S_{nl3}(\sigma, \theta) = S_{nl3}^-(\sigma, \theta) + S_{nl3}^+(\sigma, \theta) \quad (2.182)$$

with

$$S_{nl3}^+(\sigma, \theta) = \max[0, \alpha_{EB} 2\pi c c_g J^2 |\sin \beta| \{S^2(\sigma/2, \theta) - 2S(\sigma/2, \theta)S(\sigma, \theta)\}] \quad (2.183)$$

and

$$S_{nl3}^-(\sigma, \theta) = -2S_{nl3}^+(2\sigma, \theta) \quad (2.184)$$

where α_{EB} is a tunable proportionality coefficient.

The biphas β is approximated with

$$\beta = -\frac{\pi}{2} + \frac{\pi}{2} \tanh\left(\frac{0.2}{Ur}\right) \quad (2.185)$$

with Ursell number Ur :

$$Ur = \frac{g}{8\sqrt{2}\pi^2} \frac{H_s T_{m01}^2}{d^2} \quad (2.186)$$

The triad wave-wave interactions are calculated only for $0 \leq Ur \leq 1$. The interaction coefficient J is taken from Madsen and Sørensen [68]:

$$J = \frac{k_{\sigma/2}^2(gd + 2c_{\sigma/2}^2)}{k_{\sigma}d(gd + \frac{2}{15}gd^3k_{\sigma}^2 - \frac{2}{5}\sigma^2d^2)} \quad (2.187)$$

Summary of physical processes in the Wind-Wave Model

In this paragraph, a summary of all the physical processes which can be used in the SWAN Wind-Wave Model to add or withdraw wave energy to or from a wave field is given in Table below.

Process	Authors
Linear wind growth	Cavaleri and Malanotte-Rizzoli [16]
Exponential wind growth	Snyder <i>et al.</i> [95] - Komen <i>et al.</i> [59]
	Janssen [49][51][50]
	Yan [106] (modified)
Whitecapping	Komen <i>et al.</i> [59]
	Janssen [51][50]
	Alves and Banner [2]
Bottom friction	JONSWAP [41]
	Collins [19]
	Madsen <i>et al.</i> [67]
Depth-induced breaking	Battjes and Janssen [6]
Quadruplets	Hasselmann <i>et al.</i> [42]
Triads	Eldeberky [29]

2.3.4 Numerical Schemes

Discretization of the Spectral Action Balance Equation 2.127 is carried out using the finite differences method.

Since all variables are a function of the x, y spatial dimensions, the frequency σ , the directions θ and the time t , in order to solve this equation it is needed to define an horizontal $x - y$ space, a $\sigma - \theta$ spectral space and a *time* window and discretize all of them.

In this section, the way in which the $x-y$ space and $\sigma-\theta$ space and the time window are discretized and the way in which the boundary and initial conditions are obtained in the Relocatable Wind-Wave Model are described.

Time Discretization

Let's consider the homogeneous part of equation (2.127)

$$\frac{\partial N}{\partial t} + \frac{\partial c_x N}{\partial x} + \frac{\partial c_y N}{\partial y} + \frac{\partial c_\sigma N}{\partial \sigma} + \frac{\partial c_\theta N}{\partial \theta}. \quad (2.188)$$

Defining spatial mesh sizes Δx and Δy in x -, y -direction and dividing the spectral space into elementary bins with a constant directional resolution $\Delta\theta$ and a constant relative frequency resolution $\Delta\sigma/\sigma$ (resulting in a logarithmic frequency distribution), we can denote the grid counters as

$$1 \leq i \leq N_x \quad (2.189)$$

$$1 \leq j \leq N_y \quad (2.190)$$

$$1 \leq l \leq N_\sigma \quad (2.191)$$

$$1 \leq m \leq N_\theta \quad (2.192)$$

in which N_x, N_y, N_σ and N_θ represents the number of grid points in x, y, σ and θ domain respectively. Doing so all variables will be located at points (i, j, l, m) .

Time discretization takes place with the implicit Euler method, which results in the following approximation of (2.188):

$$\begin{aligned}
\frac{N^n - N^{n-1}}{\Delta t} \Big|_{i,j,l,m} &+ \frac{[c_x N]_{i+1/2} - [c_x N]_{i-1/2}}{\Delta x} \Big|_{j,l,m}^n + \\
&\frac{[c_y N]_{j+1/2} - [c_y N]_{j-1/2}}{\Delta y} \Big|_{i,l,m}^n + \\
&\frac{[c_\sigma N]_{l+1/2} - [c_\sigma N]_{l-1/2}}{\Delta \sigma} \Big|_{i,j,m}^n + \\
&\frac{[c_\theta N]_{m+1/2} - [c_\theta N]_{m-1/2}}{\Delta \theta} \Big|_{i,j,l}^n, \quad (2.193)
\end{aligned}$$

where n is a time-level with Δt as time step. Note that locations in between consecutive counters are reflected with the half-indices.

Discretization in Space

The x - y space is discretized by a curvi-linear spatial grid in a spherical coordinate system, so that all geographic locations are located on a spherical Earth and defined by geographic longitude (x) and latitude (y).

A first order upwind scheme is employed to discretize the space so that the fluxes $c_x N$ at $(i + 1/2, j, l, m)$, $(i - 1/2, j, l, m)$ and $c_y N$ at $(i, j + 1/2, l, m)$, $(i, j - 1/2, l, m)$ are approximated in the following way:

$$c_x N \Big|_{i+1/2,j,l,m} = \begin{cases} c_x N \Big|_{i,j,l,m}, & c_x \Big|_{i,j,l,m} > 0 \\ c_x N \Big|_{i+1,j,l,m}, & c_x \Big|_{i+1,j,l,m} < 0 \end{cases} \quad (2.194)$$

$$c_x N \Big|_{i-1/2,j,l,m} = \begin{cases} c_x N \Big|_{i-1,j,l,m}, & c_x \Big|_{i-1,j,l,m} > 0 \\ c_x N \Big|_{i,j,l,m}, & c_x \Big|_{i,j,l,m} < 0 \end{cases} \quad (2.195)$$

and

$$c_y N \Big|_{i,j+1/2,l,m} = \begin{cases} c_y N \Big|_{i,j,l,m}, & c_y \Big|_{i,j,l,m} > 0 \\ c_y N \Big|_{i,j+1,l,m}, & c_y \Big|_{i,j+1,l,m} < 0 \end{cases} \quad (2.196)$$

$$c_y N \Big|_{i,j-1/2,l,m} = \begin{cases} c_y N \Big|_{i,j-1,l,m}, & c_y \Big|_{i,j-1,l,m} > 0 \\ c_y N \Big|_{i,j,l,m}, & c_y \Big|_{i,j,l,m} < 0 \end{cases} \quad (2.197)$$

Note that the combination of the time and space discretizations in (2.193), (2.194, 2.195) and (2.196, 2.197) results in

$$\begin{aligned}
\frac{N^n - N^{n-1}}{\Delta t} \Big|_{i,j,l,m} &+ \frac{[c_x N]_i - [c_x N]_{i-1}}{\Delta x} \Big|_{j,l,m}^n + \\
&\frac{[c_y N]_j - [c_y N]_{j-1}}{\Delta y} \Big|_{i,l,m}^n +
\end{aligned}$$

and it is also known as the first order, backward space, backward time (BSBT) scheme.

Discretization in Spectral Space

Frequency σ -space is defined by the user specifying the *lowest* frequency and the *highest* frequency of the domain: the number of frequencies will be computed by SWAN such that $\Delta f = 0.1f$. In directional θ -space the directional range is the full 360° .

To discretize the spectral space a hybrid central/upwind scheme is employed so that the fluxes $c_\sigma N$ at $(i, j, l + 1/2, m)$ and $c_\theta N$ at $(i, j, l, m + 1/2)$ are approximated in the following way:

$$c_\sigma N|_{i,j,l+1/2,m} = \begin{cases} (1 - 0.5\mu)c_\sigma N|_{i,j,l,m} + 0.5\mu c_\sigma N|_{i,j,l+1,m}, & c_\sigma|_{i,j,l,m} > 0 \\ (1 - 0.5\mu)c_\sigma N|_{i,j,l+1,m} + 0.5\mu c_\sigma N|_{i,j,l,m}, & c_\sigma|_{i,j,l+1,m} < 0 \end{cases} \quad (2.198)$$

and

$$c_\theta N|_{i,j,l,m+1/2} = \begin{cases} (1 - 0.5\nu)c_\theta N|_{i,j,l,m} + 0.5\nu c_\theta N|_{i,j,l,m+1}, & c_\theta|_{i,j,l,m} > 0 \\ (1 - 0.5\nu)c_\theta N|_{i,j,l,m+1} + 0.5\nu c_\theta N|_{i,j,l,m}, & c_\theta|_{i,j,l,m+1} < 0 \end{cases}, \quad (2.199)$$

where the parameters μ and ν have to be chosen. The fluxes at $(i, j, l - 1/2, m)$ and $(i, j, l, m - 1/2)$ are obtained from (2.198) and (2.199), respectively, by decreasing the indices by 1 in appropriate manner.

For all values $\mu \in [0, 1]$ and $\nu \in [0, 1]$, a blended form arises between first order upwind differencing ($\mu = \nu = 0$) and central differencing ($\mu = \nu = 1$).

Users can chose the values for ν and μ setting the *numerical data parameter* `[cdd]` and `[css]` respectively (see 'Input Parameters of the model' ?? paragraph at 'Numeric' level):

a value of `[cdd], [css]=0` corresponds to a central scheme and has the largest accuracy (diffusion ≈ 0) but the computation may more easily generate spurious fluctuations. A value of `[cdd], [css]=1`. corresponds to a first order upwind scheme and it is more diffusive and therefore preferable if (strong) gradients in depth or current are present.

Initial and Boundary Conditions

The initial spectra are computed (also for grid points located at boundaries) from the local wind velocities, using the deep-water growth curve of Kahma and Calkoen [54], cut off at values of significant wave height and peak frequency from Pierson and Moskowitz [78]. The average (over the model area) spatial step size is used as fetch with local wind. The shape of the spectrum is default JONSWAP with a \cos^2 -directional distribution.

Chapter 3

Wave Model Experiments and Results

Several numerical experiments are presented in this chapter, that is organized as follows:

- In Section 3.1, experiments have been done to check the model experiments solution sensitivity
 - to the input *Forcing Fields*;
 - to different *Numerical model Parameters*;
 - and, finally, to different *Physical processes* parameterizations.

The experiment results have been validated by using the *Significant Wave Height* and the *Peak Period* measured by the ISPRA directional buoys located at Venezia, Ancona and Monopoli.

- In Section 3.2 *SURF Relocatable Model* is introduced and the coupling experiments with SWAN Model are presented.
- Section 3.3 describes the numerical tests performed for the calculation of the *Stokes' Drift* fields that are then used with the *MEDSLIK-II* oil-spill model to check the resulting particle trajectories.

3.1 Sensitivity Experiments

For all the sensitivity experiments, the *Adriatic Sea* has been chosen to be the case study area. The Adriatic is about 750 km long and 200 km wide, with a limited opening at its southern connection to the Mediterranean Sea. The basin is shallow in its northern part while South of Ancona the depth increases down to 1200 m. The sea is surrounded by mountains, both on the Italian and on the Balkan side, where we find the Apennines and the Dinaric Alps respectively [8].

3.1.1 Model Setup

The Spatial domain has been discretized using a rectangular regular grid (see figure 3.1) with the vertexes located at

$$A = 12.20^{\circ} E, 39.00^{\circ} N$$

$$B = 20.78^{\circ} E, 39.00^{\circ} N$$

$$C = 20.78^{\circ} E, 45.82^{\circ} N$$

$$D = 12.20^{\circ} E, 45.82^{\circ} N$$

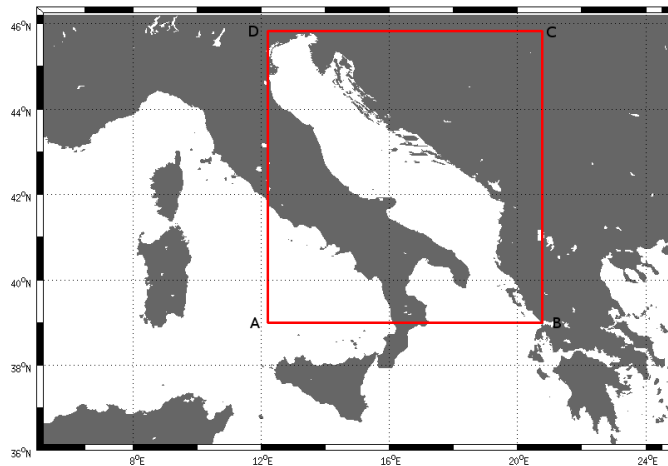


Fig. 3.1: Geometry of the entire computational domain

The *Spatial Computational Grid* uses a *Spherical Curvilinear* coordinate systems with constant *horizontal resolution* equal to 0.03° for the longitude and

0.022° for the latitude, resulting in a 287×311 grid points.

The *Frequency* domain is discretized with 35 bins starting from a minimum frequency of 0.04 s^{-1} by to a 1.5 s^{-1} maximum frequency. The *Directional* grid domain cover the full 360° with a resolution of 10° .

A summary of all the features of the computational domain (both *Spatial* than *Spectral*) of the SWAN model implementation in the Adriatic Sea is given in table 3.1.

Table 3.1: Features of the Spatial and Spectral computational domains used in the sensitivity SWAN Model tests

Grid Type	Min. Value	Max. Value	Number of Grid Points
Spatial Grid	12.20° E, 39.00° N	12.20° E, 45.82° N	287×311
Frequency Grid	0.04 s^{-1}	1.5 s^{-1}	35
Directional Grid	0°	360°	36

The *bathymetry* (see figure 3.2) is extracted from the *Adriatic Forecasting Systems* (hereafter called AFS). It is a *high-resolution* model implemented in the Adriatic sea [74]. The AFS horizontal grid resolution is equal to the SWAN *Spatial Grid* and the vertical grid is composed of 31 vertical sigma levels. AFS produces simulations and forecasts provided as daily and hourly mean outputs [36].

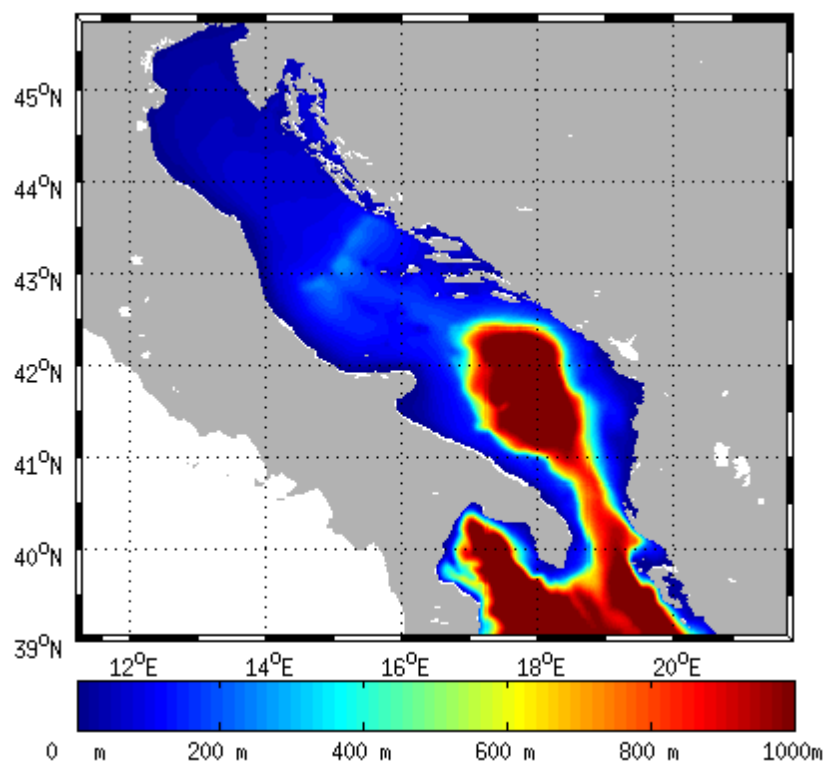


Fig. 3.2: Bathymetry of the entire computational domain with a horizontal grid resolution of $1/45^\circ$ (approximately 2.2 km)

All the computations have been performed in *Non-Stationary* mode, which means that the equation 2.127 is solved by the numerical model. The time integration technique chosen is the *implicit Euler* method described in Section 2.3.4.

The simulated period is between 14-05-2013 at 00.00 and 22-05-2013 at 00.00.

The coordinates and the locations of the ISPRA directional buoys used for the results validation are shown in figure 3.3. The directional buoys data have been made available as part of the exchange activities set forth by the *scientific collaboration ISPRA-INGV Agreement*.

Location	Longitude	Latitude
Venezia	12.516700° E	45.333500° N
Ancona	13.719400° E	43.825000° N
Monopoli	17.377800° E	40.975000° N

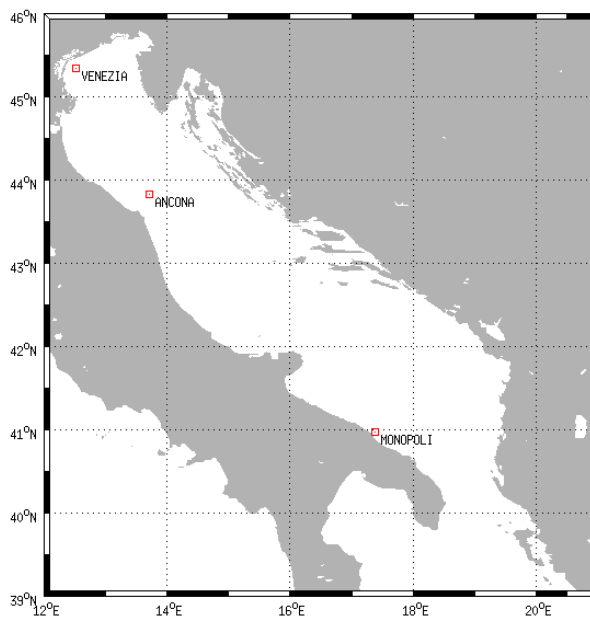


Fig. 3.3: Spatial location of the three ISPRA buoys used to validate sensitivity numerical experiments

Wind input data used to force the wind-wave model are:

- 1) forecast and analysis data with a spatial resolution of $1/4^\circ$ and temporal resolution of 6 hours produced by the European Centre for Medium-range Weather Forecasts (hereafter called ECMWF) and provided by INGV.
- 2) analysis data from the COSMO-ME model implemented by the Italian National Center of Meteorology and Climatology (CNMCA) over the European area with a 7 km grid resolution and a 3 hours temporal resolution and made available as part of the exchange activities sanctioned by the agreement SGV-INGV for COSMO.

The word ‘*forecast*’ means that the atmospheric fields are produced by integrating the atmospheric model equations in the future while the word ‘*analysis*’ indicates atmospheric fields produced by combining short-range forecast data with observations to produce the best fit to both.

Currents input data from AFS are provided with a temporal resolution of 1 hour on an Arakawa C-grid [71]. In this kind of grid, scalar quantities (T , S , p , ρ) are defined at the center of each tridimensional cell, while vector ones (u , v , w) are defined in the centre of each face of the cells (see figure 3.4).

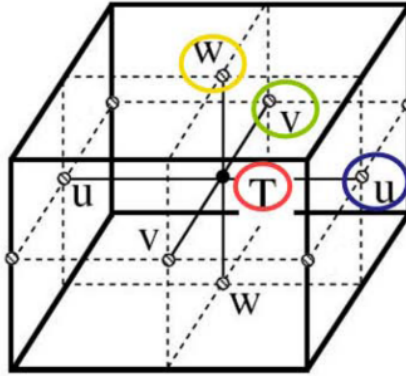


Fig. 3.4: Arakawa C-Grid definition

For simplicity, hereafter the three-dimensional grid identified by the points in which AFS scalar quantities are defined will be called AFS *Scalar Grid* or *T-grid*. Similarly, the two three-dimensional grids identified by points where AFS zonal and meridional quantities are defined (i.e., u and v) will be called, respectively, AFS *Zonal* and *Meridional* grid or *U-grid* and *V-grid*.

The SWAN model requires current fields defined at the AFS scalar grid points. Thus an interpolation is required to bring (U , V) current velocities

components in the T -spatial grid.

The *Interpolation Techniques* which can be used are the *Linear* and the *Bilinear* methods, considering that, in this case, the last one reduces to the first one.

The wind velocity grid is very different in resolution from the SWAN one. Consider, for example, figure 3.5. It represents an ECMWF analysis zonal wind velocity field, nine grid points of the SWAN *Spatial Computational Grid* (in blue) and nine points of the ECMWF grid (in black).

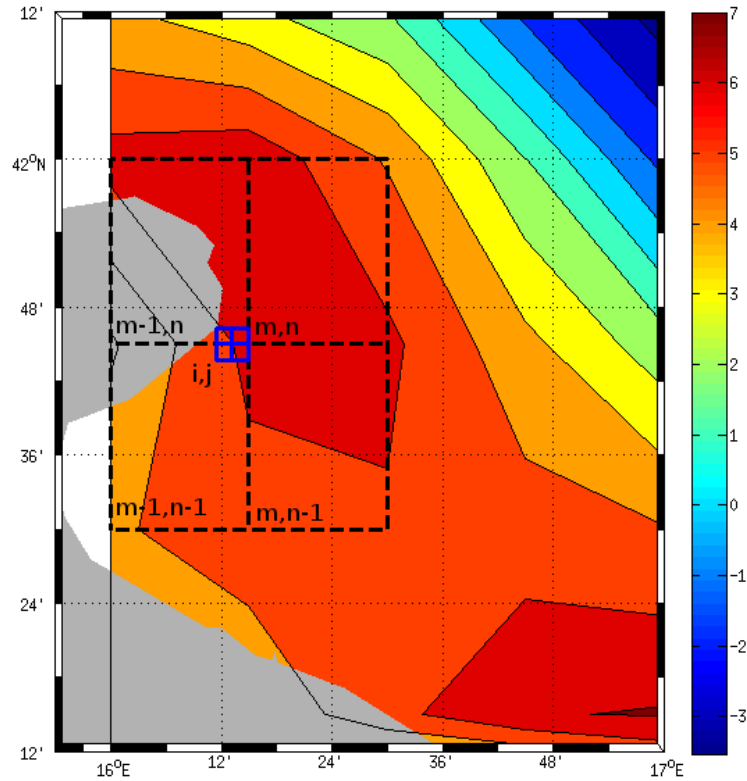


Fig. 3.5: ECMWF zonal wind velocity field, nine grid points of the SWAN grid (in blue) and nine points of the ECMWF grid (in black).

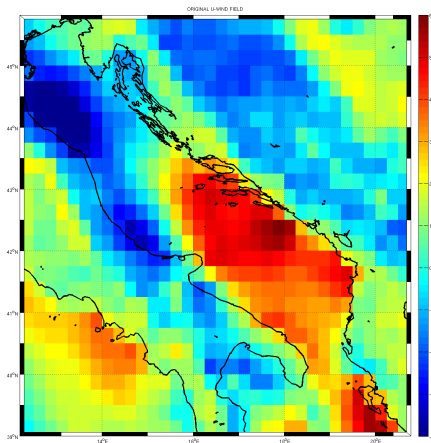
In order to find a zonal wind velocity value in the vertex (i, j) of the SWAN grid, it is needed to interpolate on it the data defined in vertexes (m, n) , $(m - 1, n)$, $(m, n - 1)$ and $(m - 1, n - 1)$ of the ECMWF grid. In this case only the *Bilinear* technique can be used.

Therefore, to interpolate the original wind and current forcing fields on SWAN spatial grid a *Bilinear* method has been chosen.

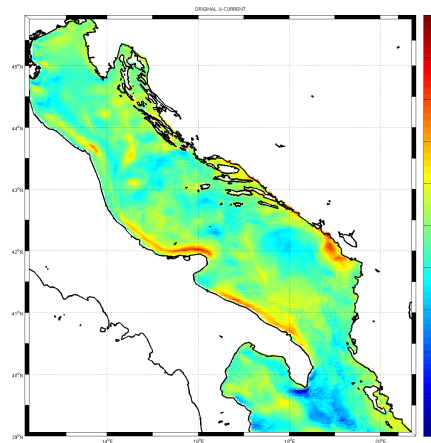
Current fields are defined only for sea locations while wind fields are defined both on the land and on the sea.

On the other hand, a regular computational domain generally comprehends sea and land locations, the so called *wet* and *dry* grid points, respectively. Therefore, when current fields are interpolated, it can happen that one or more grid points of the original field are located on the land. On these points there are no numerical current velocities values associated, and interpolation becomes asymmetric that changes the properties of the method. We need to consider that winds exists also on the land but they can not be used to interpolate data on the sea, due to the fact that these two environments present a different roughness and orography.

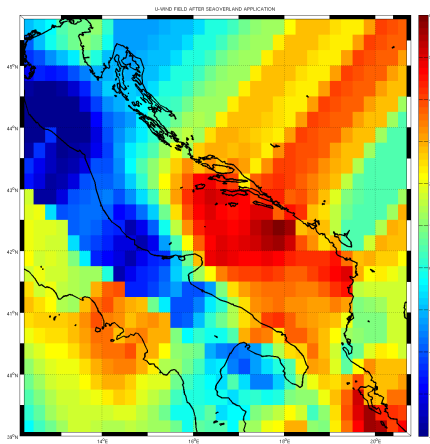
Therefore, all input fields have been processed with the *SeaOverLand* procedure that extrapolates average sea values on land points (figure 3.6) before the bilinear interpolation is used.



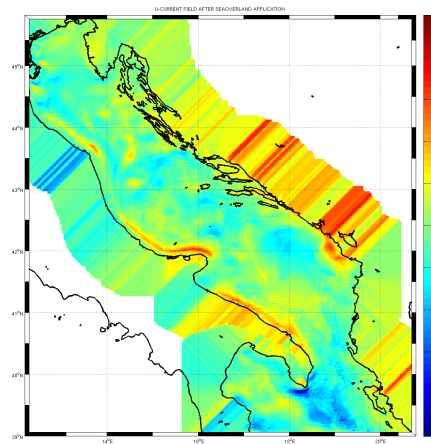
(a)



(b)



(c)



(d)

Fig. 3.6: Original ECMWF analysis wind and AFS 1 hour current fields (respectively (a) and (b)) and the same fields after SeaOverLand algorithm application (respectively (c) for the wind and (d) for the current).

After the *SeaOverLand* application, the original wind and current forcing fields have been bi-linearly interpolated using two algorithms: the first is that one used by the SWAN model, the second is that one used by the NEMO model [66].

The differences between forcing fields interpolated with both algorithms are shown in figures 3.7, 3.8 and 3.9.

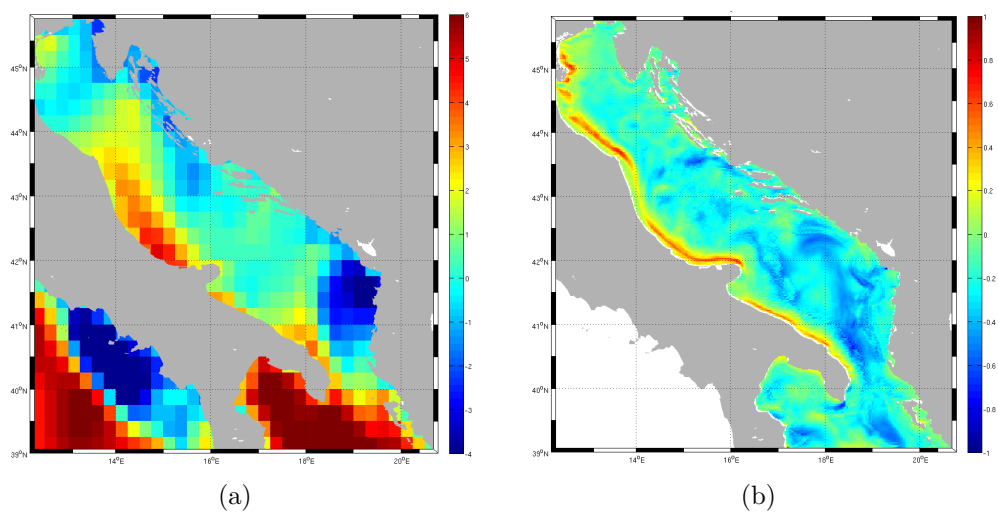


Fig. 3.7: Original ECMWF analysis wind and AFS 1 hour current fields (respectively (a) and (b)).

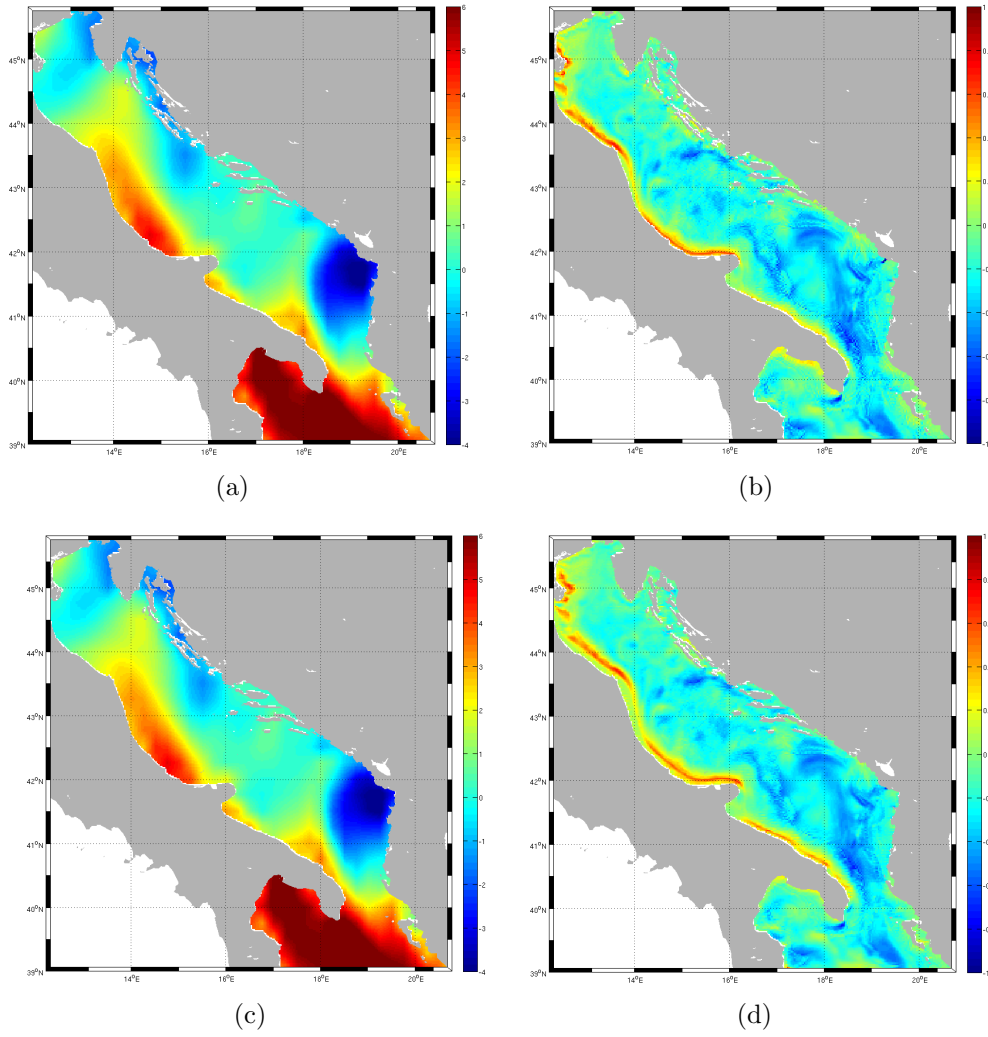


Fig. 3.8: ECMWF analysis wind and AFS 1 hour current fields interpolated using SWAN (respectively (a) and (b)) and using NEMO tool (respectively (c) for wind and (d) for current).

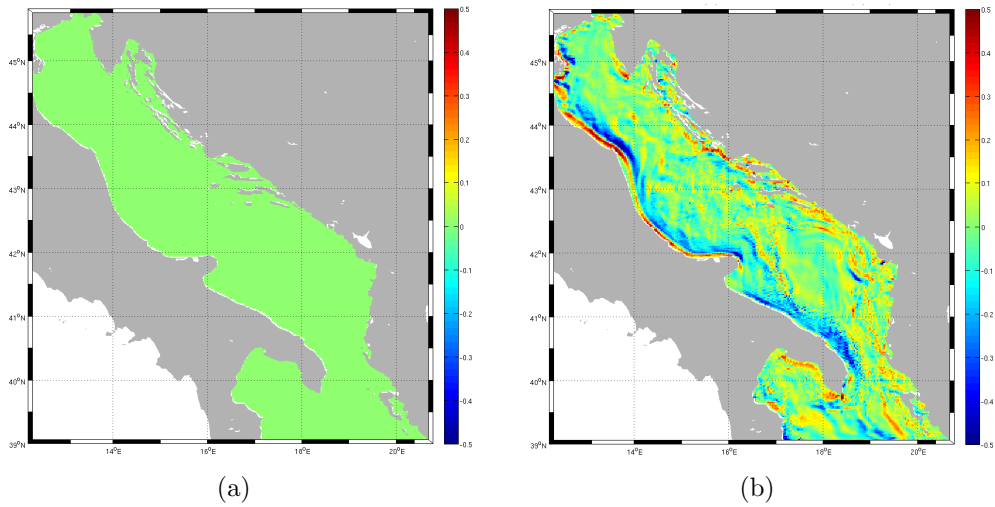


Fig. 3.9: Difference between ECMWF analysis wind and AFS 1 hour current fields (respectively (a) and (b)) interpolated by NEMO tool and by SWAN model.

The results demonstrate that for the wind input fields the two kind of bi-linear interpolation algorithms are equivalent, while for current input fields there are remarkable differences.

This is probably due to the fact that the SWAN model applies the land mask on the current fields before that the bi-linear interpolation is performed, vanishing the *SeaOverland* procedure.

Therefore, since the aim of this group of experiments was to test the original SWAN model code, it has been chosen to use the NEMO bi-linear interpolation algorithm to interpolate all the different forcing input fields on the SWAN spatial computational grid.

The linear interpolation in time is performed by SWAN.

The default settings parameters used in sensitivity experiments is summarized in table 3.2.

Table 3.2: Default settings parameters used in numerical parameters sensitivity experiments.

Parameter	Default configuration
General Parameters	
Gravitational Acceleration	$9.81ms^{-2}$
Water Density	$1025 kgm^{-3}$
Wind Drag Coefficient	no cutting off the drag coefficient
Spectral Output	based on variance spectrum
Convection for wind and wave direction adopted	nautical
Shape of spectral tail above [<i>fhigh</i>]	automatic
Maximum Froude number	0.8
Computational Parameters	
Time mode	Non-Stationary
Spatial mode	Two-Dimensional
Start time of the simulation	14.05.2013 at 00.00
End Time of the simulation	22.05.2013 at 00.00
Geographical-Space Grid	
Coordinates	spherical
Computational grid	curvi-linear grid
Number of meshes in lon-direction	287
Number of meshes in lat-direction	311
Spectral-Space Grid	
Spectral direction grid	cover the full circle
Number of meshes in θ space	36
Lowest discrete freq. used in calculation	$0.04 Hz$
Highest discrete freq. used in calculation	$1.5 Hz$
Number of meshes in <i>frequency</i> space	35
Forcing Input Data	
Wind forcing data	<i>ECMWF</i> forecast
Current forcing data	<i>AFS 1 hour</i>
Numerics	
Numerical scheme	BSBT
Max number of iterations per time step	100

Table 3.2: Default settings parameters used in numerical sensitivity experiments.

Parameter	Default configuration
Initial and Boundary Conditions	
First time step of the computation	Initial wave-field computed from local wind velocities
Each next restart	Initial wave-field read from hotstart file
Physical Processes: Source and Sinks	
Linear wave growth by wind input	<i>Cavaleri-Malanotte</i> formulation with $[AGROW] = 0.015$, where $[AGROW]$ is the prop. coefficient for linear wave growth term
Exponential wave growth by wind input	<i>Komen</i> formulation with $[cds2] = 2.36e - 5$, $[stpm] = 3.02e - 3$ where $[cds2]$ is the coeff. for the rate of whitecapping dissipation and $[stpm]$ is the value of the wave steepness for a Pierson-Moskowitz spectrum
Quadruplet	fully explicit computation of the non linear transfer with DIA algorithm ($[iquad] = 2$)
Friction	JONSWAP bottom friction dissipation
Wave Breaking	constant breaker parameter with $[\alpha] = 1$ and $[\gamma] = 0.73$, where $[\alpha]$ is prop. coefficient of the rate of dissipation and $[\gamma]$ is the ratio of maximum individual wave height over depth

Table 3.2: Default settings parameters used in numerical sensitivity experiments.

3.1.2 Sensitivity Experiments to Numerical Parameters

The aim of these experiments is to investigate the SWAN model sensitivity to some of the numerical parameters listed in table 3.2. In particular, we examined the computational *time-step* and the *c-theta* parameter.

The *c-theta* parameter is a numerical restriction on the time step which should be imposed in large-scale SWAN application in order to prevent inaccurate wave refraction due to large spatial bottom gradient. Specifically, the Courant number based on ΔT and $\Delta\theta$ (i.e., time-step and directional bin, respectively) should not exceed unity, that is,

$$Cr \equiv \frac{|c_\theta|\Delta T}{\Delta\theta} \leq \alpha_\theta \leq 1 \quad (3.1)$$

where α_θ is a user-defined maximum Courant number.

It has to be remarked that equation 3.1 is not required for the stability of the integration method, but contributes to improve its physical accuracy.

In order to investigate the SWAN model sensitivity to these parameters, four different numerical tests have been done. First, three experiments has been performed changing only the *time-step* and not considering the *c-theta* parameter. Then, a test with the numerical restriction for refraction *c-theta* and the with the time-step that showed the best results in the previous experiments.

The other model parameters have been set on their *Default* configurations, which are summarized in table 3.2.

The configurations of the four numerical experiments performed are described in table 3.3.

Results are shown in figures 3.10 and 3.11: in picture 3.10, the time series of the *Significant Height* computed by the SWAN model at each ISPRA buoy location for all the four experiments is compared with the time series of the *Significant Height* sampled by each ISPRA buoy. In figure 3.11, the *Peak Period* measured at each ISPRA buoy is compared to the modeled one.

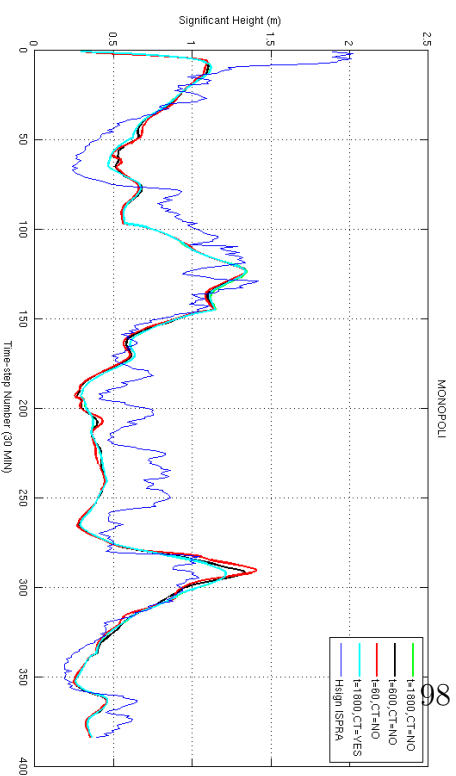
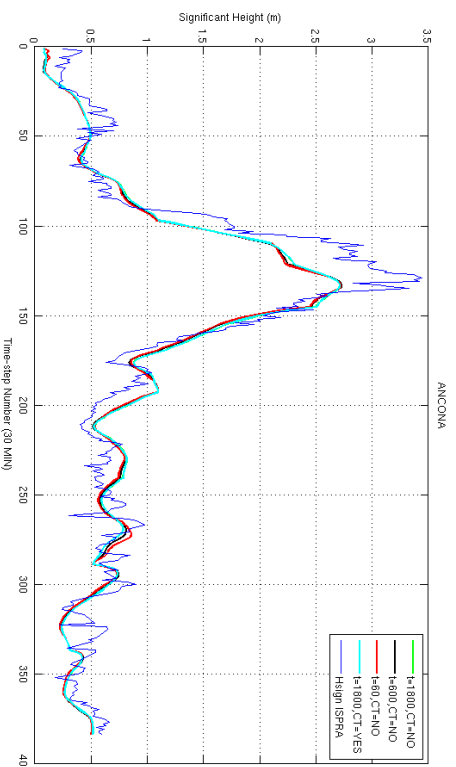
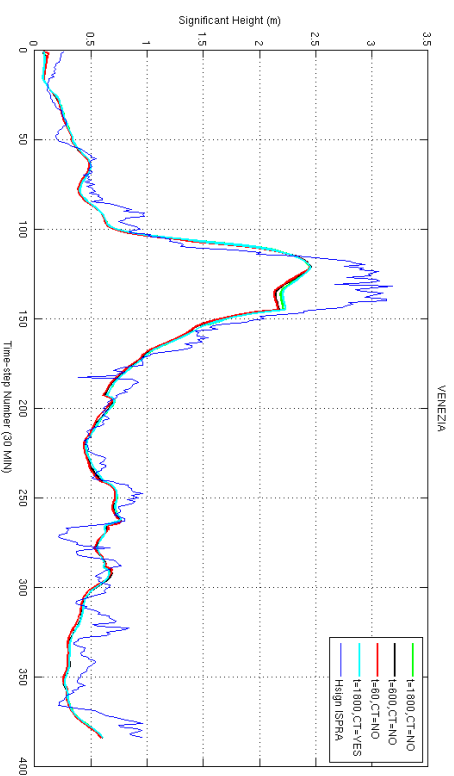
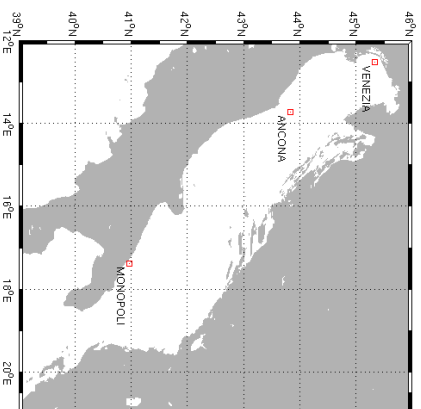


Fig. 3.10: Time series of the *Significant Height* computed by the SWAN model at each ISPRA buoy location for all the four experiments performed to test the SWAN sensitivity to time-step variations and the $c - theta$ parameter usage. The simulations start on the 14.05.2013 at 00.00 and end on the 22.05.2013 at 00.00.

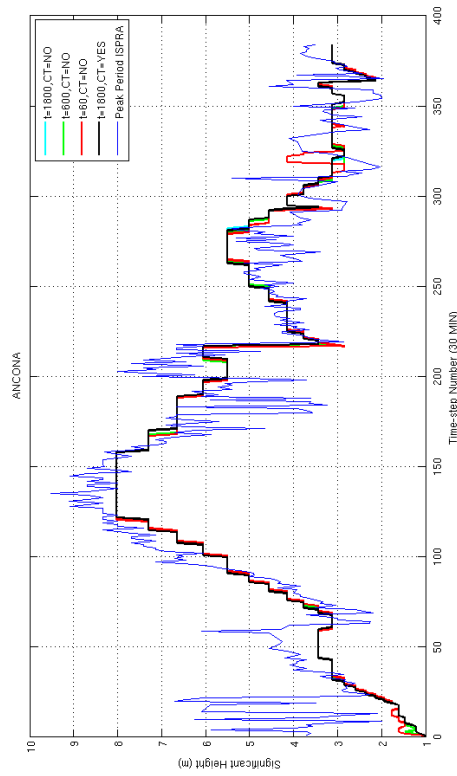
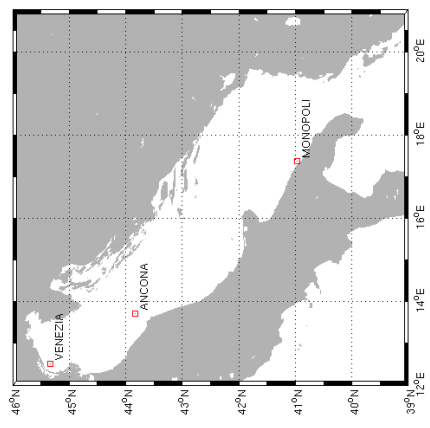
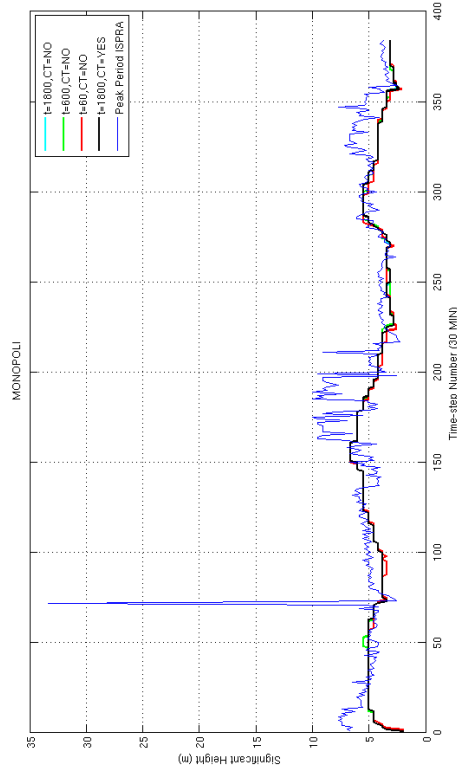
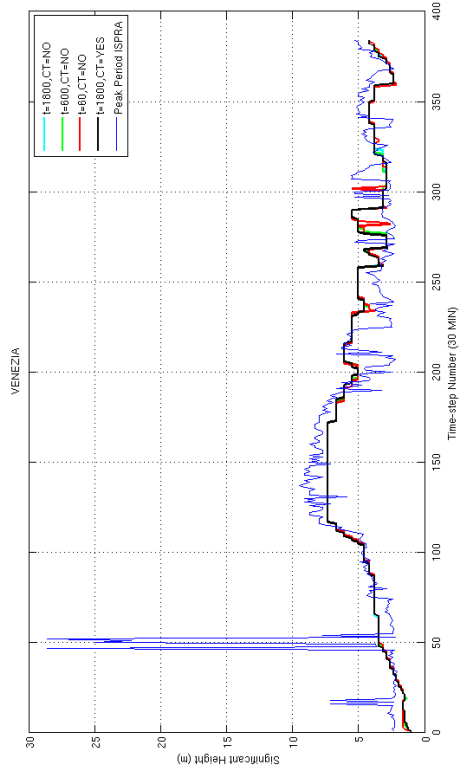


Fig. 3.11: Time series of the *Peak Period* computed by the SWAN model at each ISPRAs buoy location for all the four experiments performed to test the SWAN sensitivity to time-step variations and the $c - theta$ parameter usage. The simulations start on the 14.05.2013 at 00.00 and end on the 22.05.2013 at 00.00.

Table 3.3: Description of the four numerical experiments performed to test SWAN sensitivity to *time-step* and *c-theta* numerical parameters.

Experiment Number	Time-step	<i>c-theta</i>
Exp. 1.1	1800 s	NO
Exp. 1.2	600 s	NO
Exp. 1.3	60 s	NO
Exp. 1.4	1800 s	YES [<i>ctheta</i>] = 0.5

In order to objectively quantify the accuracy of the numerical model simulations, the following statistical parameters have been calculated for each time series:

- The *Root Mean Square Error* x_{rmse} , which describes the magnitude of a varying quantity and is defined as

$$x_{rmse} = \sqrt{\frac{\sum_{i=1}^N (x_i^{SWAN} - x_i^{BUOY})^2}{N}} \quad (3.2)$$

where x_i^{SWAN} and x_i^{BUOY} are the values of the parameter x respectively calculated by the Wind-Wave model and sampled by the buoy at the i^{th} index time of the time series. It is a frequently used measure of the differences between values predicted by a model or an estimator and the values actually observed.

- The *Bias*, which shows the tendency of a data set (a model output in this case) to a specific behavior. It is defined as

$$Bias = \frac{\sum_{i=1}^N (x_i^{SWAN} - x_i^{BUOY})}{N} \quad (3.3)$$

A large bias value means that the model has a tendency to consistently forecast on a specific way (under- or overforecast), whereas a small bias indicates of a more random or dispersive behavior.

- The *Correlation Coefficient* which is defined as

$$R = \frac{COV(SWAN, BUOY)}{\sqrt{VAR(SWAN)VAR(BUOY)}} \quad (3.4)$$

where $COV(SWAN, BUOY)$ is the *covariance* matrix of the model and the samples and $VAR(SWAN)$ and $VAR(BUOY)$ are the variances of, respectively, the model and the buoy data. R is between zero and one: data with high correlation show values of R more close to one.

In tables 3.4 and 3.5 the values of these statistical indexes are shown for each buoy location, both for *Peak Periods* and *Significant Heights*.

Table 3.4: Statistical indexes calculated for the *Significant Height*.

Statistical Index	Exp 1.1	Exp 1.2	Exp 1.3	Exp 1.4
VENEZIA				
Mean BUOY	0.82	0.82	0.82	0.82
Mean SWAN	0.72	0.71	0.70	0.72
Bias	0.10	0.11	0.12	0.10
rmse	0.24	0.25	0.26	0.24
R	0.96	0.96	0.96	0.96
ANCONA				
Mean BUOY	0.96	0.96	0.96	0.96
Mean SWAN	0.90	0.88	0.89	0.90
Bias	0.06	0.08	0.08	0.06
rmse	0.25	0.25	0.26	0.25
R	0.96	0.96	0.96	0.96
MONOPOLI				
Mean BUOY	0.72	0.72	0.72	0.72
Mean SWAN	0.64	0.63	0.63	0.64
Bias	0.08	0.08	0.09	0.08
rmse	0.26	0.26	0.27	0.26
R	0.71	0.70	0.69	0.71

Table 3.5: Statistical indexes calculated for the *Peak Period*.

Statistical Index	Exp 1.1	Exp 1.2	Exp 1.3	Exp 1.4
VENEZIA				
Mean BUOY	4.74	4.74	4.74	4.74
Mean SWAN	4.50	4.46	4.45	4.50
Bias	0.24	0.28	0.29	0.24
rmse	2.72	2.72	2.72	2.72
R	0.46	0.47	0.47	0.46
ANCONA				
Mean BUOY	4.98	4.98	4.98	4.98
Mean SWAN	4.80	4.77	4.76	4.80
Bias	0.17	0.21	0.22	0.18
rmse	1.16	1.16	1.16	1.16
R	0.82	0.82	0.82	0.82
MONOPOLI				
Mean BUOY	5.21	5.21	5.21	5.21
Mean SWAN	4.40	4.39	4.35	4.40
Bias	0.80	0.82	0.86	0.80
rmse	2.12	2.14	2.16	2.13
R	0.36	0.35	0.35	0.36

Data listed in table 3.4 and 3.5 show that the SWAN numerical model seems to be quite *insensitive* to the computational time-step. This can be justified by the many parametrizations that are used to represent the physical processes involved in waves generation in the SWAN model code. Not using some kind of time evolving equations, reduces the sensitivity of the model results to time step variations.

In addition, it has to be noted that the SWAN *insensitivity* to time-step changes can be also due to the coarse spatial grid used, which can not be able to represent small scale gradient of quantities involved in waves generation reducing sensibly their changes in time.

Since the simulations results are insensitive to the time steps, for the last experiments (1.4) we decided to use the time step that requires less computational time (1800 seconds).

The test 1.4 shows also that the *c-theta* parameter does not increase the accuracy of the simulation. Thus, the computational grid used is resolved enough to properly represent the wave refraction, but too coarse to properly represent processes involved in wave growth.

3.1.3 Sensitivity Experiments to the Input Fields (Wind and Currents)

In this section, the experiments done to test the SWAN sensitivity to different input wind fields with and without coupling with the AFS current fields are described.

Three atmospheric model outputs have been used: the ECMWF forecast and analysis and the COSMO-ME analysis. For the currents the AFS hourly current fields have been used.

In table 3.6 the configuration of the model parameters used in this group of experiments is described while table 3.7 overviews the sensitivity experiments to the input fields.

Table 3.6: Settings parameters used in forcing fields sensitivity experiments.

Parameter	Configuration
General Parameters	
	see 3.2
Computational Mode	
	see 3.2
Time - step	1800 s
<i>c-theta</i>	$[c - theta] = 0.5$
Geographical-Space Grid	
	see 3.2
Spectral-Space Grid	
	see 3.2
Numerics	
	see 3.2
Initial and Boundary Conditions	
	see 3.2
Physical Processes: Source and Sinks	
	see 3.2

Table 3.7: Description of the six numerical experiments performed to test SWAN sensitivity to *wind* and *current* forcing fields.

Experiment Number	WIND field	CURRENT field
Exp. 2.1	ECMWF fcst	NO
Exp. 2.2	ECMWF analysis	NO
Exp. 2.3	COSMO-ME analysis	NO
Exp. 2.4	ECMWF fcst	AFS 1 hr
Exp. 2.5	ECMWF analysis	AFS 1 hr
Exp. 2.6	COSMO-ME analysis	AFS 1 hr

Results are shown in figures 3.12 and 3.13. In picture 3.12, the time series of the *Significant Wave Height* computed in the six experiments at each ISPRA buoy location is shown, while in figure 3.13 the same is done for the *Wave Peak Period*.

In tables 3.8 and 3.9 the statistical indexes calculated from each experiment are shown for each buoy location, both for *Wave Peak Periods* and *Significant Wave Heights*.

Table 3.8: Statistical indexes calculated for the *Significant Wave Height* for the 8 days simulated.

Statistical Index	Exp 2.1	Exp 2.2	Exp 2.3	Exp 2.4	Exp 2.5	Exp 2.6
VENEZIA						
Mean BUOY	0.82	0.82	0.82	0.82	0.82	0.82
Mean SWAN	0.78	0.73	0.80	0.72	0.71	0.78
Bias	0.04	0.09	0.03	0.10	0.11	0.04
rmse	0.24	0.24	0.23	0.24	0.25	0.24
R	0.94	0.96	0.95	0.96	0.96	0.95
ANCONA						
Mean BUOY	0.96	0.96	0.96	0.96	0.96	0.96
Mean SWAN	0.90	0.91	1.00	0.90	0.90	1.00
Bias	0.06	0.05	-0.05	0.06	0.06	-0.04
rmse	0.23	0.23	0.26	0.25	0.25	0.24
R	0.97	0.97	0.96	0.96	0.96	0.96
MONOPOLI						
Mean BUOY	0.72	0.72	0.72	0.72	0.72	0.72
Mean SWAN	0.60	0.60	0.68	0.64	0.63	0.73
Bias	0.13	0.13	0.03	0.08	0.09	-0.00
rmse	0.27	0.27	0.24	0.26	0.26	0.26
R	0.72	0.71	0.77	0.71	0.70	0.74

Table 3.9: Statistical indexes calculated for the *Wave Peak Period* for the 8 days simulated.

Statistical Index	Exp 2.1	Exp 2.2	Exp 2.3	Exp 2.4	Exp 2.5	Exp 2.6
VENEZIA						
Mean BUOY	4.74	4.74	4.74	4.74	4.74	4.74
Mean SWAN	4.86	4.80	4.87	4.50	4.46	4.54
Bias	-0.13	-0.06	-0.13	0.24	0.28	0.20
rmse	2.78	2.77	2.75	2.72	2.69	2.69
R	0.44	0.44	0.46	0.46	0.48	0.48
ANCONA						
Mean BUOY	4.98	4.98	4.98	4.98	4.98	4.98
Mean SWAN	4.95	4.97	4.77	4.80	4.82	4.64
Bias	0.03	0.01	0.21	0.18	0.16	0.34
rmse	1.19	1.20	1.11	1.16	1.16	1.13
R	0.81	0.81	0.87	0.82	0.82	0.86
MONOPOLI						
Mean BUOY	5.21	5.21	5.21	5.21	5.21	5.21
Mean SWAN	4.18	4.17	4.60	4.40	4.39	4.66
Bias	1.02	1.04	0.61	0.80	0.82	0.54
rmse	2.27	2.28	2.18	2.13	2.13	2.17
R	0.32	0.31	0.28	0.36	0.37	0.27

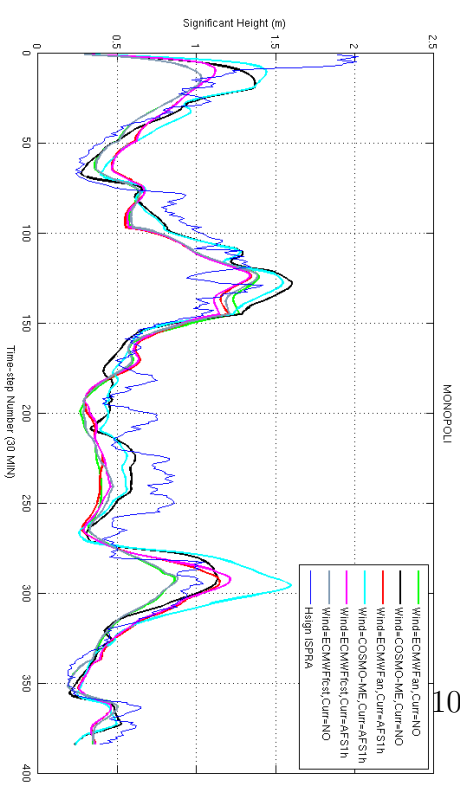
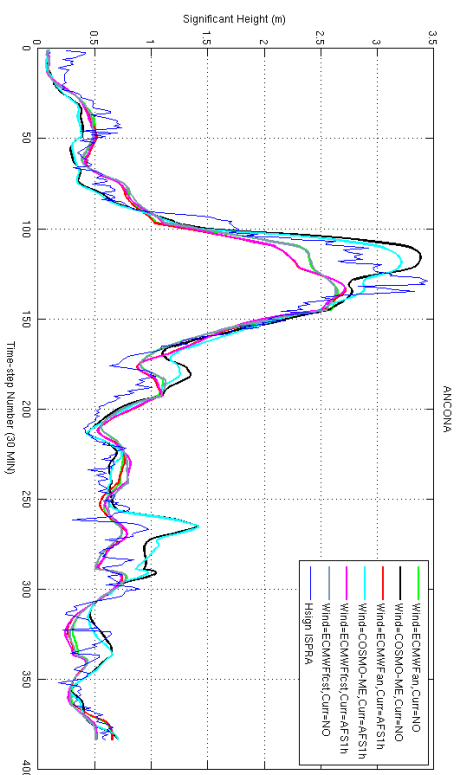
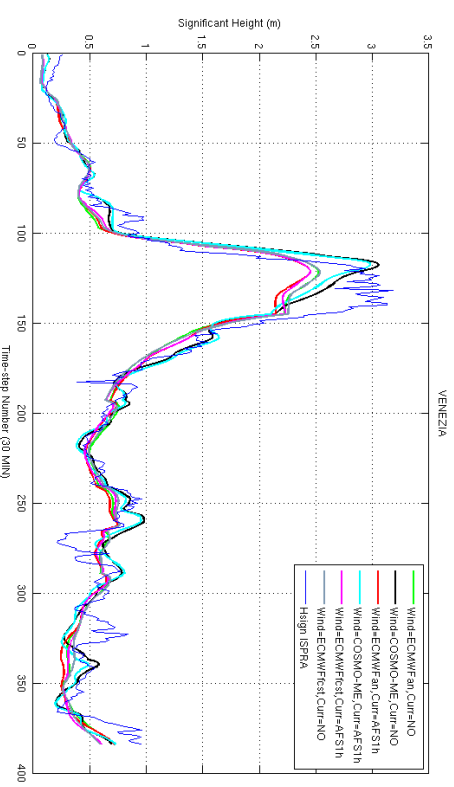
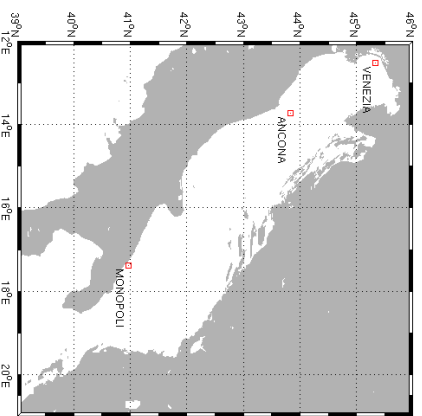


Fig. 3.12: Time series of the *Significant Wave Height* computed by the SWAN model at each ISPRa buoy location for the six experiments performed to test the SWAN sensitivity to input forcing fields. The simulations start on the 14.05.2013 at 00.00 and end on the 22.05.2013 at 00.00.

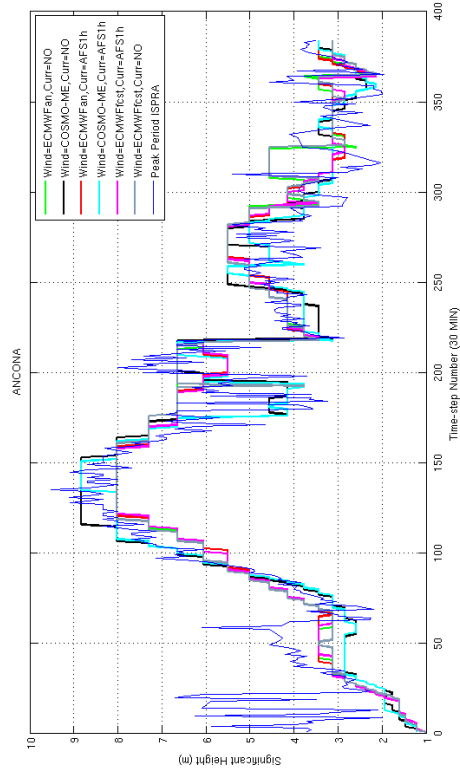
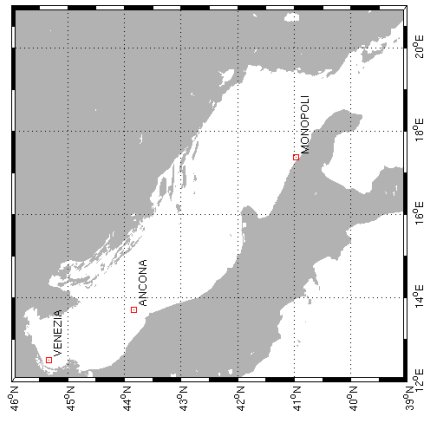
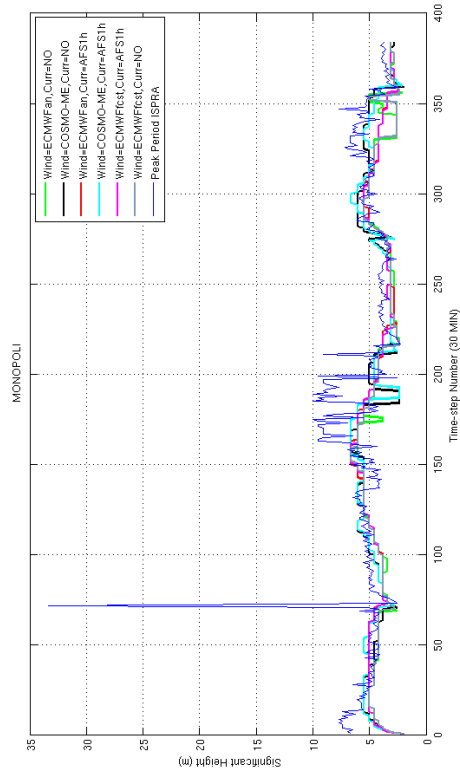
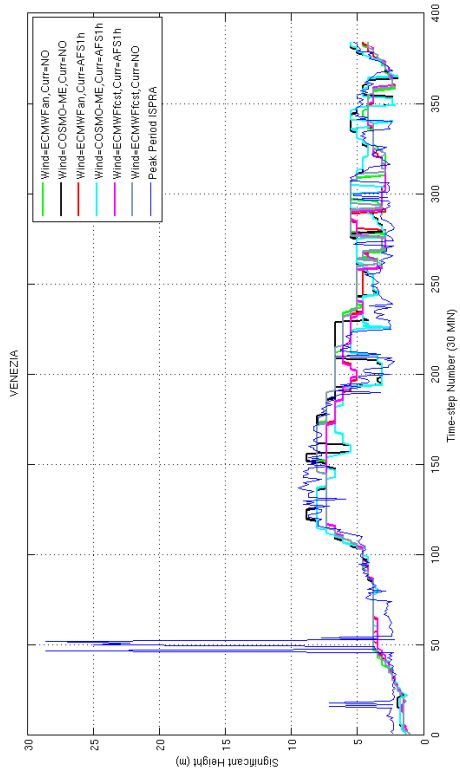


Fig. 3.13: Time series of the *Peak Period* computed by the SWAN model at each ISPPA buoy location for the six experiments performed to test the SWAN sensitivity to input forcing fields. The simulations start on the 14.05.2013 at 00.00 and end on the 22.05.2013 at 00.00.

The *rmse* and the *bias* listed in tables 3.8 and 3.9 and the time series plots 3.12 and 3.13 demonstrate that simulations performed using COSMO-ME wind fields forcing show the lowest errors. This is to be expected due to the higher temporal and spatial resolution of COSMO-ME fields.

Concerning to the ECMWF fields, the differences between simulations done using analysis or forecast fields are not so large because we used only the first day of forecast for each day.

Looking at *Venezia* and *Ancona* buoys results in figures 3.12 and 3.13 and tables 3.8 and 3.9, using current fields input forcing fields, the accuracy of the simulations seems to decrease, while for the *Monopoli* case it increases.

Therefore, the effect of the currents on the waves at Monopoli is larger than at the North Adriatic probably because they are in general more accurate.

3.1.4 Sensitivity Experiments to Wave Physical Processes

The real strength of third generation wave models is the possibility to choose which physical process involved in waves generation could be activated to simulate the wave conditions.

In order to calibrate the model, it is needed to test the different physical processes configurations to find the best physical setting capable to properly simulate the environmental dynamics characterizing a particular place.

In this section, the experiments performed to achieve this target are described.

The set of experiments is divided into three groups. In *the first*, all the different SWAN parametrizations able to simulate the *Exponential wave growth by wind* and the *White-Capping* (see paragraphs 2.3.3 and 2.3.3) processes are tested. In the *second group* SWAN parametrizations for *Bottom Friction* (see paragraph 2.3.3 for a detailed description of the parametrizations) are investigated. In *the third* one the *Non-Linear Triads* (see 2.3.3) are tested.

Exponential Wave Growth and White-Capping

In table 3.10 the parameters of the model configuration used in the first group of experiments are shown:

Table 3.10: Settings parameters used in Exponential Wind Growth and White-Capping sensitivity experiments.

Parameter	Default configuration
General Parameters	
	see 3.2
Computational Mode	
	see 3.6
Geographical-Space Grid	
	see 3.2
Spectral-Space Grid	
	see 3.2
Numerics	
	see 3.2
Initial and Boundary Conditions	

Parameter	Default configuration
	see 3.2
Forcing fields	
Wind	ECMWF analysis
Current	AFS 1 hr

In table 3.11 the list of experiments to test SWAN sensitivity to *Exponential wave growth by wind* and *White-Capping* physical processes is summarized.

Table 3.11: Description of the five numerical experiments performed to test SWAN sensitivity to *Exponential wave growth by wind* and *White-Capping* physical processes.

Experiment Number	EXPONENTIAL WAVE GROWTH	WHITE-CAPPING
Exp. 3.1	KOMEN	KOMEN
Exp. 3.2	JANSSEN	JANSSEN
Exp. 3.3	WESTH	WESTH
Exp. 3.4	JANSSEN	KOMEN
Exp. 3.5	WESTH	KOMEN

In figures 3.14 and 3.15 the results are shown for the comparison between the model *Significant Wave Height* and *Wave Peak Period* and the ISPRA time series.

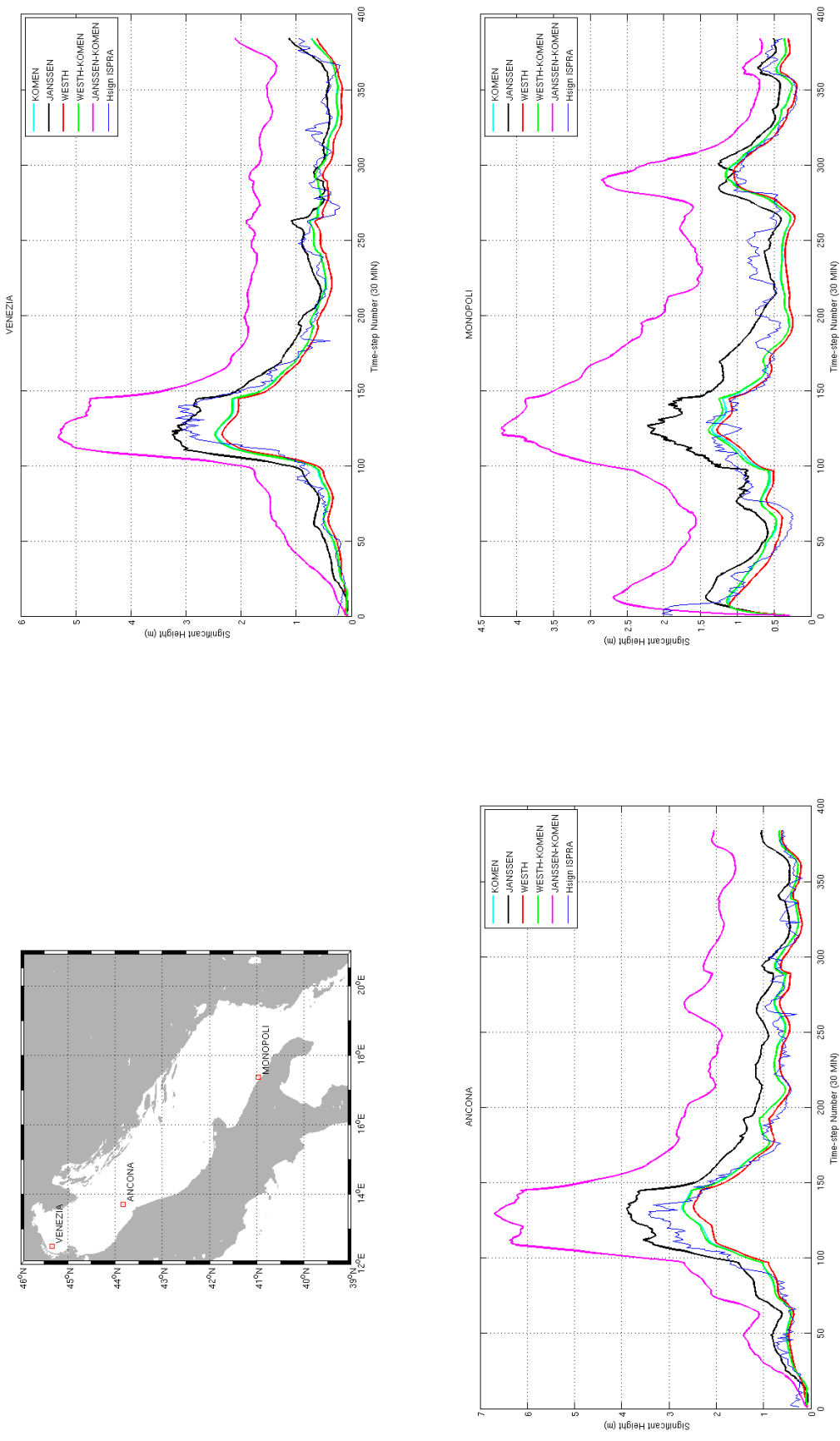


Fig. 3.14: Time series of the *Significant Wave Height* computed by the SWAN model at each ISFRA buoy location for the five experiments performed to test the SWAN sensitivity to *Exponential wave growth by wind* and *White-Capping* physical processes. The simulations start on the 14.05.2013 at 00.00 and end on the 22.05.2013 at 00.00.

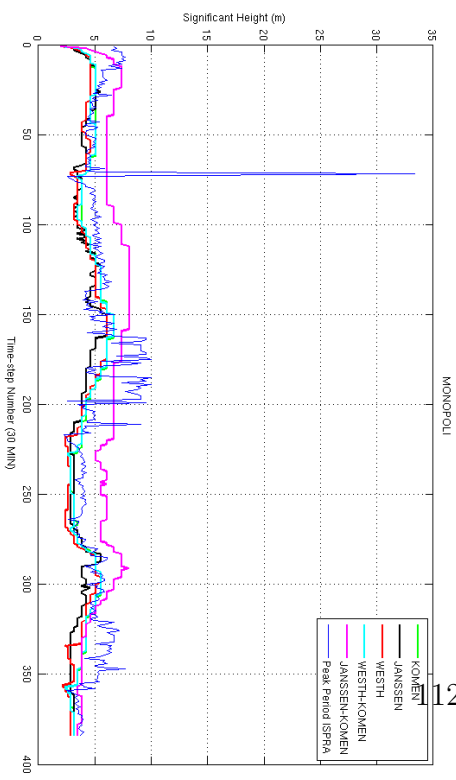
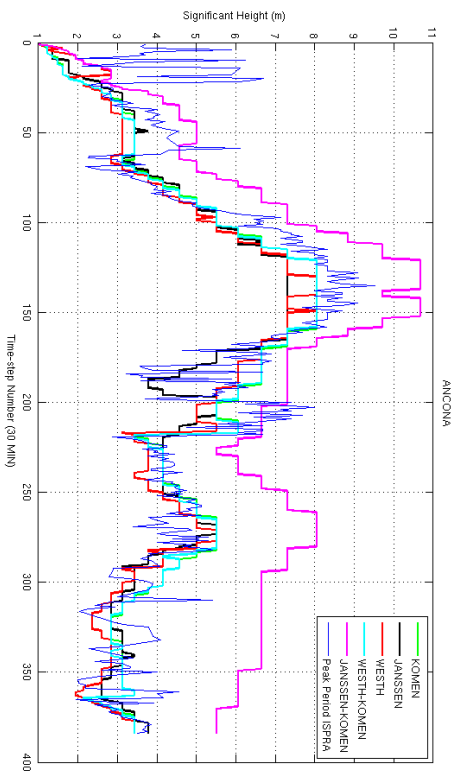
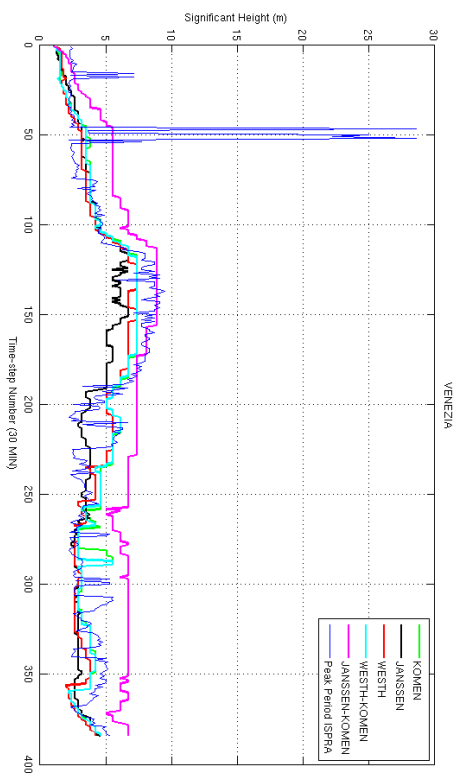
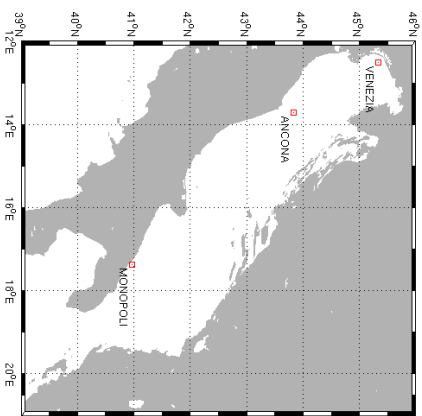


Fig. 3.15: Time series of the *Peak Period* computed by the SWAN model at each ISPPRA buoy location for the five experiments performed to test the SWAN sensitivity to *Exponential wave growth by wind* and *White-Capping* physical processes. The simulations start on the 14.05.2013 at 00.00 and end on the 22.05.2013 at 00.00.

In tables 3.12 and 3.13 the statistical indexes obtained from each model simulation are shown for each buoy location, both for *Wave Peak Periods* and *Significant Wave Heights*.

Table 3.12: Statistical indexes calculated for the *Significant Height*.

Statistical Index	Exp 3.1	Exp 3.2	Exp 3.3	Exp 3.4	Exp 3.5
VENEZIA					
Mean BUOY	0.82	0.82	0.82	0.82	0.82
Mean SWAN	0.71	0.94	0.62	1.97	0.71
Bias	0.11	-0.12	0.20	-1.15	0.11
rmse	0.25	0.27	0.30	1.26	0.25
R	0.96	0.95	0.96	0.94	0.96
ANCONA					
Mean BUOY	0.96	0.96	0.96	0.96	0.96
Mean SWAN	0.90	1.33	0.79	2.61	0.89
Bias	0.06	-0.37	0.17	-1.65	0.07
rmse	0.23	0.47	0.31	1.87	0.25
R	0.96	0.96	0.96	0.95	0.96
MONOPOLI					
Mean BUOY	0.72	0.72	0.72	0.72	0.72
Mean SWAN	0.63	0.92	0.56	2.05	0.64
Bias	0.08	-0.20	0.16	-1.33	0.07
rmse	0.26	0.39	0.28	1.54	0.26
R	0.70	0.65	0.74	0.58	0.71

Table 3.13: Statistical indexes calculated for the *Peak Period*.

Statistical Index	Exp 3.1	Exp 3.2	Exp 3.3	Exp 3.4	Exp 3.5
VENEZIA					
Mean BUOY	4.74	4.74	4.74	4.74	4.74
Mean SWAN	4.46	3.66	4.04	6.46	4.38
Bias	0.28	1.07	0.70	-1.72	0.36
rmse	2.69	2.85	2.72	3.26	2.67
R	0.48	0.50	0.50	0.42	0.50
ANCONA					
Mean BUOY	4.98	4.98	4.98	4.98	4.98
Mean SWAN	4.82	4.49	4.45	6.78	4.78
Bias	0.16	0.49	0.53	-1.80	0.20
rmse	1.16	1.17	1.19	2.36	1.16
R	0.82	0.83	0.84	0.70	0.82
MONOPOLI					
Mean BUOY	5.21	5.21	5.21	5.21	5.21
Mean SWAN	4.39	3.86	3.95	6.10	4.34
Bias	0.82	1.34	1.25	-0.90	0.87
rmse	2.13	2.45	2.33	2.14	2.45
R	0.37	0.25	0.37	0.18	0.37

It is evident that the best combination for the *Exponential Wave Growth* and *White-Capping energy dissipation* parameterizations is the one defined ‘KOMEN’ for both as defined by *Komen et al.* [59] (see 2.3.3 and 2.3.3 for a detailed description). The second best combination is the ‘WESTH/KOMEN’, where the Exponential Wave Growth by *Yan* [106] and White-Capping by *Komen et al.* [59] are used. Hence, for all the next experiments the ‘KOMEN’ combination for Exponential Wave Growth and White-Capping dissipation is used.

Bottom Friction

In table 3.14 the model configuration used in the second group of experiments is shown:

Table 3.14: Default settings parameters used in Bottom Friction sensitivity experiments.

Parameter	Default configuration
General Parameters	
	see 3.2
Computational Mode	
	see 3.6
Geographical-Space Grid	
	see 3.2
Spectral-Space Grid	
	see 3.2
Numeric	
	see 3.2
Initial and Boundary Conditions	
	see 3.2
Forcing fields	
	see 3.10
Physical Processes: Source and Sink	
Exponential wave growth	KOMEN
White-Capping	KOMEN

In table 3.15 the list of experiments configurations to test SWAN sensitivity to *Bottom Friction* physical process is summarized.

Table 3.15: Description of the three numerical experiments performed to test SWAN sensitivity to *Bottom Friction* physical process.

Experiment Number	BOTTOM FRICTION
4.1	JONSWAP
4.2	COLLINS
4.3	MADSEN

In figures 3.16 and 3.17 the results are shown for the time series of the *Significant Wave Height* and the *Wave Peak Period* computed for all the six experiments at each ISPRA buoy location.

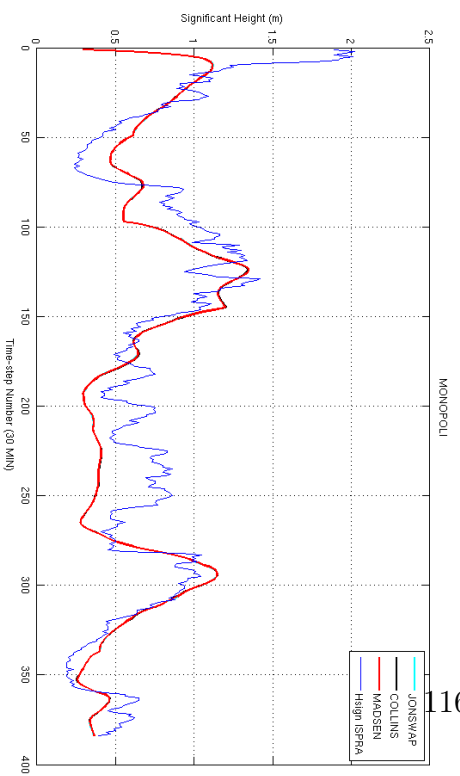
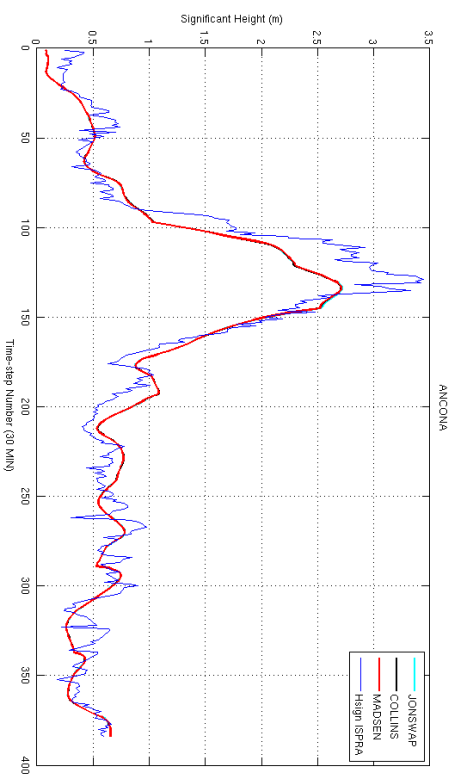
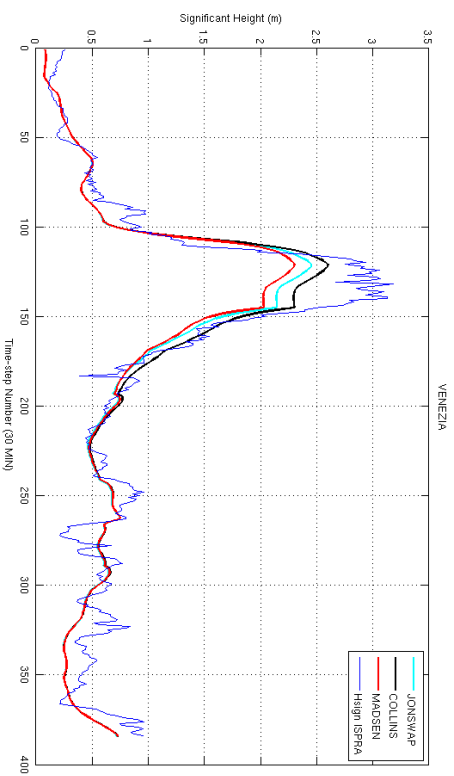
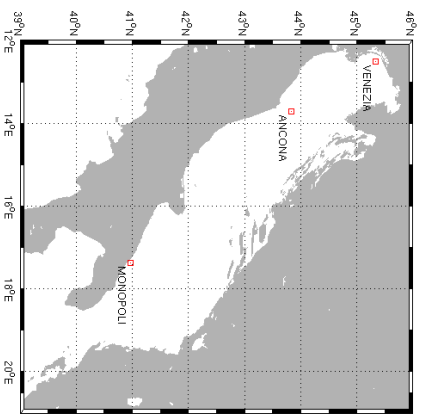


Fig. 3.16: Time series of the Significant Wave Height computed by the SWAN model at each ISFRA buoy location for the three experiments performed to test the SWAN sensitivity to Bottom Friction physical process. The simulations start on the 14.05.2013 at 00.00 and end on the 22.05.2013 at 00.00.

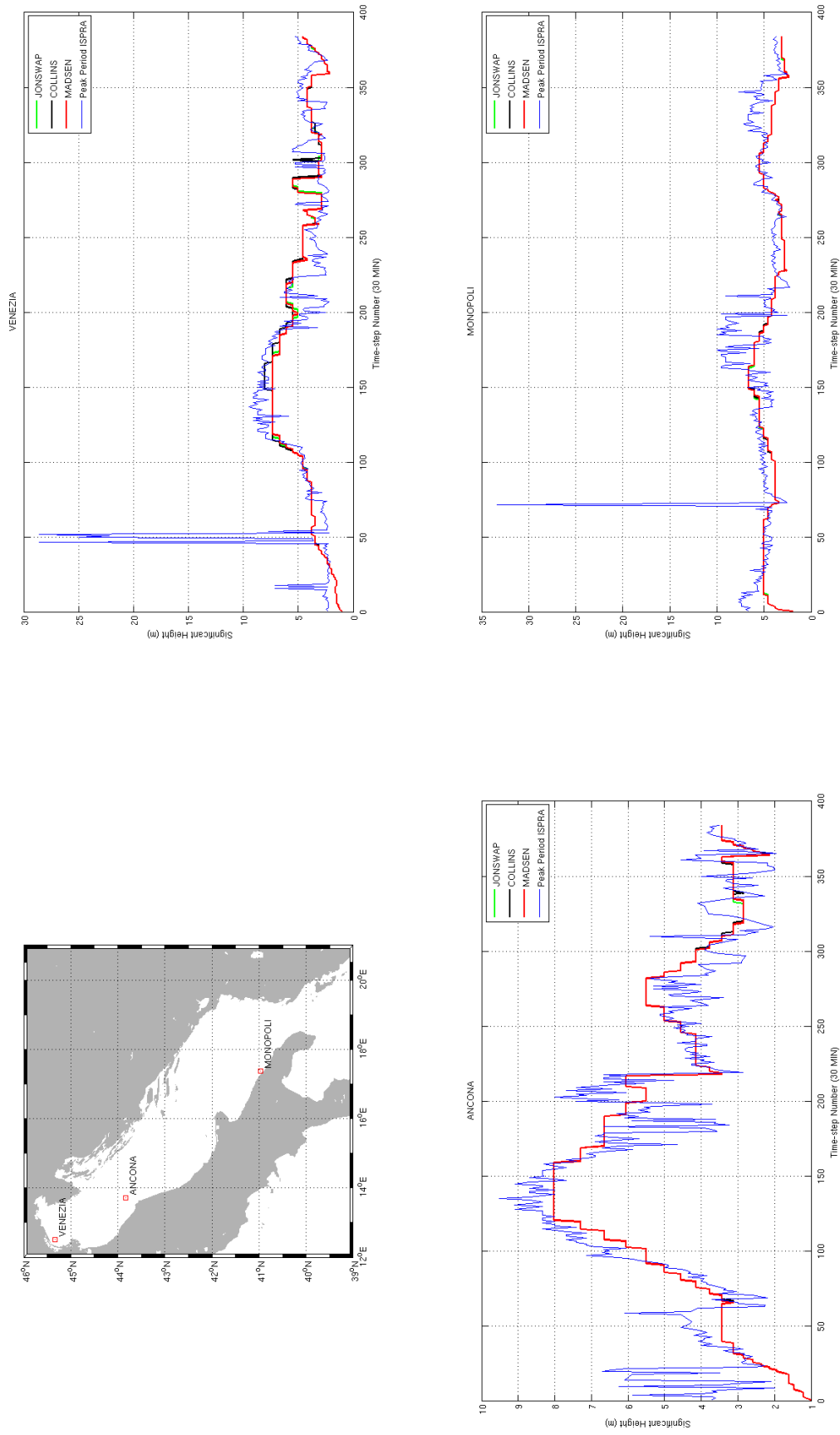


Fig. 3.17: Time series of the *Peak Period* computed by the SWAN model at each ISFRA buoy location for the three experiments performed to test the SWAN sensitivity to *Bottom Friction* physical process. The simulations start on the 14.05.2013 at 00.00 and end on the 22.05.2013 at 00.00.

In tables 3.16 and 3.13 the statistical indexes obtained from the model simulations are shown for each buoy location, both for *Wave Peak Periods* and *Significant Wave Heights*.

Table 3.16: Statistical indexes calculated for the *Significant Height*.

Statistical Index	Exp 4.1	Exp 4.2	Exp 4.3
VENEZIA			
Mean BUOY	0.82	0.82	0.82
Mean SWAN	0.71	0.74	0.70
Bias	0.11	0.08	0.13
rms	0.25	0.22	0.28
R	0.96	0.96	0.96
ANCONA			
Mean BUOY	0.96	0.96	0.96
Mean SWAN	0.90	0.90	0.90
Bias	0.06	0.06	0.06
rms	0.25	0.25	0.25
R	0.96	0.96	0.96
MONOPOLI			
Mean BUOY	0.72	0.72	0.72
Mean SWAN	0.63	0.63	0.63
Bias	0.09	0.08	0.09
rms	0.26	0.26	0.26
R	0.70	0.70	0.70

Table 3.17: Statistical indexes calculated for the *Peak Period*.

Statistical Index	Exp 4.1	Exp 4.2	Exp 4.3
VENEZIA			
Mean BUOY	4.74	4.74	4.74
Mean SWAN	4.46	4.56	4.47
Bias	0.28	0.18	0.27
rms	2.69	2.70	2.70
R	0.48	0.48	0.48
ANCONA			
Mean BUOY	4.98	4.98	4.98
Mean SWAN	4.82	4.82	4.82
Bias	0.16	0.16	0.16
rms	1.16	1.16	1.16
R	0.82	0.82	0.82
MONOPOLI			
Mean BUOY	5.21	5.21	5.21
Mean SWAN	4.39	4.39	4.39
Bias	0.82	0.82	0.82
rms	2.13	2.12	2.13
R	0.37	0.37	0.37

The best parameterization of the *Bottom Friction* physical process is the one from Collins [19] (see 2.3.3 for a description of the parameterization method) and, therefore, in the next sensitivity experiments, this configuration is adopted.

Triad Interactions

In table 3.18 the default model configuration used in the third group of experiments is shown:

Table 3.18: Default settings parameters used in Non-Linear Triads sensitivity experiments.

Parameter	Default configuration
General Parameters	
	see 3.2
Computational Mode	
	see 3.6
Geographical-Space Grid	
	see 3.2
Spectral-Space Grid	
	see 3.2
Numeric	
	see 3.2
Initial and Boundary Conditions	
	see 3.2
Forcing fields	
	see 3.10
Physical Processes: Source and Sink	
Exponential wave growth	KOMEN
White-Capping	KOMEN
Bottom friction	COLLINS

In table 3.19 the list of experiments test SWAN sensitivity to *Non-Linear Triads* physical process is summarized.

Table 3.19: Description of the two numerical experiments performed to test SWAN sensitivity to *Non-Linear Triads* physical process.

Experiment Number	TRIADS
Exp. 5.1	NO
Exp. 5.2	YES

In figures 3.18 and 3.19 the results are shown for the comparison between the model *Significant Wave Height* and *Wave Peak Period* and the ISPRA time series.

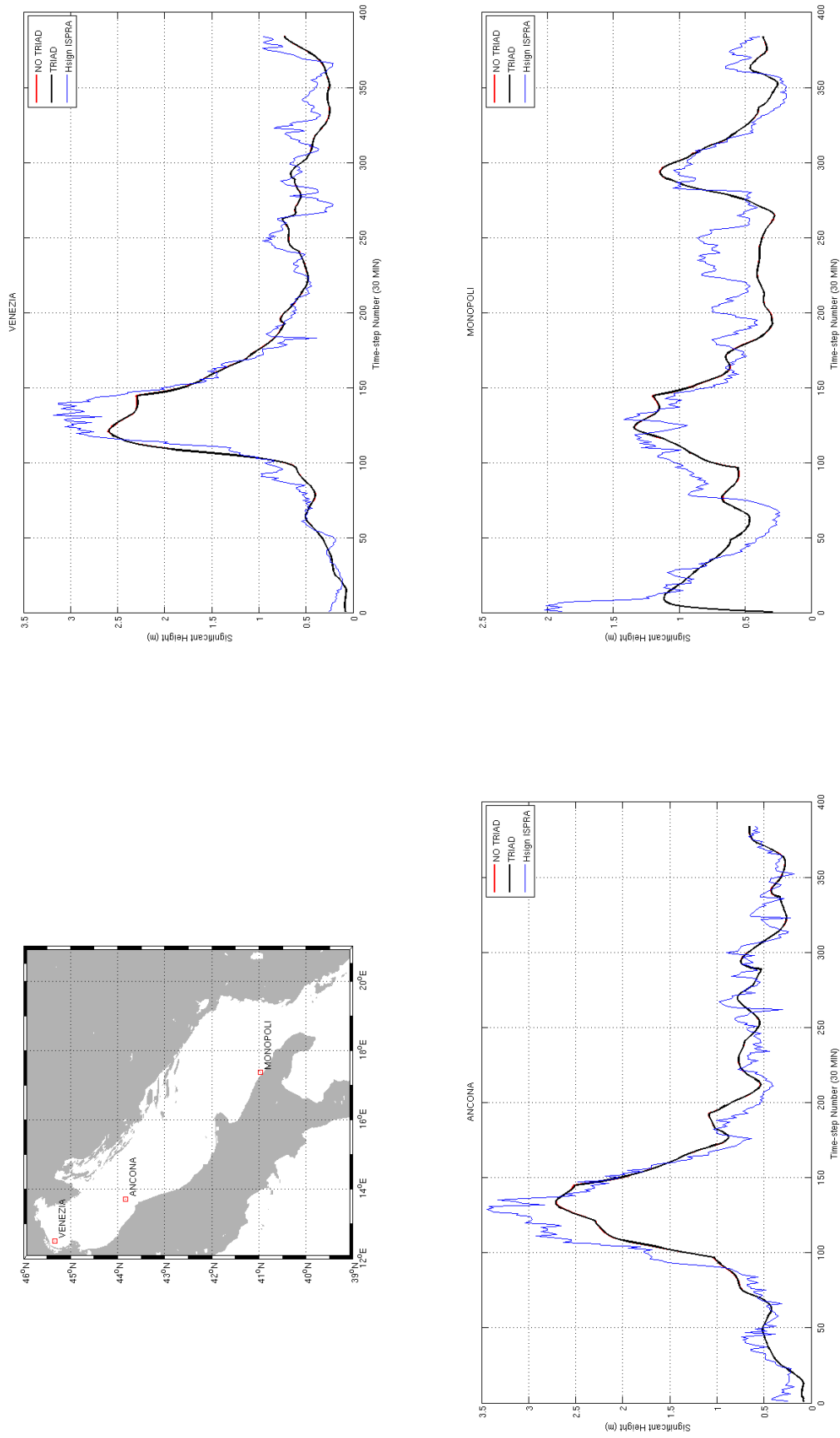


Fig. 3.18: Time series of the *Significant Wave Height* computed by the SWAN model at each ISPRA buoy location for the two experiments performed to test the SWAN sensitivity to *Non-Linear Triads* physical process. The simulations start on the 14.05.2013 at 00.00 and end on the 22.05.2013 at 00.00.

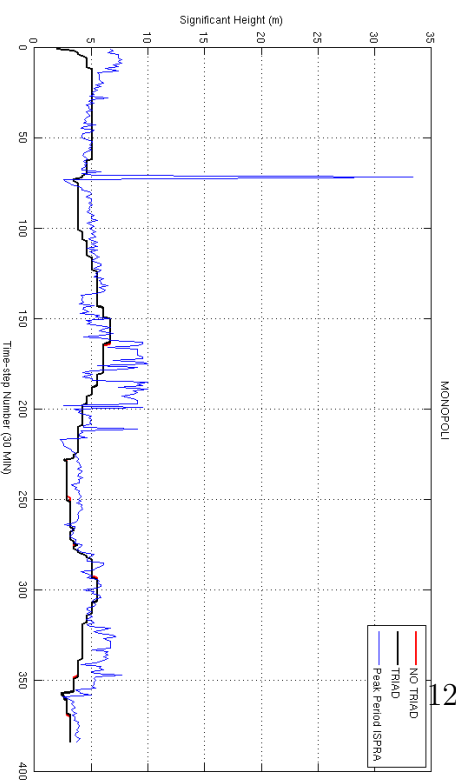
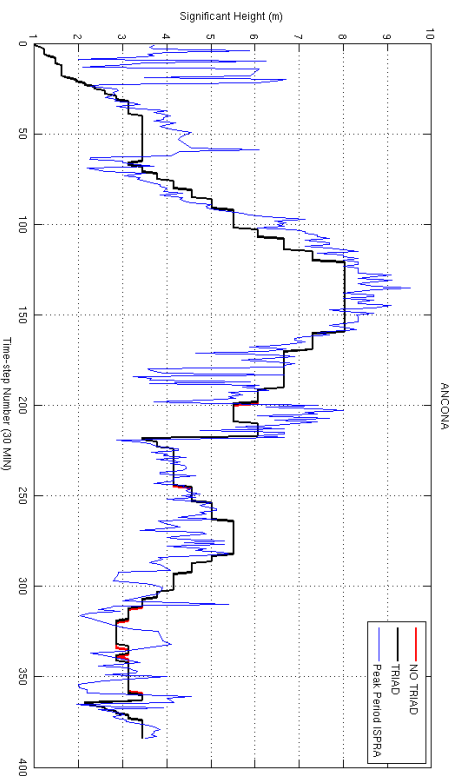
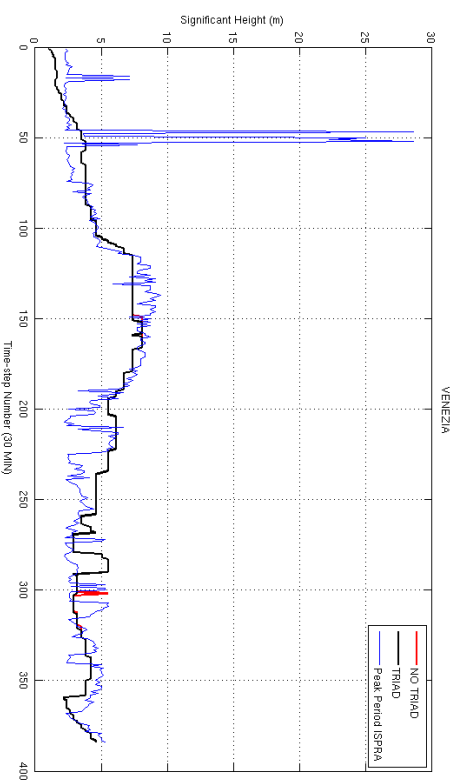
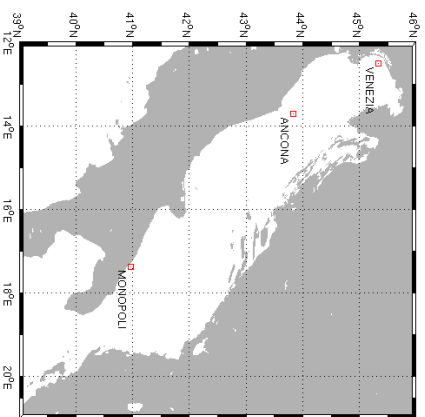


Fig. 3.19: Time series of the *Peak Period* computed by the SWAN model at each ISFRA buoy location for the two experiments performed to test the SWAN sensitivity to *Non-Linear Triads* physical process. The simulations start on the 14.05.2013 at 00.00 and end on the 22.05.2013 at 00.00.

In tables 3.20 and 3.21 the statistical indexes obtained from the model simulations are shown for each buoy location, both for *Peak Periods* and *Significant Heights*.

Table 3.20: Statistical indexes calculated for the *Significant Height*.

Statistical Index	Exp 5.1	Exp 5.2
VENEZIA		
Mean BUOY	0.82	0.82
Mean SWAN	0.74	0.74
Bias	0.08	0.08
rms	0.22	0.22
R	0.96	0.96
ANCONA		
Mean BUOY	0.96	0.96
Mean SWAN	0.90	0.90
Bias	0.06	0.07
rms	0.25	0.25
R	0.96	0.96
MONOPOLI		
Mean BUOY	0.72	0.72
Mean SWAN	0.63	0.63
Bias	0.08	0.08
rms	0.26	0.26
R	0.70	0.70

Table 3.21: Statistical indexes calculated for the *Peak Period*.

Statistical Index	Exp 5.1	Exp 5.2
VENEZIA		
Mean BUOY	4.74	4.74
Mean SWAN	4.56	4.56
Bias	0.18	0.18
rms	2.70	2.70
R	0.48	0.48
ANCONA		
Mean BUOY	4.98	4.98
Mean SWAN	4.82	4.82
Bias	0.16	0.16
rms	1.16	1.16
R	0.82	0.82
MONOPOLI		
Mean BUOY	5.21	5.21
Mean SWAN	4.39	4.39
Bias	0.82	0.82
rms	2.12	2.12
R	0.37	0.37

The Results confirm that the model simulation is insensitive to the addition triad non-Linear interactions. This result can be explained considering that *Non-Linear Triads* are a *Shallow Water* process which becomes important in areas near the coast, and in our model configuration the resolution of the spatial computational grid used is too coarse to properly represent the near-coastal processes.

3.2 SWAN Coupling with Ocean Relocatable Model

In this section the experiments performed to test the coupling between SWAN and NEMO within the SURF relocatable ocean model are described.

The coupling has been performed in order to force the SWAN model with high resolution current fields provided by the NEMO model and to evaluate the impact of high resolution currents on the wind-wave model simulations.

The relocatable modelling method focuses on the rapid implementation of an ocean model nested into a coarser scale model. It aims to be a valuable tool to be used together with wave modelling in several applications, such as oil spill monitoring, search and rescue operations, ship routing, ship traffic monitoring, etc.

3.2.1 SURF Relocatable Model

The SURF (Structured Unstructured Relocatable ocean model for Forecasting) model is based on the ocean model NEMO and the wind-wave model SWAN.

The SURF model work-flow which is shown in figure 3.20.

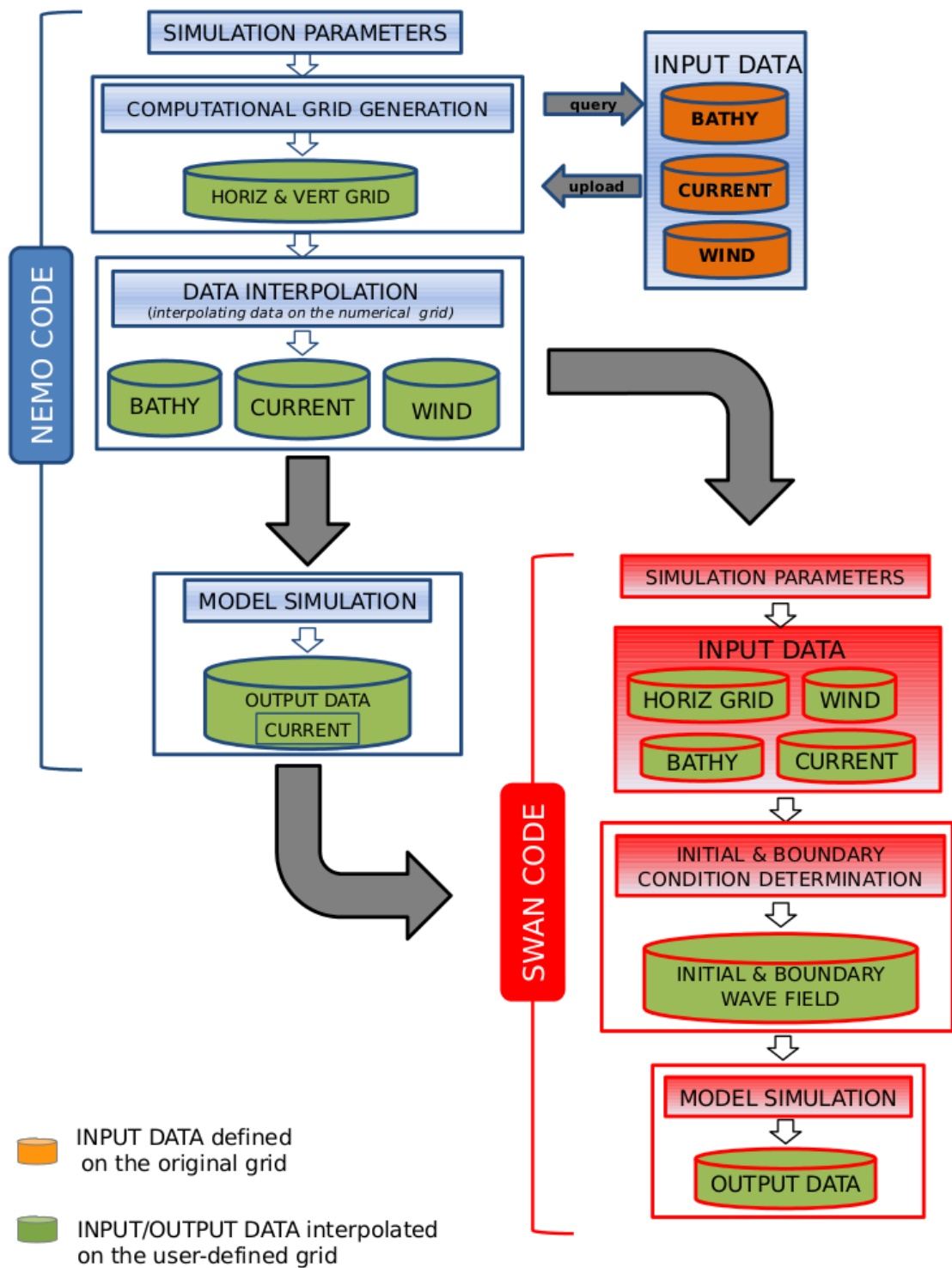


Fig. 3.20: Relocatable SURF model work-flow.

As it can be seen from figure 3.20, a SURF model run is composed of two step.

First, a **NEMO** model execution to compute the current fields for the specific area and period of interest is performed. The work-flow of the NEMO run is organized as follows:

- **Model parameters setup:** first, the simulation parameters are defined.
- **Horizontal Grid & Vertical Grid Depth:** the generation of the numerical grid is then performed.
- **Input Data Requirements:** after the model configuration and grid creation, the procedure for querying the Input Data, which might be already downloaded in the local database, is activated. Then, the next automatic step is the data reformat, which generates the forcing, boundary conditions and initial conditions files necessary to run the model. In this step the bathymetry, the wind forcing fields and the current fields needed to define boundary and initial conditions are interpolated on the model grid.
- **Model run:** the NEMO run starts. This phase involves the model compilation and its run, together with the data upload in the local database.
- **Model output:** during the execution of the main program, output files are continuously updated given the fixed output frequency. At the end of simulation, the output files are stored in the directory where the user is running the model.

After, a **SWAN** run is done to simulate the wave fields for the same area and period.

The SWAN simulation work-flow is organized as follows:

- **Model parameters setup:** in the first step, the model simulation parameters have to be defined. The horizontal grid resolution has not to be specified because the horizontal grid is generated by NEMO and given to SWAN as input.
- **Input Data Requirements:** after the model configuration, the procedure for querying the Input Data, which might be already downloaded in the local database, is activated. The SWAN input data are the

horizontal grid generated by NEMO, the bathymetry and wind forcing fields interpolated by NEMO on the horizontal grid and the surface current fields resulting from the NEMO run.

- **Initial and Boundaries condition determination:** the initial spectra are computed (also for grid points located at boundaries) from the local wind velocities.
- **Model run:** this phase involves the model compilation and its run, together with the data upload in the local database.
- **Model output:** during the execution of the main program, output files will be continuously updated given the fixed output frequency. At the end of simulation the output files will be stored in the directory where the user is running the model.

3.2.2 NEMO-SWAN Coupling Experiments

For calibration/validation purposes SURF has been implemented in a sub-region of the Tyrrhenian Sea. The whole region can be considered in deep water conditions, and avoiding the necessity of extending the study far away up to the longest fetches [15].

The spatial grid is a rectangular curvilinear regular one, with horizontal resolution of $\left(\frac{1}{40}\right)^\circ$ both in longitude and in latitude, with the Southern-West corner located at 9.35° East and 41.5° North. It consists of 130×80 points. The vertical resolution of the SURF model is of about 100 levels.

The geometry of the spatial domain and the horizontal and vertical grids used are shown in figures 3.21 and 3.22.

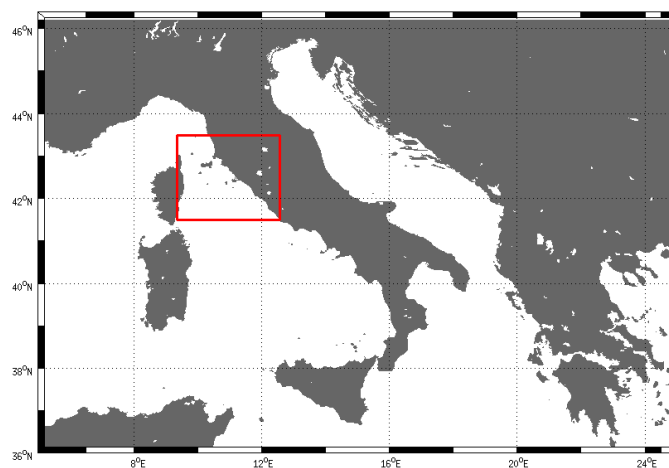


Fig. 3.21: Geometry of the spatial computational domain

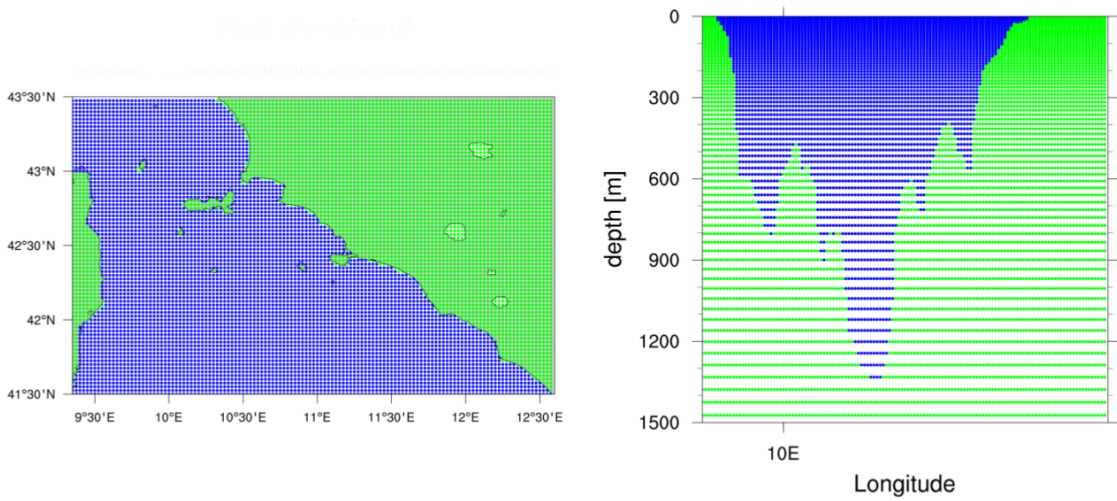


Fig. 3.22: Horizontal (on the left) and vertical (on the right) grids

SURF calculated the bathymetry (see figure 3.23) by interpolating the Digital Bathymetric Data Base Variable resolution (DBDBV) on the horizontal grid of the model. DBDBV is a digital bathymetric data base that provides ocean depths at various gridded resolutions. It was developed by the U.S. Naval Oceanographic Office (NAVOCEANO) to support the generation of bathymetric chart products, and to provide bathymetric data to be integrated with other geophysical and environmental parameters for ocean modeling. Grid resolutions available include 0.5, 1, 2, and 5 minutes of latitude/longitude. The Mediterranean Sea including the Adriatic Sea and the Black Sea has a geographic coverage of 1 minute.

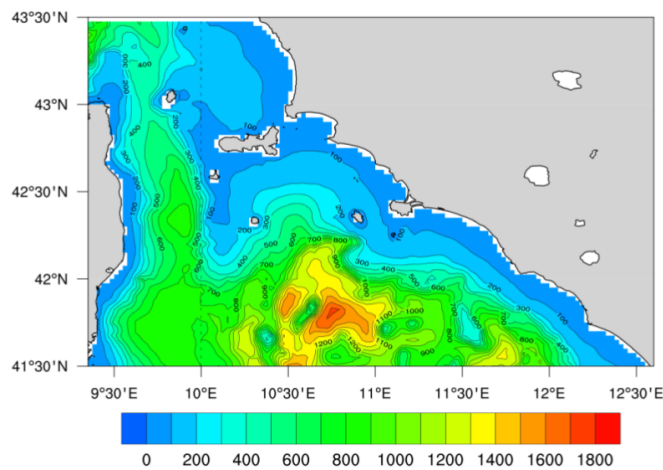


Fig. 3.23: Bathymetry of the computational domain

The NEMO and SWAN component of SURF have been forced with the high resolution SKIRON atmospheric input fields, characterized by a time resolution of one hour and a 0.025° horizontal resolution. SKIRON [96] is a modeling system developed at the University of Athens from the AM-WFG [56] [57]. The SKIRON atmospheric input fields have been processed by the *seaoverland* algorithm and interpolated on the horizontal computational grid by SURF, using the bi-linear interpolation method integrated in the NEMO code.

The integration time step used for the NEMO component of SURF computations is 50 s while for SWAN is 1800 s.

The NEMO component of SURF uses the Mediterranean Forecast System (hereafter called MFS [73]) output fields as initial conditions. MFS is forced by ECMWF atmospheric forcing and it produces analysis and forecasts.

In this initial work, closed lateral boundaries conditions are considered for both NEMO and SWAN.

The experiments performed to couple the SWAN and NEMO models have been organized as follows.

SWAN simulations started on the 14-02-2012 at 00.00 and ended on the 16-02-2012 at 00.00.

NEMO model simulated three time periods: *the first period* is between 11-02-2012 at 00.00 and 16-02-2012 at 00.00, *the second* between 09-11-2012 at 00.00 and 16-02-2012 at 00.00 and *the third* one is between 07-11-2012 at 00.00 and 16-02-2012 at 00.00.

These experiments have been performed in order to investigate the sensitivity to the initialization time, called *spin-up time*, of the NEMO relocatable model.

The *spin-up time* is defined as the time needed by an ocean model to reach a state of physical equilibrium under the applied forcing: the results cannot be trusted until this equilibrium is reached due to spurious noise in the numerical solution [23].

Therefore, adopting this experiment configuration, the SURF sensitivity to NEMO model spin up of 3, 5 and 7 days has been tested.

A summary of the computational features of the NEMO and SWAN model used in these experiments is given in tables 3.22 and 3.23, respectively, while the list of the experiments is shown in table 3.24.

Table 3.22: NEMO computational setting.

Parameter	Configuration/Value
Time Parameters	
Computational time step Δt	50 s
Output frequency Δt	3600 s
Horizontal Grid	
Coordinates	spherical
Computational grid	curvi-linear grid
Resolution in lon-direction	$\left(\frac{1}{40}\right)^\circ$
Number of meshes in lon-direction	130
Resolution in lat-direction	$\left(\frac{1}{40}\right)^\circ$
Number of meshes in lat-direction	80
Vertical Grid	
Number of meshes in z-direction	100
Max stretching level h_{th}	101.83 m
Stretching factor h_{cr}	50.0
Sub-grid Physical Processes	
A^{vm}	$1.2 \times 10^{-5} m^2 s^{-1}$
A^{lm}	$-5 \times 10^9 m^4 s^{-1}$
A^{vT}	$1.2 \times 10^{-6} m^2 s^{-1}$
A^{lT}	$-3 \times 10^9 m^4 s^{-1}$
Forcing Input Data	
Wind forcing data	<i>SKIRON</i> analysis
Initial and Boundary Conditions	
Initial condition	MFS field
Lateral boundaries	No flux
Bottom boundary C_D	0.001

Table 3.22: SURF computational setting.

Table 3.23: SWAN computational setting.

Parameter	Configuration/Value
General Parameters	
Gravitational Acceleration	$9.81ms^{-2}$
Water Density	$1025 kgm^{-3}$
Wind Drag Coefficient	no cutting off the drag coefficient
Spectral Output	based on variance spectrum
Convection for wind and wave direction adopted	nautical
Shape of spectral tail above [<i>fhigh</i>]	automatic
Maximum Froude number	0.8
Time Parameters	
Time mode	Non-Stationary
Spatial mode	Two-Dimensional
Computational time step Δ_t	1800 s
Output frequency Δ_t	1800 s
Spatial Grid	
Coordinates	spherical
Computational grid	curvi-linear grid
Number of meshes in lon-direction	130
Number of meshes in lat-direction	80
Spectral-Space Grid	
Spectral direction grid	cover the full circle
Number of meshes in θ space	36
Lowest discrete freq. used in calculation	$0.04 Hz$
Highest discrete freq. used in calculation	$1.0 Hz$
Number of meshes in <i>frequency</i> space	35
Forcing Input Data	
Wind forcing data	<i>SKIRON</i> analysis
Current forcing data	<i>SURF 1 hour</i>
Numeric	
Numerical scheme	BSBT
Max number of iterations per time step	100
Initial and Boundary Conditions	
First time	Initial wave-filed computed

Table 3.23: SWAN computational setting.

Parameter	Configuration/Value
step of the computation	from local wind velocities
Each next restart	Initial wave-field read from hotstart file
Physical Processes: Source and Sinks	
Linear wave growth by wind input	<i>Cavaleri-Melanotte</i> formulation with $[AGROW] = 0.015$, where $[AGROW]$ is the prop. coefficient for linear wave growth term
Exponential wave growth by wind input	<i>Komen</i> formulation with $[cds2] = 2.36e - 5$, $[stpm] = 3.02e - 3$ where $[cds2]$ is the coeff. for the the rate of whitecapping dissipation and $[stpm]$ is the value of the wave steepness for a Pierson-Moskowitz spectrum
Quadruplet	fully explicit computation of the non linear transfer with DIA algorithm ($[iquad] = 2$)
Friction	COLLINS bottom friction dissipation
Wave Breaking	constant breaker parameter with $[\alpha] = 1$ and $[\gamma] = 0.73$, where $[\alpha]$ is prop. coefficient of the rate of dissipation and $[\gamma]$ is the ratio of maximum individual wave height over depth

Table 3.23: SWAN computational setting.

Table 3.24: Description of the three numerical experiments performed to test SURF-SWAN coupling.

Experiment Number	NEMO simulation spin-up	SWAN simulation start-end
6.1	3 days	14-02-2012, 00.00 16-02-2012, 00.00
6.2	5 days	14-02-2012, 00.00 16-02-2012, 00.00
6.3	7 days	14-02-2012, 00.00 16-02-2012, 00.00

Validation of results has been done comparing the *Significant Wave Height* and the *Wave Peak Period* measured by the ISPRA directional buoys located at Civitavecchia and the SWAN simulations.

The locations of the ISPRA directional buoy are shown in figure 3.24.

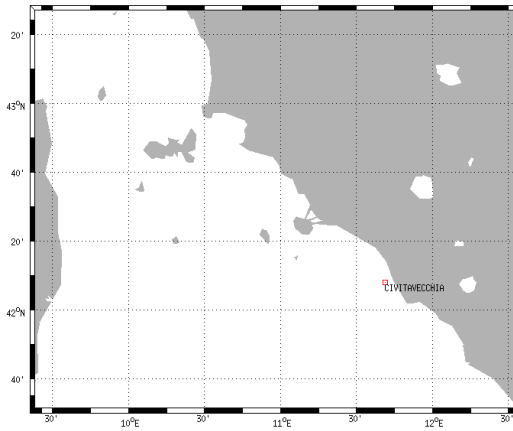


Fig. 3.24: Spatial location of the ISPRA directional buoy placed at Civitavecchia offshore waters.

Three example of the zonal current fields calculated by NEMO on 15-02-2012 at 14.00 with different spin-up times and their differences are shown in figures 3.25 and 3.26, respectively.

The results of the coupling experiments are shown in figures 3.27 and 3.28: in picture 3.27, the time series of the *Significant Wave Height* computed in the three experiments by the SWAN model at the ISPRA Civitavecchia buoy location is compared with the time series of the *Significant Wave Height* sampled by the ISPRA buoy, while in figure 3.28 the same is done for the *Peak Period*.

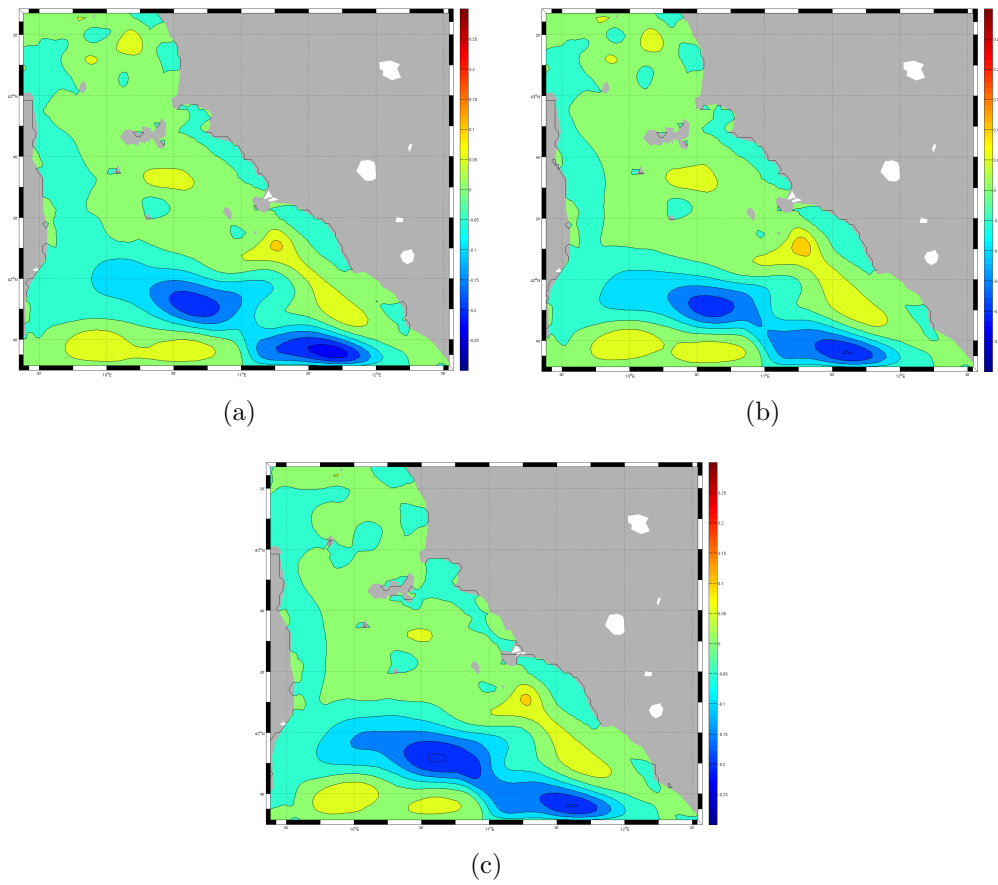


Fig. 3.25: Three sample results of the zonal current fields calculated by NEMO on 15-02-2012 at 14.00 with (a) spin-up time of 3 days, (b) spin-up time of 5 days and (c) spin-up time of 7 days.

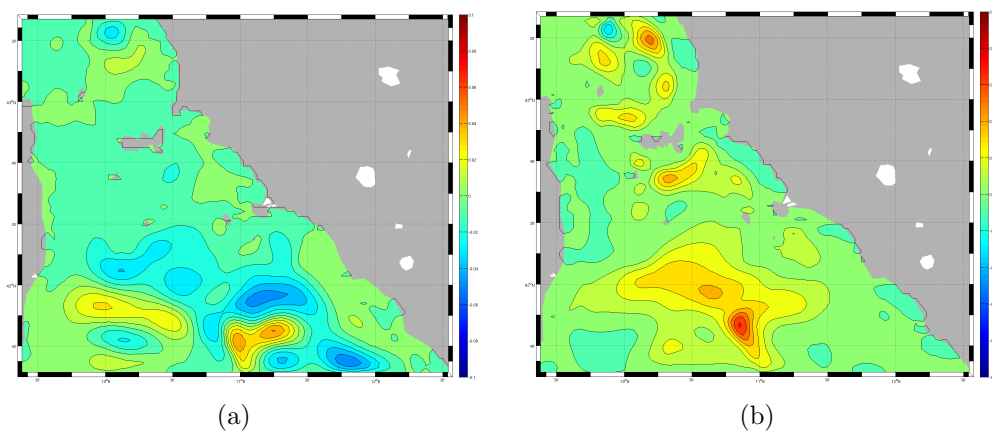


Fig. 3.26: Differences between the zonal current fields calculated by NEMO on 15-02-2012 at 14.00 with (a) 3 and 5 days or (b) 5 and 7 days of spin-up times.

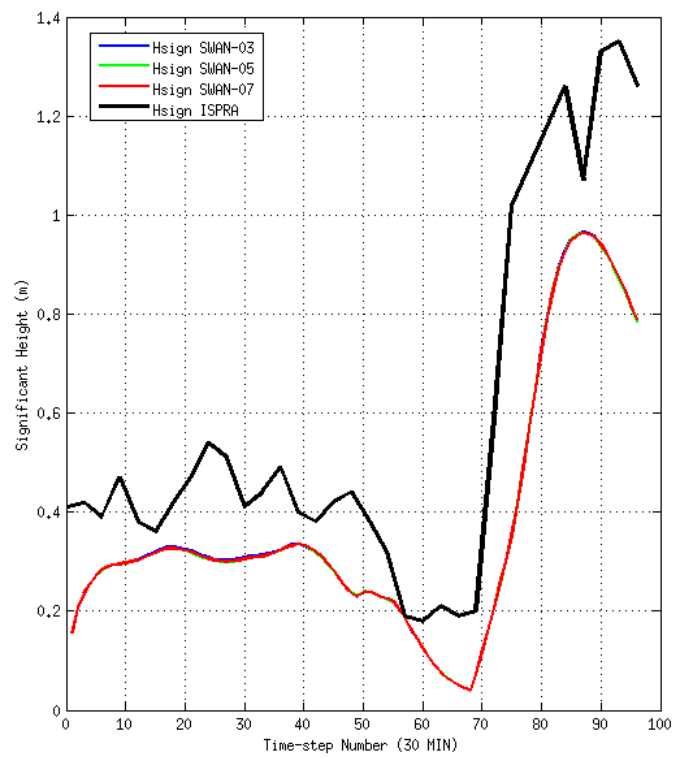


Fig. 3.27: Time series of the *Significant Height* computed in the three experiments 6.1, 6.2 and 6.3 at the ISPRA Civitavecchia buoy location for the period between 14-02-2012 at 00.00 and 16-02-2012 at 00.00.

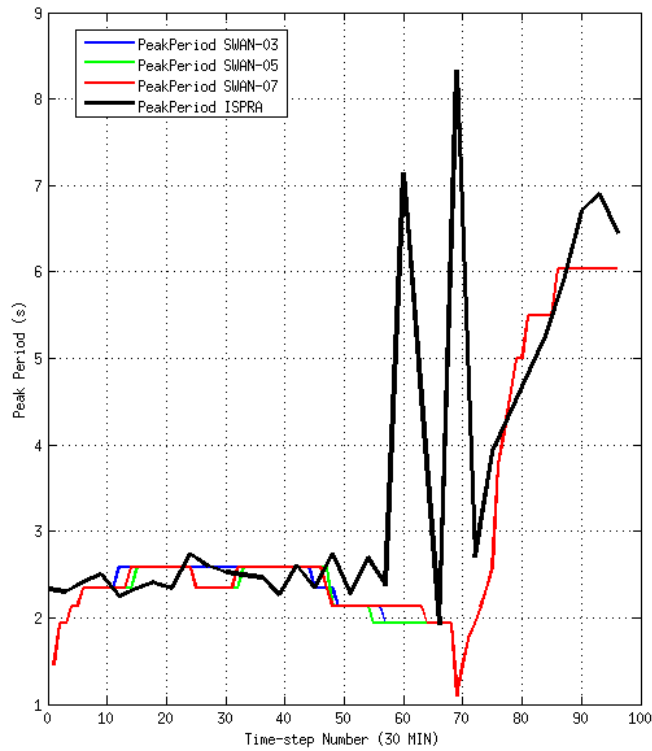


Fig. 3.28: Time series of the *Wave Peak Period* computed in the three experiments 6.1, 6.2 and 6.3 at the ISPRA Civitavecchia buoy location for the period between 14-02-2012 at 00.00 and 16-02-2012 at 00.00. .

The results evaluated in terms of Statistical indexes are shown in tables 3.25 and 3.26 both for *Wave Peak Periods* and *Significant Wave Heights*.

Table 3.25: Statistical indexes calculated for the *Significant Height*.

Statistical Index	Exp 1.1	Exp 1.2	Exp 1.3
CIVITAVECCHIA			
Mean BUOY	0.55	0.55	0.55
Mean SWAN	0.36	0.36	0.36
Bias	0.19	0.19	0.19
rmse	0.24	0.24	0.24
R	0.93	0.93	0.93

Table 3.26: Statistical indexes calculated for the *Peak Period*.

Statistical Index	Exp 1.1	Exp 1.2	Exp 1.3
CIVITAVECCHIA			
Mean BUOY	3.55	3.55	3.55
Mean SWAN	2.90	2.88	2.90
Bias	0.65	0.67	0.65
rmse	1.74	1.75	1.75
R	0.53	0.53	0.53

The sensitivity of SWAN results to the NEMO spin-up time is small because also NEMO currents are not very different (see figure 3.26).

These results are in disagreement with previous studies (*De Dominicis et al.* [23] and *Simoncelli et al.* [94]) that demonstrated the influence of the spin-up time on the accuracy of the currents simulations performed by a nested model and this is due to the closed lateral boundary conditions used by NEMO.

3.3 SWAN Coupling with the Oil-Spill Model

In this section, the description of the numerical experiments carried out to couple the SWAN wave model with the MEDSLIK-II oil-spill model is given.

3.3.1 MEDSLIK-II Model

MEDSLIK-II is an oil spill model designed to predict the transport and weathering of an oil spill or to simulate the movement of a floating object and its code is a freely available community model which can be downloaded from <http://gnoo.bo.ingv.it/MEDSLIKII>.

The oil movement in the sea water is related to advection by the large-scale flow field and dispersion by turbulent flow components while its concentration time evolution is due to several *weathering* processes.

The general equation which describes the evolution of a tracer concentration, $C(\vec{x}, t)$, with units of mass over volume, mixed in the marine environment, is

$$\frac{\partial C}{\partial t} + \vec{U} \cdot \vec{\nabla} C = \vec{\nabla} \cdot (K_{i,j} \cdot \vec{\nabla} C) + \sum_{k=1}^M r_k(\vec{x}, C(\vec{x}, t), t) \quad (3.5)$$

where $\partial/\partial t$ is the local time-rate-of-change operator, \vec{U} is the sea current mean field with components (U, V, W) , $K_{i,j}$ is the diffusivity tensor which parameterizes the turbulent effects, and $r_k(C)$ are the M transformation rates that modify the tracer concentration by means of physical and chemical transformation processes.

MEDSLIK-II is a Lagrangian model, which means that the oil slick is represented by a number N of constituent particles moved by advection from the hydrodynamics currents and dispersed horizontally by Lagrangian turbulent diffusion.

In order to describe the oil concentration evolution within a Lagrangian formalism some fundamental assumptions have to be made: the constituent particles do not influence water hydrodynamics and processes, they move through infinitesimal displacements without inertia and without interacting

among themselves, while physical and chemical processes act on the entire slick rather than on the single particles properties. If these assumptions apply, then it is possible to split the active tracer equation into two component equations:

$$\frac{\partial C_w}{\partial t} = \sum_{k=1}^M r_k(\vec{x}, C(\vec{x}, t), t) \quad (3.6)$$

and

$$\frac{\partial C}{\partial t} = -\vec{U} \cdot \vec{\nabla} C_w + \vec{\nabla} \cdot (K_{i,j} \cdot \vec{\nabla} C_w) \quad (3.7)$$

where C_w is the oil concentration solution solely due to the weathering processes, while the final time rate of change of C is given by the advection-diffusion acting on C_w .

Equation 3.6 is solved by MEDSLIK-II considering that the transformation processes act on the total oil slick volume and, as result, *oil slick state variables* are defined. Then, Lagrangian particle formalism is applied to solve equation 3.7, which means to discretize the oil slick in N particles with associated *particle state variables* (some of which are deduced from the oil slick state variables defined in the previous step). Finally, the oil concentration is then computed by assembling the particles together with their associated properties.

The surface volume V_S of the oil-slick is broken into N constituent particles that are characterized by a particle volume, $v(t)$, by a particle status index $\sigma(t)$ which is set equal to zero if the particle is located on the surface or equal to one if the oil particle is a subsurface or dispersed one, and by a particle position vector defined as

$$\vec{x}_k(t) = (x_k(t), y_k(t), z_k(t)), \quad k = 1, N \quad (3.8)$$

The time rate of change of particle positions in the oil tracer grid is given by n_k uncoupled *Langevin* equations:

$$\frac{d\vec{x}_k(t)}{dt} = A_{i,j}(\vec{x}_k, t) + B_{p,q}(\vec{x}_k, t)\xi(t) \quad (3.9)$$

where the tensor $A_{i,j}(\vec{x}_k, t)$ is the deterministic part of the flow field, i.e, the mean field \vec{U} in equation 3.5, while the second term $B_{p,q}(\vec{x}_k, t)\xi(t)$ is a stochastic term representing the diffusion term in equation 3.5.

It can be shown (see [25] for a rigorous explanation) that, considering $A_{i,j}(\vec{x}_k, t)$ and $B_{p,q}(\vec{x}_k, t)$ as diagonal tensors, it is possible to write

$$d\vec{x}_k(t) = [\vec{U}_C(x_k, y_k, 0, t) + \vec{U}_W(x_k, y_k, t) + \vec{U}_S(x_k, y_k, t) + \vec{U}_D(x_k, y_k, t)]dt + d\vec{x}'_k(t) \quad (3.10)$$

for oil particles located on the surface (i.e., characterized by $\sigma = 0$) and, for particles on the subsurface or dispersed in the water column (i.e., with $\sigma = 1$),

$$d\vec{x}_k(t) = \vec{U}_C(x_k, y_k, z_k, t)dt + d\vec{x}'_k(t) \quad (3.11)$$

where \vec{U}_C is the Eulerian current velocity term due to a combination of non-local wind and buoyancy forcings, mainly coming from operational oceanographic numerical model forecasts or analyses, \vec{U}_W is the local wind velocity correction term (thus the Ekman currents due to local winds [80] [61]), \vec{U}_S is the wave-induced current term (*Stokes drift* velocity), \vec{U}_D is the wind drag correction due to emergent part of the objects at the surface and $d\vec{x}'_k(t)$ is the displacement due to the turbulent diffusion.

The local wind correction term $\vec{U}_W = (U_W, V_W)$ can be parameterized as a function of wind intensity and angle between winds and currents:

$$U_W = (\alpha W_x \cos \beta + W_y \sin \beta) \quad (3.12)$$

$$V_W = (\alpha - W_x \sin \beta + W_y \cos \beta) \quad (3.13)$$

where W_x and W_y are the wind zonal and meridional components at 10 m, respectively, and α and β are two parameters referred to as drift factor and drift angle.

On the other hand, the *Stokes drift* velocity \vec{U}_S is defined as

$$U_S = D_S \cos \theta \quad (3.14)$$

$$V_S = D_S \sin \theta \quad (3.15)$$

where $\theta = \arctan(W_x/W_y)$ and D_S is the Stokes drift velocity intensity in the direction of the wave propagation at the surface defined as

$$D_S \Big|_{z=0} = 2 \int_0^\infty \omega k(\omega) S(\omega) d\omega \quad (3.16)$$

where ω is the angular frequency, k is the wave-number and $S(\omega)$ is the wave spectrum and where it has been assumed that wind and waves are aligned and that waves are generated only by the local wind (thus swell process is not considered).

The wind drag correction, U_D , is a parameterization for the leeway (windage) of a floating object, defined as the drift associated with the wind force on the overwater structure of the object and, following [88], can be defined as

$$\vec{U}_D = \sqrt{\frac{\rho_a A_a C d_a}{\rho_w A_w C d_w}} \vec{W} = \gamma \vec{W} \quad (3.17)$$

where ρ , A and Cd are the fluid density, projected areas of the object and drag coefficient, respectively, and subscripts a and w denote the air and sea-water environments and \vec{W} is the wind velocity vector.

The turbulent diffusion is parameterized as a random walk scheme given by the equation

$$d\vec{x}'_k(t) = \sqrt{2K_{i,j}} dt \vec{Z} \quad (3.18)$$

where $K_{i,j}$ is the horizontally isotropic turbulent diffusion diagonal tensor given by

$$K_{i,j} = \begin{vmatrix} K_h & 0 & 0 \\ 0 & K_h & 0 \\ 0 & 0 & K_v \end{vmatrix}.$$

and \vec{Z} is a vector of independent random numbers Z_1, Z_2, Z_3 used to model the Brownian random walk processes chosen for the parametrization of turbulent diffusion.

MEDSLIK-II is also able to take into account adsorption of oil by the coast should the slick reach it. A complete description of all the model features is

given in [25] [24].

In order to show the benefit of using SWAN to compute the Stokes' Drift correction term in equation 3.28 we have developed the computation of the Stokes' Drift from SWAN model output.

3.3.2 Stokes Drift Calculation

Stokes Drift for Random Gravity Waves

The general equation for the *Stokes Drift* velocity associated to a *random gravity waves* field is briefly considered in this paragraph.

Let us consider a statistically stationary, Gaussian, ergodic and horizontally homogeneous wave field: according to the *Linear Theory* and the *Random Phase-Amplitude Model*, the surface displacement $\eta(\vec{x}, t)$ can be represented as a superposition of sinusoidal free progressive waves generated by wind in different times and places:

$$\underline{\eta}(\vec{x}, t) = \sum_{n=1}^N \sum_{m=1}^M \underline{a}_{n,m} \cos(K_n \cos \theta_m \hat{i} + K_n \sin \theta_m \hat{j} - \omega_n t + \underline{\varphi}_{n,m}) \quad (3.19)$$

where $\underline{a}_{n,m}$ is the *amplitude*, K_n is the magnitude of the wavenumber vector (i.e., $|\vec{K}_n|$), θ_m is the angle between the x -axis and the direction of wave propagation and \hat{i} and \hat{j} are the fundamental versors in the x and y direction respectively, ω_n is the *absolute* frequency and $\varphi_{n,m}$ is the *phase* of the $(n, m)^{th}$ wave component.

The *dispersion relationship* of the n^{th} harmonic wave components is:

$$\omega_n^2 = gK_n \tanh(K_n h) \quad (3.20)$$

where g is the *gravity acceleration* and h is the total mean *water depth* defined as $h = \bar{\zeta} + h_b$, where $\bar{\zeta}(\vec{x}, t)$ is the mean free surface displacement and $h_b(\vec{x})$ is the depth of the bottom with respect to the unperturbed surface level.

By applying the Stokes' method [97] described in 2.1.6 section, the *ensemble* mean second-order drift velocity for the wave field 3.19 can be derived (see [58] for a detailed mathematical derivation) and the result is that *the total mean drift associated to a random gravity waves field is the superposition of the drifts resulting from each wave component*, thus

$$\vec{U}_S(z) = \sum_{n=1}^N \sum_{m=1}^M \vec{u}_s^{n,m} = \sum_{n=1}^N \sum_{m=1}^M a_{n,m}^2 \omega_n \vec{K}_{n,m} \frac{\cosh(2|\vec{K}_{n,m}|(h+z))}{2 \sinh^2(|\vec{K}_{n,m}|h)} \quad (3.21)$$

where $\vec{u}_s^{n,m}$ is the stokes drift velocity associated to the $(n, m)^{th}$ wave component, N and M are the number of the discretized frequencies and directions, respectively, and the second part of the equation result by applying equation 2.81 to each harmonic component.

Distributing the $\vec{u}_s^{n,m}$ over the frequency and direction intervals Δf_n and $\Delta \theta_m$ for each frequency f_n and direction θ_m and imposing that the two frequency and direction bands Δf_n and $\Delta \theta_m$ have to approach to 0, a continuous function for *the total mean drift* can be derived as

$$\vec{U}_S(z) = \int_{-\infty}^{\infty} \int_0^{\infty} a^2 \omega \vec{K} \frac{\cosh(2|\vec{K}|(h+z))}{2 \sinh^2(|\vec{K}|h)} df d\theta \quad (3.22)$$

Considering now that from equation 2.56 the energy associated to a sinusoidal wave component is

$$E = \frac{1}{2} \rho g a^2 \quad (3.23)$$

where ρ denotes *sea water density* at the surface, then it is possible to write

$$a^2 = \frac{2E}{\rho g} \quad (3.24)$$

Remembering now the relationship between the energy and frequency-directional wave spectrum derived in equation 2.104, thus

$$E = \rho g S(f, \theta) df d\theta \quad (3.25)$$

it is possible to write

$$a^2 = 2S(f, \theta) df d\theta \quad (3.26)$$

and, therefore, the general formulation for arbitrary deep water of the stokes drift velocity associated to a random gravity waves field is

$$\vec{U}_S(z) = 2 \int_{-\infty}^{\infty} \int_0^{\infty} \omega \frac{\cosh(2|\vec{K}|(h+z))}{2 \sinh^2(|\vec{K}|h)} \vec{K} S(f, \theta) df d\theta \quad (3.27)$$

and the components of the velocity vector $\vec{U}_S = (U_S, V_S)$ are

$$\begin{cases} U_S(z) = 2 \int_{-\infty}^{\infty} \int_0^{\infty} \omega \frac{\cosh(2|\vec{K}|(h+z))}{2 \sinh^2(|\vec{K}|h)} |\vec{K}| \cos \theta S(f, \theta) df d\theta \\ V_S(z) = 2 \int_{-\infty}^{\infty} \int_0^{\infty} \omega \frac{\cosh(2|\vec{K}|(h+z))}{2 \sinh^2(|\vec{K}|h)} |\vec{K}| \sin \theta S(f, \theta) df d\theta \end{cases} \quad (3.28)$$

Assuming that the deep water approximation applies, equation 3.27 become

$$\vec{U}_S(z) = 2 \int_{-\infty}^{\infty} \int_0^{\infty} \omega \vec{K} e^{2|\vec{k}|z} S(f, \theta) df d\theta \quad (3.29)$$

which can be written as

$$\vec{U}_S(z) = \frac{16\pi^3}{g} \int_{-\infty}^{\infty} \int_0^{\infty} f^3 e^{\frac{8\pi^2 f^2 z}{g}} S(f, \theta) df d\theta \quad (3.30)$$

remembering that $\omega = 2\pi f$ and $|\vec{K}| = \omega^2/g$.

According to *Stokes* [97], the Stokes' drift vertical decay rate is twice that one for the Eulerian velocity components (see section 2.1.6). It implies therefore that the Stokes' drift is confined very close to the sea surface.

Hence, considering only the Stokes' drift on the surface, equations 3.27 and 3.29 can be rewritten as follows:

$$\vec{U}_S \Big|_{z=0} = 2 \int_{-\infty}^{\infty} \int_0^{\infty} \omega \frac{\cosh 2|\vec{K}|h}{2 \sinh^2 |\vec{K}|h} \vec{K} S(f, \theta) df d\theta \quad (3.31)$$

$$= 2 \int_{-\infty}^{\infty} \int_0^{\infty} \frac{g|\vec{K}|}{\omega \tanh(2|\vec{K}|h)} \vec{K} S(f, \theta) df d\theta \quad (3.32)$$

considering trigonometric equalities, and

$$\vec{U}_S \Big|_{z=0} = 2 \int_{-\infty}^{\infty} \int_0^{\infty} \omega \vec{K} S(f, \theta) df d\theta = \frac{16\pi^3}{g} \int_{-\infty}^{\infty} \int_0^{\infty} f^3 S(f, \theta) df d\theta \quad (3.33)$$

respectively.

Stokes Drift Calculation from Spectral Model Output

The Stokes drift velocity calculated by MEDSLIK-II is the mean drift velocity at the surface assuming that deep water conditions applies. The JONSWAP frequency spectrum [41] is used and the wave field is in the wind direction.

Therefore, MEDSLIK-II computes the Stokes' Drift using 3.33 in the following form:

$$\begin{cases} U_S = 2 \left(\int_0^\infty \omega k(\omega) S_J(\omega) d\omega \right) \cos \theta \\ V_S = 2 \left(\int_0^\infty \omega k(\omega) S_J(\omega) d\omega \right) \sin \theta \end{cases} \quad (3.34)$$

where θ is the direction of the wind velocity vector $\vec{W} = (W_x, W_y)$ defined as $\theta = \arctan \left(\frac{W_x}{W_y} \right)$.

In order to improve the accuracy of the stokes drift calculation and, hence, of the trajectories simulations, we want to calculate the mean drift velocity using the directional-frequency spectra resulting from SWAN simulations in equation 3.32 and compare these results with the MEDSLIK-II parameterization 3.34.

Consider now equation 3.32: a numerical solutions for these equations can be found writing a code that calculates the module of the wave-number vector $|\vec{K}|$ for each discretized frequency of the spectral domain and which solves the double integral in the $\sigma - \theta$ space.

Therefore, in order to numerically solve equation 3.32, the SWAN model output has been post-processed with the following procedure:

- First, an algorithm to numerically solve the general dispersion relationship for K has been implemented;
- Then, the trapezoidal rule has been implemented to find a numerical solution of the double integral. This algorithm has been applied to find the mean wave directions and results have been compared to mean wave directions calculated by SWAN in order to validate the double integral solving rule.

- In the last, the rectangle rule has been implemented too. Then, both the trapezoidal and the rectangle rules have been used to calculate the stokes drift velocity and results have been compared with the mean directions calculated by SWAN, considering that the stokes drift direction is approximately equal to the mean wave direction.

In order to test the above methodology, the SWAN model outputs of the SURF experiments have been used (see 3.2.2 for a description of the SWAN computational domain and its computational features).

Wave Number Numerical Computation: according to the *Linear Theory* (see section 2.1), the general relationship which links the angular frequency ω to the wave-number module $|\vec{K}|$ is

$$\omega = g|\vec{K}| \tanh |\vec{K}|h \quad (3.35)$$

where g is the gravitational acceleration and H is the water depth. Equation 3.35 can be rewritten for $|\vec{K}|$ as

$$|\vec{K}| \tanh |\vec{K}|h = \frac{4\pi^2 f^2}{g} \quad (3.36)$$

remembering that $\omega = 2\pi f$, where f is the frequency expressed in Hz. Equation 3.36 is a transcendental one and, in order to numerically solve it with a specified accuracy by an iterative computation, it is useful to rewrite it as

$$x \tanh x = D \quad (3.37)$$

where $x = |\vec{K}|H$ and $D = \frac{4\pi^2 f^2 H}{g}$.

Following *Goda* [34], it is a good procedure to first rewrite equation 3.37 as follows in order to remove the inflection point:

$$y(x) = x - D \coth x \quad (3.38)$$

Equation 3.38 can be solved using the *Newton's iterative method*, which is based on the following equation (see [83] and [84] for a detailed review of the Newton's method applied to solve non-linear equations and non-linear systems):

$$x^{(k+1)} = x^{(k)} - \frac{y(x^k)}{y'(x^k)} = x^{(k)} - \frac{x^k - D \coth x^k}{1 + D(\coth^2 x^k - 1)} \quad (3.39)$$

It can be shown that Newton's method convergence is not ensured for every $x^{(k)}$ chosen, but only for each $x^{(k)} \in I(\alpha)$, where α is the real zero of the function studied and $I(\alpha)$ is a small enough around of α (see [83] and [84] for a rigorous demonstration).

Following *Goda* [34], the best estimate for the initial value of $x^{(k)}$ is

$$x^{(k)} = \begin{cases} D, & \text{for } D \geq 1 \\ D^{1/2} & \text{for } D < 1 \end{cases} \quad (3.40)$$

In order to validate the implemented code, for some arbitrary chosen wave period T and the depth H values the wave-number modulo has been calculated and results have been compared with that ones listed in *Goda* [34]. Some of the results are listed in table 3.27.

Table 3.27: Wave-number modulo values calculated with the Fortran 90 code in Appendix ?? and given by *Goda* [34].

Wave Period T in seconds	Water Depth h in meters	Goda [34] K value	K value
2.00	1.80	5.96	5.96
8.00	75.00	99.81	99.81
14.00	120.00	301.60	301.60

As it can be seen from table 3.27, the algorithm developed, at the second order of accuracy, exactly reproduces the wave-number values given by *Goda* [34], validating it.

Test of the Double Integral Composite Trapezoidal rule: the numerical *Composite Trapezoidal rule* for two dimensional functions has been implemented to numerically solve the double integral in equation 3.32.

In these experiments the code has been used to solve the equation for the *Mean Wave Directions* associated to a random gravity waves field using SWAN directional frequency variance spectra outputs.

The *Mean Wave Direction* at a given ocean location is defined as

$$\langle \theta \rangle = \arctan \left(\frac{\int_{-\infty}^{+\infty} \int_0^{+\infty} \sin \theta S(f, \theta) df d\theta}{\int_{-\infty}^{+\infty} \int_0^{+\infty} \cos \theta S(f, \theta) df d\theta} \right) \quad (3.41)$$

where $S(f, \theta)$ is the directional-frequency variance spectrum.

The validation of the results have been made comparing the calculated values with that ones provided as outputs from the same simulations by the SWAN model.

The *Composite Trapezoidal rule* is one of the many integration techniques developed to numerically approximate the integral of a limited mono-dimensional function. It is defined as

$$\int_a^b f(x) dx \approx \frac{H}{2} \sum_{k=0}^{m-1} (f(x_k) + f(x_{k+1})) = H \left(\frac{1}{2} f(x_0) + \sum_{k=1}^{m-1} f(x_k) + \frac{1}{2} f(x_m) \right) \quad (3.42)$$

where $H = (b - a)/m$ is the discretization step of the interval $[a, b]$ in $m + 1$ points (see [83] and [84] for a detailed review of the most important numerical integration techniques).

This integration technique is able to solve exactly the integral of first degree polinomial functions (see [83] and [84] for the demonstration).

In order to apply the *Composite Trapezoidal rule* to integrate a bi-dimensional function, it has to be noted that

$$\int_a^b \int_c^d f(x, y) dx dy = \int_a^b \left[\int_c^d f(x, y) dx dy \right] \quad (3.43)$$

$$\approx \int_a^b \sum_{j=0}^n \beta_j f(x, y_j) dx \quad (3.44)$$

$$\approx \sum_{i=0}^m \sum_{j=0}^n \alpha_i \beta_j f(x_i, y_j) \quad (3.45)$$

$$= Q_m Q_n f \quad (3.46)$$

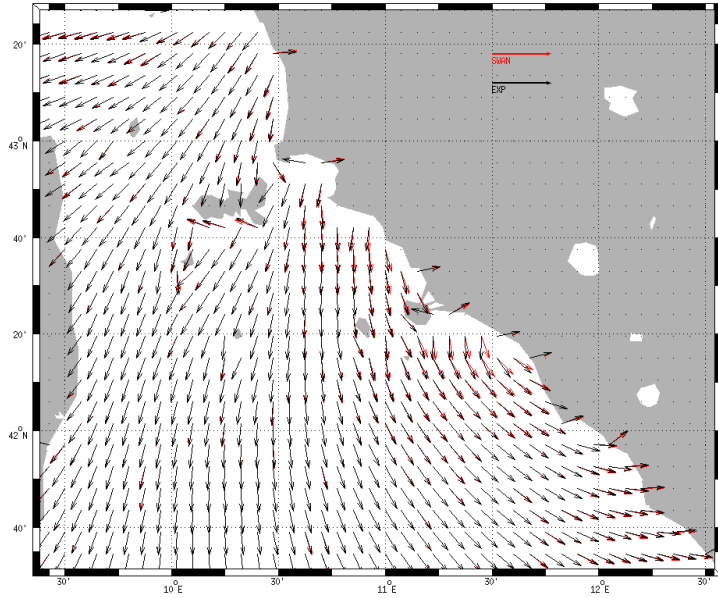
where $x \in [a, b]$, $y \in [c, d]$ and Q_m and Q_n are two arbitrary chosen mono-dimensional integration techniques with $m + 1$ and $n + 1$ discretization points,

respectively, and α_i , with $i = 0 \dots m$, and β_j , with $j = 0 \dots n$, weights, respectively [83] and [84].

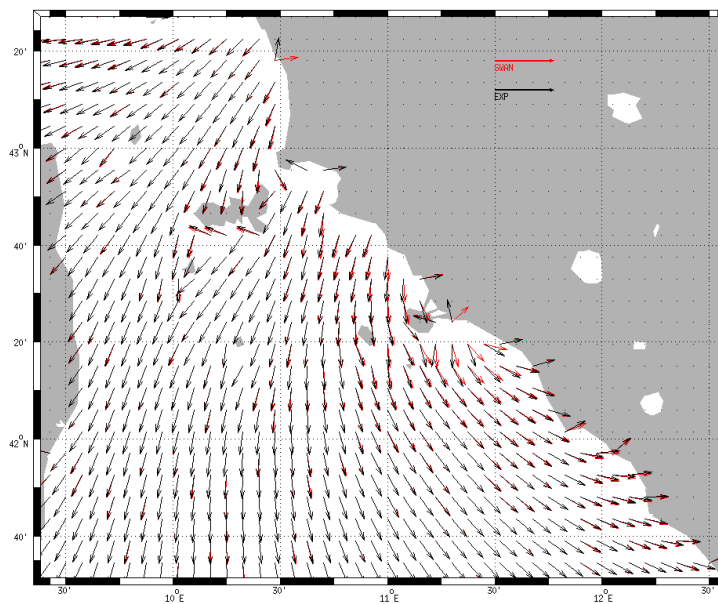
Therefore, to perform the double integration of a limited bi-dimensional function, it is needed to integrate before in a dimension and then in the other one.

In figure 3.29 the mean wave direction fields calculated by SWAN and by the routine are shown for two test cases.

The *Composite Trapezoidal rule* algorithm developed to perform the double integration of equation 3.41 reproduces the values of mean wave directions calculated by SWAN with a good approximation.



(a)



(b)

Fig. 3.29: (a) Mean wave directions sample field calculated on the 15-02-2012 at 10.30 by SWAN (in red) and by using the trapezoidal rule (in balck). (b) Mean wave directions sample field calculated on the 15-02-2012 at 03.00 by SWAN (in red) and by using the trapezoidal rule (in balck). .

Stokes Drift Numerical Solutions: in this last set of experiments, in order to numerically solve the double integral in equation 3.33, the *Composite Rectangle Rule* has been implemented too.

Then, the *Trapezoidal* composite rule and the iterative algorithm for wave-number computation have been used to calculate the stokes drift velocity solving equations 3.36 and 3.32 (Stokes' Drift for general random gravity waves fields), while the *Rectangle* one has been applied to solve equations 2.47 and 3.33 for deep waters approximation.

Results have been compared with the mean wave directions calculated by SWAN, considering that the stokes drift direction is approximately equal to the mean wave direction.

The *Composite Rectangle rule* is the simplest integration technique developed to numerically approximate the integral of a limited mono-dimensional function. It is defined as [83] and [84]

$$\int_a^b f(x)dx \approx H \sum_{k=0}^{m-1} f(x_k) \quad (3.47)$$

where $H = (b - a)/m$ is the discretization step of the interval $[a, b]$ in $m + 1$ points (see [83] and [84]).

As the *Composite Trapezoidal rule*, this technique is able to solve exactly the integral of first degree polinomial functions (see [83] and [84] for the demonstration).

Also the *Composite Rectangle rule* has been implemented to solve bi-dimensional integrals.

Two sample results of the experiments are shown in figures 3.30 and 3.31.

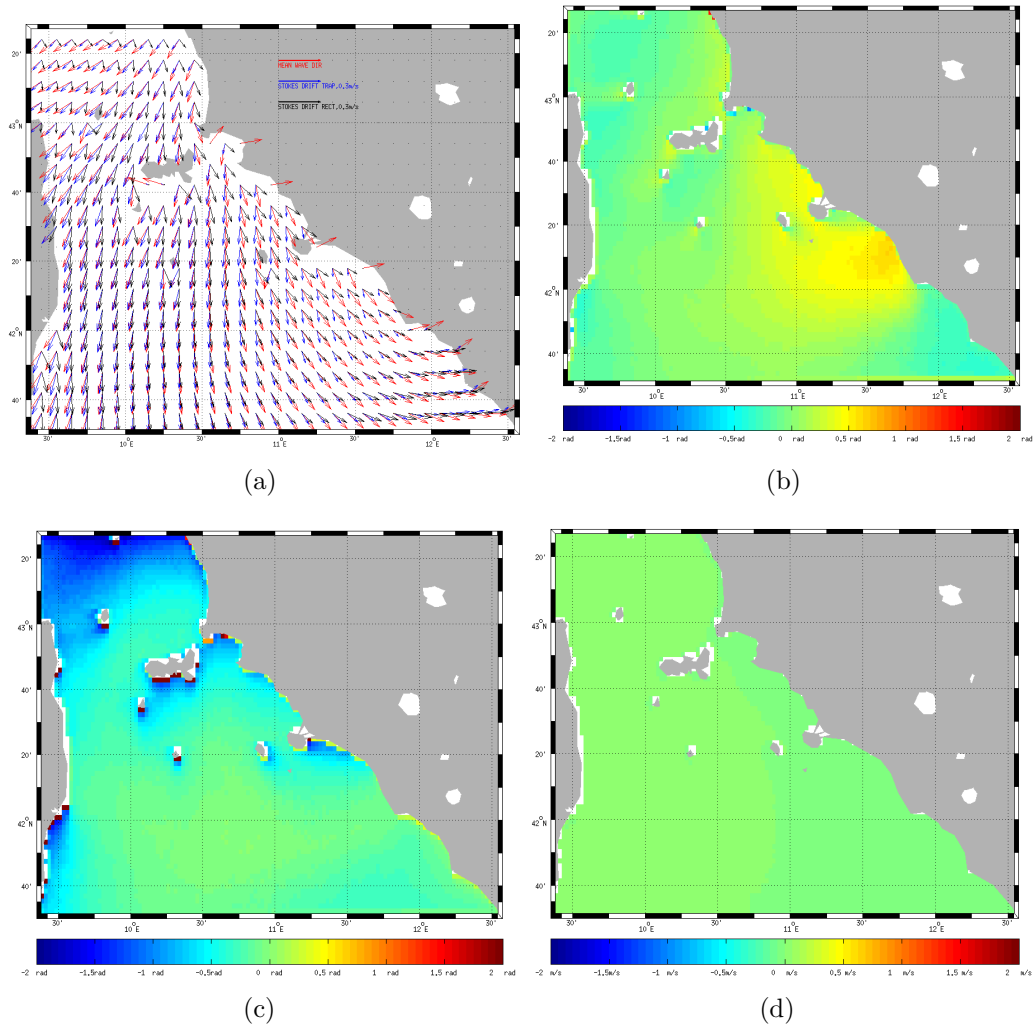


Fig. 3.30: (a) Example of Mean wave directions field computed by SWAN (in red) on 15-02-2012 at 01.00 and Stokes drift velocity fields calculated for the same date and time using the *Composite Trapezoidal rule* (in blue) and the *Composite Rectangle rule* (in black). (b) Differences between mean wave directions computed by SWAN and the direction of the Stokes drift velocity calculated using the *Composite Trapezoidal rule*. The direction of the Stokes drift velocity θ_S is calculated using the equation $\theta_S = \arctan(V_S/U_S)$, where U_S and V_S are, respectively, the zonal and meridional components of the Stokes drift velocity $\vec{U}_S = (U_S, V_S)$. (c) Differences between mean wave directions computed by SWAN and the direction of the Stokes drift velocity calculated using the *Composite Rectangle rule*. (d) Differences between the modulo of the Stokes drift velocity calculated using the *Composite Trapezoidal rule* and that one computed using the *Composite Rectangle rule*. The modulo of the Stokes drift vector $\vec{U}_S = (U_S, V_S)$ is given by $|\vec{U}_S| = \sqrt{U_S^2 + V_S^2}$

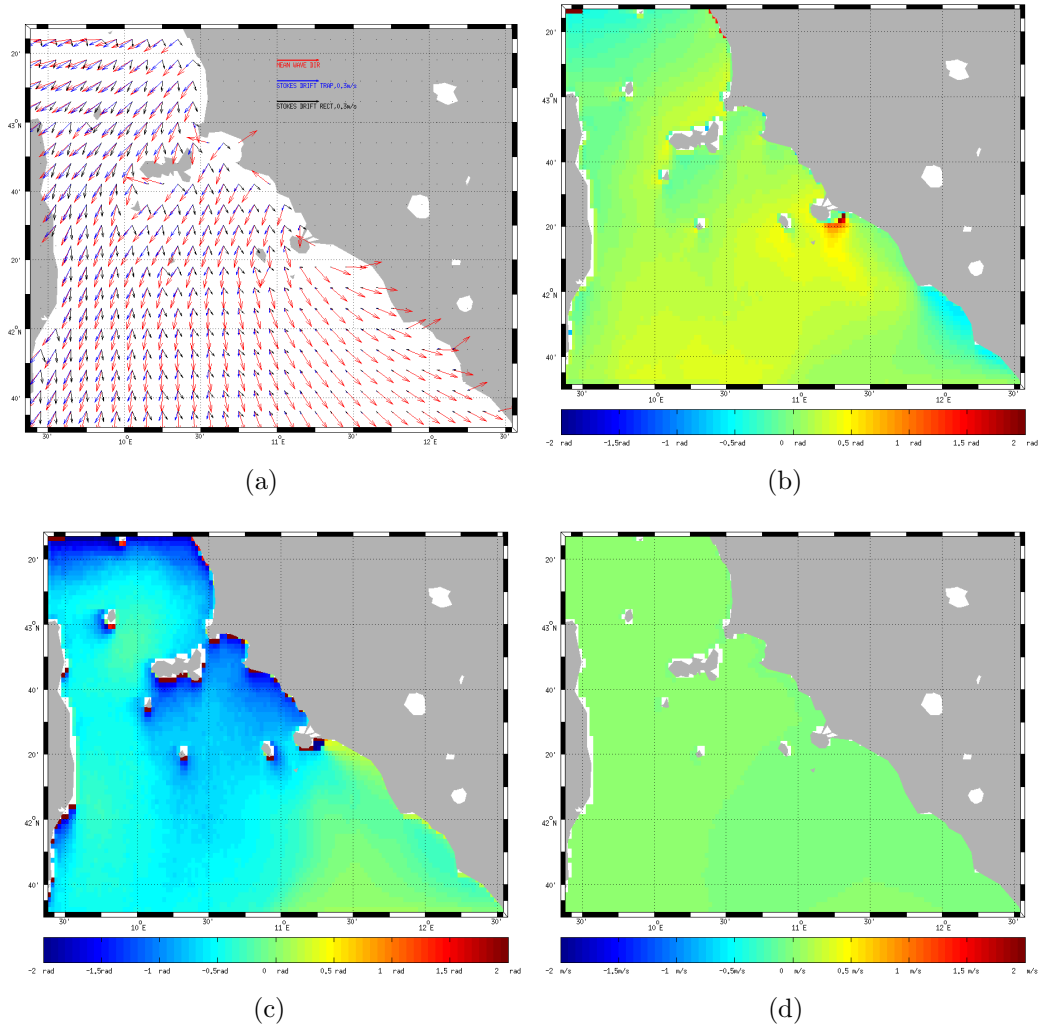


Fig. 3.31: (a) Example of Mean wave directions field computed by SWAN (in red) on 15-02-2012 at 12.30 and Stokes drift velocity fields calculated for the same date and time using the *Composite Trapezoidal rule* (in blue) and the *Composite Rectangle rule* (in black). (b) Differences between mean wave directions computed by SWAN and the direction of the Stokes drift velocity calculated using the *Composite Trapezoidal rule*. The direction of the Stokes drift velocity θ_S is calculated using the equation $\theta_S = \arctan(V_S/U_S)$, where U_S and V_S are, respectively, the zonal and meridional components of the Stokes drift velocity $\vec{U}_S = (U_S, V_S)$. (c) Differences between mean wave directions computed by SWAN and the direction of the Stokes drift velocity calculated using the *Composite Rectangle rule*. (d) Field of the differences between the modulo of the Stokes drift velocity calculated using the *Composite Trapezoidal rule* and that one computed using the *Composite Rectangle rule*. The modulo of the Stokes drift vector $\vec{U}_S = (U_S, V_S)$ is given by $|\vec{U}_S| = \sqrt{U_S^2 + V_S^2}$

Looking at the results, it is possible to say that the Stokes' Drift velocities computed by the *Composite Trapezoidal rule* are meanly in the same direction of the mean wave directions computed by SWAN, while that ones computed by using the *Composite Rectangle rule* significantly diverge from them. The module of the velocities computed with both the methods is almost the same. Therefore, in the next experiments, the *Composite Trapezoidal rule* has been used in order to solve equation 3.32.

3.3.3 SWAN-MEDSLI-II Coupling Experiments

In this section, the experiments performed to couple the oil-spill model *MEDSLIK-II* with the wind-wave model SWAN are described.

The coupling operation has been performed in order to force the MEDSLIK-II model with Stokes' Drift velocity fields calculated from the SWAN directional-frequency spectra outputs and the algorithms described in Section 3.3.2.

In order to validate the experiments, MEDSLIK-II has been used to simulate the trajectories of the four *I-SPHERE* drifters released south-eastward of the Giglio island during the Costa Concordia emergency.

The drifters are *oceanographic instruments* used to study the surface circulation and oceanographic dynamics. They are designed to be transported by ocean currents and these characteristics make them useful tools to validate hydrodynamic models [5] [44] [63] and oil spill/trajectory models [85] [81] [62].

Oil spill-following surface drifters (*i-SPHERE*) [81] are 39.5 cm diameter spheres designed on the basis of earlier experiments carried out in the late 1980s and early 1990s (see figure 3.32) [23].

The 4 drifters were released the 14 of February 2012 and recovered 24 hrs later.

As shown in figure 3.33, the buoys had a linear arrangement from north-east to southwest and an average distance of about 7 km between Giglio and Giannutri Island.



Fig. 3.32: Oil spill-following surface drifters *i-SPHERE*.)

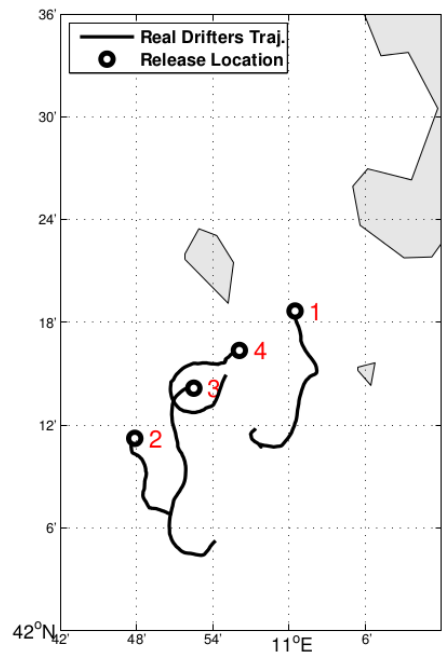


Fig. 3.33: Real drifters trajectories (black lines) from 14th February at 9:00 UTC to 15th February at 9:00 UTC (from [23]).

MEDSLIK-II has been forced using SURF-NEMO current fields. SURF has been implemented in the same area of the Tyrrhenian Sea chosen for the NEMO-SWAN coupling experiments (see Section 3.2.2), using the same computational features. Since the simulations results in Section 3.2.2 have demonstrated that the NEMO component of the SURF model, in this initial computational configuration, is insensitive to the spin-up time, for the experiments performed in this Section we have decided to use the NEMO spin-up time that requires less computational time (*spin-up time* 3 days).

A summary of the features of the computational domain of the SWAN and NEMO models implementation in the Costa Concordia area are given in tables 3.22 and 3.23.

The three models (NEMO, SWAN and MEDSLIK-II) have been forced with the high resolution SKIRON analysis atmospheric input fields, with a time resolution of one hour and a 0.025° horizontal resolution.

The MEDSLIK-II trajectory simulations were performed using the currents, the Stokes drift and the wind drag, indicated as U_C , U_S and U_D , respectively, in equation 3.28.

The turbulent diffusion $d\vec{x}'_k(t)$ of equation 3.28 has been parameterized using the diffusivity coefficients in equation 3.18 set to zero.

The parameter γ of equation 3.17 for U_D has been set equal to 0.01, thus, U_D was about 1% of the wind velocity.

The MEDSLIK-II code has been modified in order to read Stokes drift velocity fields calculated from a spectral wave model output as described in Section 3.3.2. Therefore, in the configuration developed in this Thesis, MEDSLIK-II can calculate the Stokes' drift velocity using parameterized JONSWAP wave spectra (equation 3.33) or using the SWAN wave spectra.

In table 3.28, a summary of the computational features of the MEDSLIK-II model used in these experiments is given.

Table 3.28: MEDSLIK-II computational setting used in coupling experiments.

Parameter	Configuration/Value
General features	
Simulation mode	trajectories simulation
Drifter simulated	4
Area of drifter released	Costa Concordia accident area
Time Parameters	
Computational time step Δt	1800 s
Output frequency Δt	1800 s
Advective Terms	
U_C	provided as input
U_S	by using JONSWAP parameterization or algorithm developed in this Thesis
U_D	calculated with $\gamma = 0.01$
Turbulent Diffusion	
K_h	0
K_v	0
Forcing Input Data	
Wind forcing data	<i>SKIRON</i>
Current forcing data	<i>SURF</i>
Stokes drift forcing data	JONSWAP parametric spectra or SWAN wave energy spectra

Table 3.28: MEDSLIK-II computational setting used in coupling experiments.

Two experiments have been performed and they are organized as follows.

- **In the first**, SURF-NEMO has been used to simulate current fields for the period between 11-02-2012 at 00.00 and 15-02-2012 at 00.00 (*spin-up time* of 3 days). Then, SURF-SWAN has been used to simulate wind-wave fields for the period between 14-02-2012 at 00.00 and 15-02-2012 at 00.00. After that, SURF-SWAN Directional-frequency spectra outputs have been provided to the Stokes Drift calculation algorithm developed in this Thesis. Finally, the Stokes' Drift velocity fields computed and the SURF-NEMO current fields have been provided to MEDSLIK-II which has been used to simulate the trajectories of the four drifters released during the Costa Concordia accident.

- **In the second**, SURF-NEMO has been used to simulate current fields for the period between 11-02-2012 at 00.00 and 15-02-2012 at 00.00 (*spin-up time* of 3 days). Then, MEDSLIK-II used the SKIRON winds to calculate the Stokes' Drift using the JONSWAP parameterization (MEDSLIK-II original algorithm).

A summary of the configuration of the two coupling experiments is shown in table 3.29.

Table 3.29: Description of the two numerical experiments performed to test SURF-SWAN-MEDSLIK-II coupling.

Exp Number	SURF-NEMO spin-up	Stokes Drift Computation	MEDSLIK-II simulation
Exp. 7.1	3 days	by using SURF-SWAN wave energy spectra	4 drifters trajectories
Exp. 7.2	3 days	by using JONSWAP parameterized spectra	4 drifters trajectories

Two metrics have been used to objectively evaluate the accuracy of the Lagrangian trajectory simulations.

The first is the the *separation distance* d_i between the observed and the simulated trajectories as a function of the simulation time:

$$d_i(x_s(t_i), x_o(t_i))$$

where d_i is the distance at the selected time t_i , after a reference time t_0 , between the simulated drifter position, x_s , and the observed positions, x_o . The acceptable maximum separation between observed and modeled trajectory depends on the particular model application. Generally, an error lower than 20 km would allow the use of the model forecasts in situations of rapid response, such as oil spills and search and rescue operations [24]. Generally, taking a quite conservative limit, it can be considered acceptable a spatial error of the simulated trajectories of the order of three-four times the horizontal resolution of the Eulerian ocean currents used to force the model [24].

The second metric is the *Liu and Weisberg* skill score [63]. It is defined as an average of the separation distances weighted by the lengths of the observed trajectories:

$$s(t_i) = \frac{\sum_{t=0}^{t_i} d_i(x_s(t), x_o(t))}{\sum_{t=0}^{t_i} l_{oi}(x_o(t_0), x_o(t))} \quad (3.48)$$

where l_{oi} is the length of the observed trajectory at the corresponding time, t_i , after a reference time t_0 . The s index can be used to define a model skill score:

$$ss(t_i) = \begin{cases} \frac{1-s(t_i)}{n} & (s \leq n) \\ 0 & (s > n) \end{cases} \quad (3.49)$$

where n is a tolerance threshold. In this work, as suggested by *Liu and Weisberg* [63], we used $n = 1$. It corresponds to a criterion that cumulative separation distance should not be larger than the associated cumulative length of the drifter trajectory. The higher the ss value, the better the performance, with $ss = 1$ implying a perfect fit between observation and simulation and with $ss = 0$ indicating the model simulations have no skill. This skill score may have some limitations in case of very weak currents and hence small cumulative distances, that may imply a very large value of s and very low skill score ss . These limitations may be overcome by setting a proper tolerance threshold, n , as suggested by *Liu and Weisberg* [63].

Figure 3.34 shows the real tracks (black lines) of the four drifters released (a, b, c, and d, respectively) and the simulated MEDSLIK-II trajectories for the two experiments of table 3.29.

Considering the drifters 1, 2, and 3, both the simulated trajectories by using JONSWAP parametric frequency energy spectra and SURF-SWAN directional-frequency output variance spectra have the correct direction respect to the real ones. For the drifter 4 this is not true. Furthermore, all the simulated drifters are much too slow as compared to reality.

The latter can be reasonably attributed to a low accuracy of the SURF-NEMO current fields, remembering that current velocity magnitude can be generally considered of the first order, while Stokes Drift is a second order effect.

Indeed, from the comparison with the MEDSLIK-II trajectories calculating by using the currents provided by the relocatable model IRENOM (Interactive RElocatable Nested Ocean Model, described in *De Dominicis et al.*

[23] and presented in figure 3.34), it is clear that the SURF-NEMO current velocities are responsible for the lower path traveled by the simulated drifter.

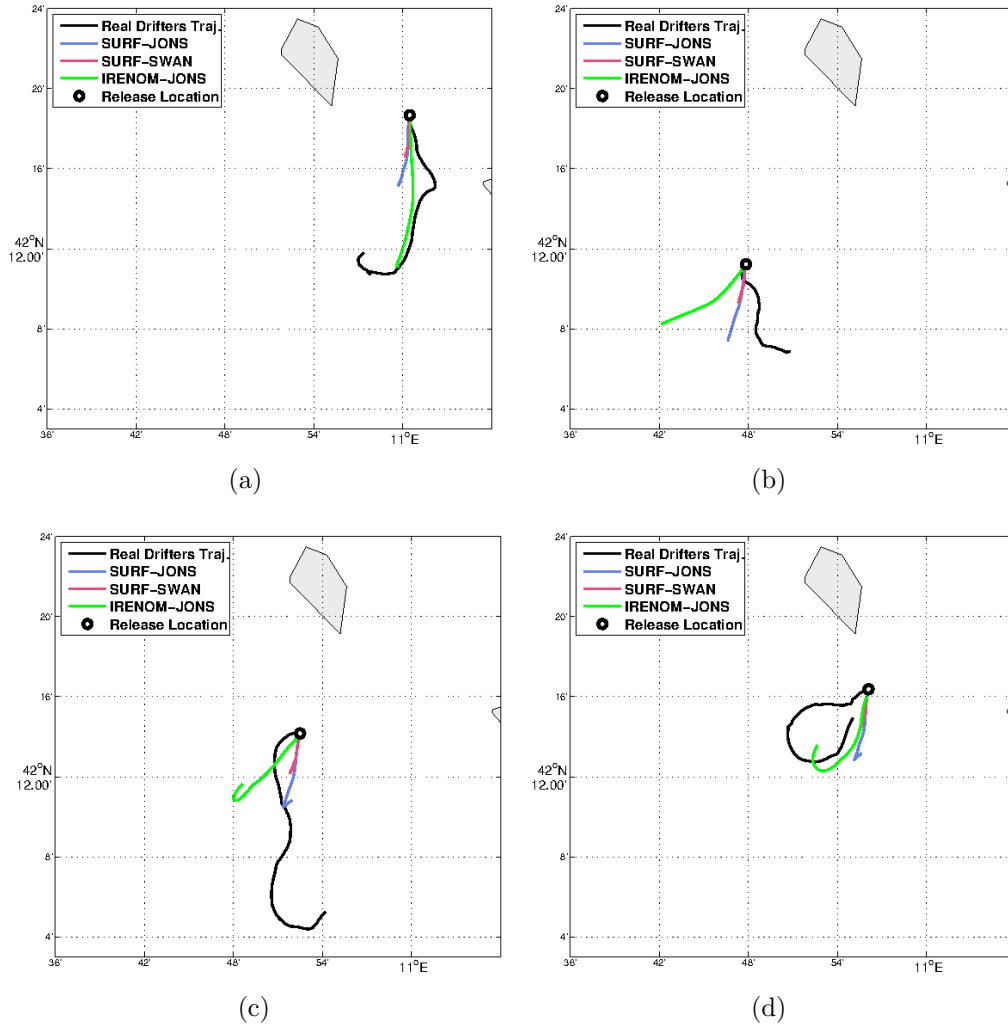


Fig. 3.34: Real drifters trajectories (black lines) from 14th February at 9:00 UTC to 15th February at 9:00 UTC and simulated MEDSLIK-II trajectories using JONSWAP parametric spectra and SURF-NEMO currents (blu line), SURF-SWAN directional-frequency variance output spectra and SURF-NEMO currents (red line) or JONSWAP parametric spectra and IRENOM currents (green line). (a) Drifter 1. (b) Drifter 2. (c) Drifter 3. (d) Drifter 4.

The low accuracy of SURF-NEMO current fields can be reasonably justified by the closed lateral boundary condition used in this work. In addition, it has to be considered that the *Giannutri* island is not represented in the SURF-NEMO computational domain, while in the IRENOM implementation of *De Dominicis et al.* [23] experiments it was, and therefore the intensified current flow stream demonstrated in [23] can not be calculated by SURF.

Focusing on the Stokes' Drift computations, the results show that the Stokes Drift velocities calculated from the SURF-SWAN directional-frequency output spectra are slower of than the ones computed by using JONSWAP parametric frequency spectra and MEDSLIK-II. This is confirmed by figures 3.35, 3.36 and 3.37.

In figure 3.35 the module, as a function of the simulation time, of the Stokes Drift velocities derived by using SURF-SWAN output spectra (in red) are compared to the ones obtained by using JONSWAP spectra (in blue), for the four drifters.

Figures 3.36 and 3.37 show the *Separation Distance* and the *Skill Score* ss , as a function of the simulation time, calculated for the simulations performed by using JONSWAP spectra (in blu) and SWAN output spectra (in red). The best results for both the *Separation Distance* and the *Skill Score* are obtained using the JONSWAP spectra (in blu). This is a consequence of the fact that the Stokes Drift velocities calculated from the SURF-SWAN directional-frequency output spectra are slower than the one computed by using the JONSWAP spectra.

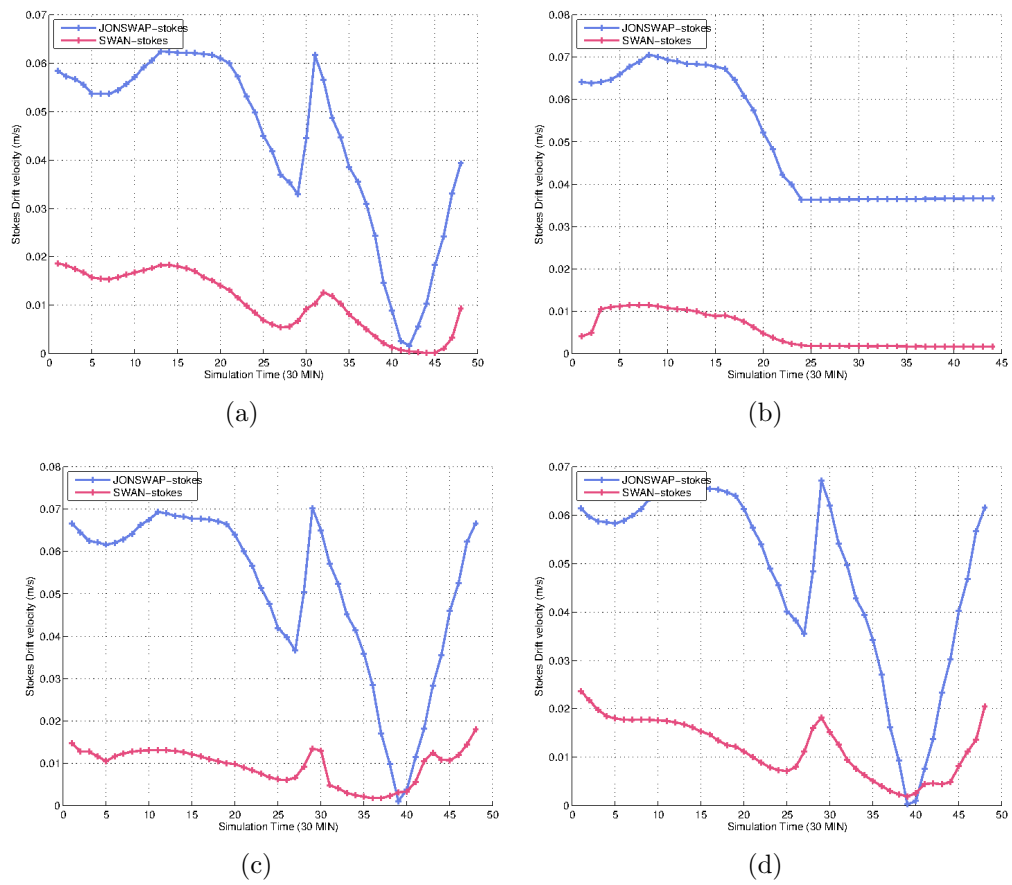


Fig. 3.35: Module of the Stokes Drift velocities, as a function of the simulation time, from 14th February at 9:00 UTC to 15th February at 9:00 UTC by using SURF-SWAN directional-frequency output spectra (red lines) and by using JONSWAP parametric frequency spectra (blu lines). (a) Drifter 1. (b) Drifter 2. (c) Drifter 3. (d) Drifter 4.

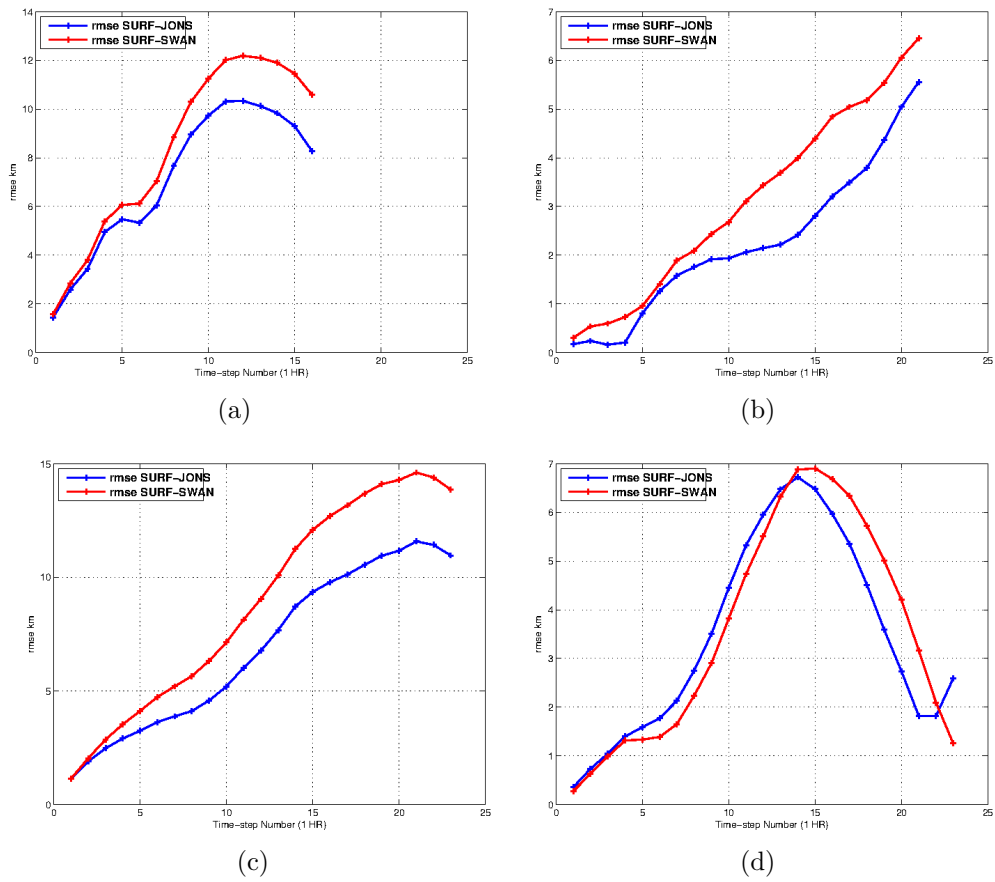


Fig. 3.36: Real drifters trajectories (black lines) from 14th February at 9:00 UTC to 15th February at 9:00 UTC and simulated MEDSLIK-II trajectories using JONSWAP parametric spectra (blu lines) or SURF-SWAN directional-frequency varinace output spectra (red lines). (a) Drifter 1. (b) Drifter 2. (c) Drifter 3. (d) Drifter 4.

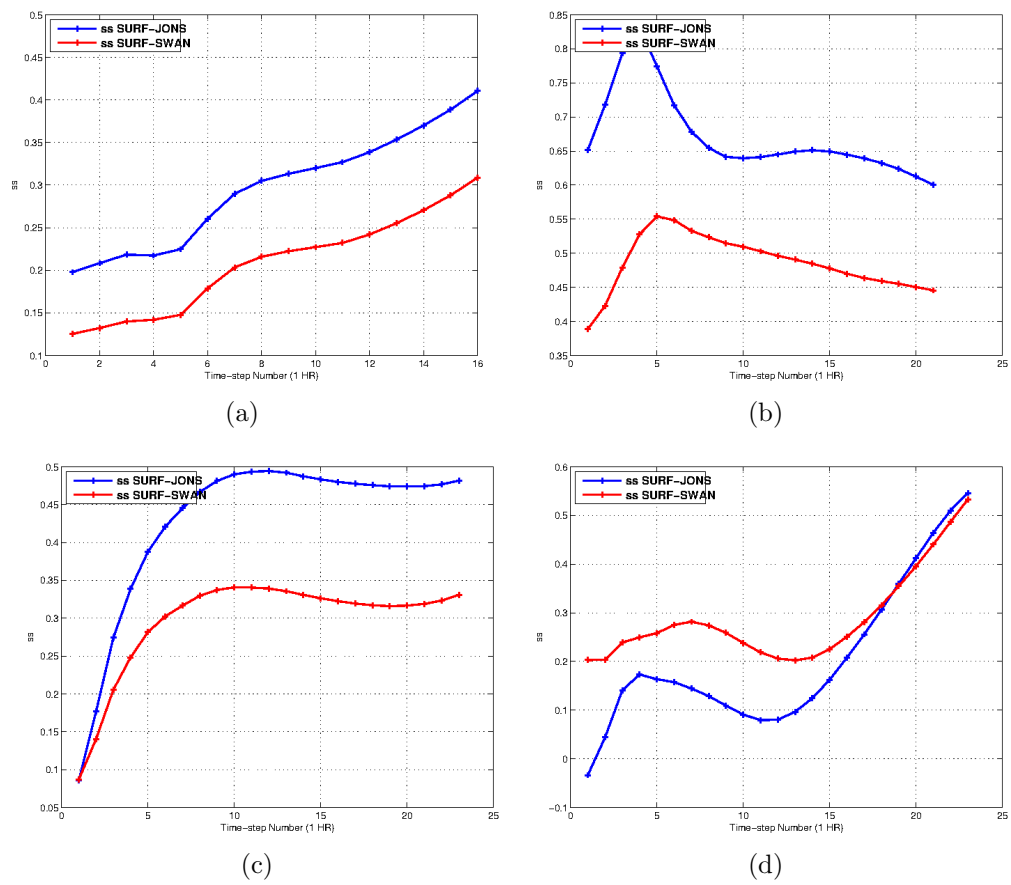


Fig. 3.37: Real drifters trajectories (black lines) from 14th February at 9:00 UTC to 15th February at 9:00 UTC and simulated MEDSLIK-II trajectories using JONSWAP parametric spectra (blu lines) or SURF-SWAN directional-frequency varinace output spectra (red lines). (a) Drifter 1. (b) Drifter 2. (c) Drifter 3. (d) Drifter 4.

The significant differences between the velocity module of the two methods can be explained considering that the JONSWAP frequency spectrum is a parameterization, which means that its shape and values are computed from the local wind fields by using empirical statistical formulas (see Section 2.2.3 for the JONSWAP spectra definition). These formulas make no attempt to separate the physical processes involved in wave growth and energy dissipation. They represent net wave growth from known properties of the wind field (wind speed and direction, fetch and duration) [77] but they do not consider, for example, the depth. Since wave growth is affected by the depth, with additional dissipative processes in play, the deep water curves like the JONSWAP one will over-estimate the wave growth in shallow water [77]. In addition, it has been fully demonstrated and accepted by the scientific community (see, for example, [41] [47] [38]) that parametric spectra as JONSWAP and Pierson-Moskowitz are not able to properly represent wave spectra developed under rapidly wind variations, overestimating always the real ones.

This conclusion is supported by figure 3.38, where the *Significant Wave Heights* computed by SURF-SWAN for the coordinates that describe the trajectory of the first drifter is compared to the ones computed by MEDSLIK-II using JOSWAP parameterization.

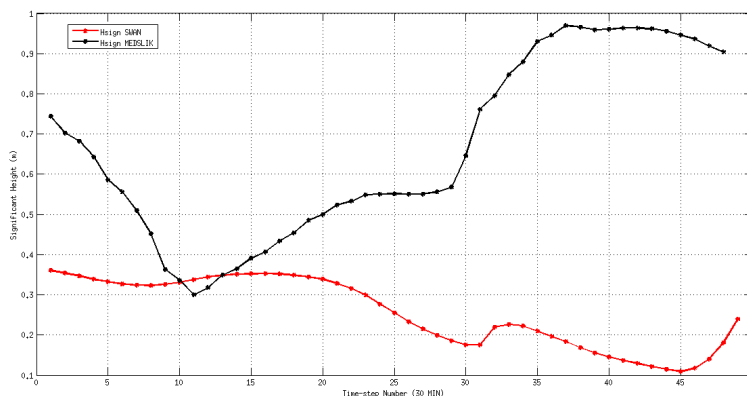


Fig. 3.38: Significant Wave Height, as a function of the time step and the trajectory coordinates of the drifter 1, computed by MEDSLIK-II and SWAN.

Therefore, it is possible to conclude that the Stokes Drift velocities calculated by using the JONSWAP parametric spectra already implemented in MEDSLIK-II are higher than the ones calculated by using SWAN directional frequency output spectra due to the JONSWAP spectra overestimation.

In order to support this conclusion, two more experiments have been per-

formed for the period between 14-02-2012 at 00.00 and 16-02-2012 at 00.00.

The purpose of these experiments was to compare the *Significant Wave Height* measured by the ISPRA buoy located at Civitavecchia with the ones calculated by using the JONSWAP parameterization and the SWAN wave energy spectra.

In the first one, the significant wave height has been computed using the JONSWAP spectrum parameterization implemented in MEDSLIK-II.

In the second, the same has been done by using SURF-SWAN directional frequency spectra.

Results are shown in figure 3.39.

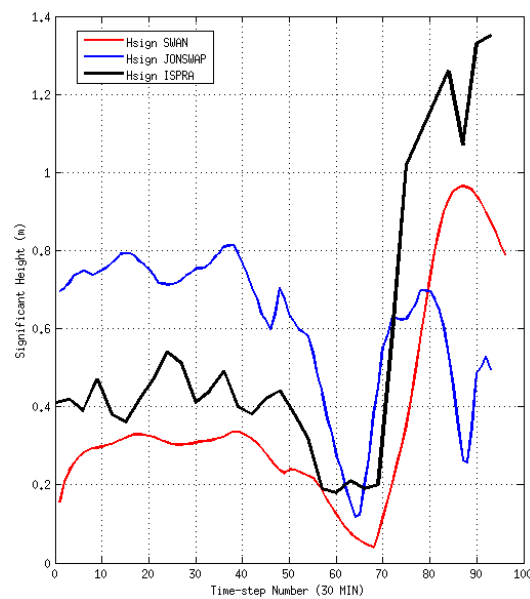


Fig. 3.39: Significant Wave Heights timeseries for the period between 14-02-2012 at 00.00 and 16-02-2012 at 00.00 sampled by the ISPRA buoy located at Civitavecchia offshore waters and computed by SURF-SWAN and MEDSLIK-II for the same location.

As figure 3.39 demonstrates, the *Significant Wave Heights* computed by MEDSLIK-II are significantly meanly higher than the ones computed by SWAN, confirming the general overestimation of the JONSWAP wave spectra respect to real ones.

Chapter 4

Conclusions

The blowing of the wind on the sea surface generates ocean currents due to turbulent stress and ocean waves, which give rise to wave-induced velocities that are known as Stokes' Drift velocities. The Stokes' Drift transport associated to a random gravity wave field is a function of the wave Energy Spectra that statistically fully describe it.

Therefore, in order to perform an accurate numerical simulation of the oil motion in seawater, a coupling of the oil-spill model with a wave and turbulence current forecasting model is needed. In this Thesis work, the coupling of the SWAN wind-wave model with MEDSLIK-II oil-spill numerical model and NEMO relocatable model has been performed and tested.

First, in order to improve the knowledge about the wind-wave model and its numerical performances, a preliminary sensitivity study of the SWAN model has been carried out. The Significant Wave Height and the Peak period simulated by the SWAN model for the period between 14-02-2012 at 00.00 and 16-02-2012 at 00.00 have been compared with that ones sampled for the same period by the ISPRA directional buoys located at Venezia, Ancona and Monopoli.

The experiments performed to test the sensitivity of the SWAN numerical model to atmospheric and currents input fields have demonstrated the great influence that the resolution of the wind forcing fields and the accuracy of the current fields have on the quality of the wave model simulations.

Numerical tests done to investigate the SWAN sensitivity to computational time-step variations (60, 600 and 1800 seconds) have showed that the SWAN numerical model seems to be quiet insensitive to this numerical parameter. This can be justified by the many parameterizations that are used to represent the physical processes involved in waves generation in the SWAN model code. Thus, not using some kind of time evolving equations reduces the sensitivity of the model results to time step variations. Furthermore, it has to be noted that the SWAN insensitivity to computational time-step changes can be also due to the too coarse computational grid used in this group of experiments, which can not be able to represent small scale gradient of quantities involved in waves generation reducing sensibly their changes in time.

Experiments performed to test wave refraction (through the *c-theta* parameter set equal to 0.5) have demonstrated that the computational grid with horizontal resolution approximately equal to 2.2 km used in sensitivity experiments was resolute enough to properly represent the wave refraction.

The last sensitivity experiments have been performed in order to test and find the best physical setting able to properly simulate the environmental dynamics characterizing the Adriatic Sea domain. Results have showed that the best combination for the *Exponential Wave Growth* and *White-Capping energy dissipation* parameterizations is that one for which the empirical formulations by Komen et al. [59] are used. The best parameterization of the *Bottom Friction* physical process is the one from Collins [19]. In addition, results have showed that the model is insensitive to the using or not of the *Non-Linear Triads*, which means that, in our model configuration, the resolution of the spatial computational grid used is too coarse to properly represent the near-coastal processes.

Next, using the best SWAN model configuration detected, the coupling between SWAN and NEMO within the SURF relocatable ocean model has been performed and tested.

SWAN-NEMO coupling experiments results have showed that the SURF-SWAN simulations are insensitive to SURF-NEMO current fields obtained with different spin-up times. This can be justified by the small differences in the SURF-NEMO current fields and by the fact that in this initial step the SURF relocatable model has been developed by using closed lateral boundary conditions in SURF-NEMO computations.

In order to show the benefit of using SWAN to compute the Stokes' Drift velocity fields we have developed the computation of the Stokes' Drift from SWAN model output. The Newton's iterative method has been implemented in order solve the general dispersion relation for surface gravity waves for the wave-number K . Results have showed that, at the second order of accuracy, the algorithm developed exactly reproduces the wave-number values given by *Goda* [34].

In addition, both the trapezoidal and the rectangle rules have been implemented to calculate the stokes drift velocity given by equations 3.32 and 3.33. Results have been compared with the mean directions calculated by SWAN, considering that the stokes drift direction is approximately equal to the mean wave direction and the *Composite Trapezoidal rule* has showed the best results.

Finally, the coupling of the oil-spill model *MEDSLIK-II* with the wind-wave model SWAN has been performed in order to force the MEDSLIK-II model with Stokes' Drift velocity fields calculated from the SWAN directional-frequency spectra outputs.

In SWAN-MEDSLIK-II coupling experiments, the trajectories of four drifters have been simulated by using JONSWAP parametric spectra or SWAN output spectra and results have been compared with the real paths traveled by the drifters. Results showed that the Stokes Drift velocities calculated from the SWAN directional-frequency output spectra by using the algorithm developed in this Thesis are slower of than computed by using JONSWAP parametric frequency spectra and MEDSLIK-II. The significant differences between the velocity module of the two methods can be explained considering that the JONSWAP frequency spectrum is a parameterization. This means that its shape is computed by using empirical statistical formulas which make no attempt to separate the physical processes involved in wave growth and energy dissipation but represent net wave growth from known properties of the wind field (wind speed and direction, fetch and duration). It has been fully demonstrated and accepted by the scientific community that parametric spectra as JONSWAP and Pierson-Moskowitz are not able to properly represent wave spectra developed under rapidly wind variations, overestimating always the real ones and our experiments have demonstrated this overestimation.

The lower accuracy of MEDSLIK-II simulated trajectories obtained by using SWAN directional-frequency output spectra can be justified by considering

that, in this work, the SWAN model has not been nested in a coarser wave model and, therefore, the swell, which is a fundamental component of wave energy spectra, has not been considered. In addition, nowadays, according to [98], third generation wave models are able to properly simulate integral wave parameters but the accuracy of the one- and bi-dimensional wave energy spectra simulated is still much low.

Therefore, this work is a first fundamental attempt to solve the problem linked to the Stokes' Drift by using wind wave models which can improve the accuracy of its computation, but much work has still to be done.

Future improvements can be the nesting of the SWAN model in a coarser wind-wave model in order to consider the swell component and the development of some different numerical schemes able to solve with more accuracy the computation of the Stokes' Drift from wave energy spectra.

Bibliography

- [1] Y. Agnon and A. Sheremet. Stochastic evolution models for nonlinear gravity waves over uneven topography. *Advances in Coastal and Ocean Engineering*, 6:103–133, 2000.
- [2] J.H.G.M. Alves and M. L. Banner. Performance of a saturation-based dissipation-rate source term in modelling the fetch-limited evolution of wind waves. *Journal of Physical Oceanography*, 33:1274–1298, 2003.
- [3] U. C. Bandara and P. D. Yapa. Bubble sizes, breakup, and coalescence in deepwater gas/oil plumes. *Journal of Hydraulic Engineering, ASCE*, 137, No. 7:729–738, 2011.
- [4] U. C. Bandara, P. D. Yapa, and H. Xie. Fate and transport of oil in sediment laden marine waters. *Journal of Hydro-Environment Research, Elsevier*, Vol. 5:145–156, 2011.
- [5] C. N. Barron, L. F. Smedstad, J. M. Dastugue, and O. M. Smedstad. Evaluation of ocean models using observed and simulated drifter trajectories: Impact of sea surface height on synthetic profiles for data assimilation. *J. Geophys. Research*, 112, 2007.
- [6] J.A. Battjes and J.P.F.M. Janssen. Energy loss and set-up due to breaking of random waves. *Proc. 16th Int. Conf. Coastal Engineering, ASCE*:569–587, 1978.
- [7] S.E. Belcher and J.C.R. Hunt. Turbulent shear flow over slowly moving waves. *Journal of Fluid Mechanics*, 251:109–148, 1993.
- [8] L. Bertotti and L. Cavaleri. Wind and wave predictions in the adriatic sea. *Journal of Marine Systems*, 78:227–234, 2009.
- [9] K. Blair and J. J. Schule. Wind waves: Their generation and propagation on the ocean surface. *Science*, 150:737–738, 1999.

- [10] N. Booij, R. C. Ris, and L. H. Holthuijsen. A third-generation wave model for coastal regions - 1. model description and validation. *Journal of Geophysical Research*, 104:7649–7666, 1999.
- [11] E. Bouws and G.J. Komen. On the balance between growth and dissipation in an extreme, depth-limited wind-sea in the southern north sea. *J. Phys. Oceanogr.*, 13:1653–1658, 1983.
- [12] D. Bruciaferri, S. Falchetti, F. Trotta, L. Giacomelli, and M. Zavatarelli. Report on the characteristics of the relocatable wind-wave model swan. *Progetto Tessa, Attivita' 1.3*, Dipartimento di Fisica e Astronomia dell'Universita' di Bologna, Laboratorio SINCEM, via S.Alberto 163, 48100 Ravenna, 01-07-2013.
- [13] P. Carracedo, S. Torres-Lopez, M. Barreiro, P. Montero, C. F. Balseiro, E. Penabad, P.C. Leitao, and V. Perez-Munuzuri. Improvement of pollutant drift forecast system applied to the prestige oil spills in galicia coast (nw of spain): Development of an operational system. *Mar. Pollut. Bullet.*, 53(5):350–360, 2006.
- [14] S. Castanedo, R. Medina, I. J. Losada, C. Vidal, F. J. Mndez, A. Osorio, J.A. Juanes, and A. Puente. The prestige oil spill in cantabria (bay of biscay). part i: operational forecasting system for quick response, risk assessment, and protection of natural resources. *Journal of Coastal Research*, pages 1474–1489, 2006.
- [15] L. Cavaleri, P.L De Filippi, G.F Grancini, G.L Ioveniti, and R. Tosi. Extreme wave conditions in the tyrrhenian sea. *Ocean Engng*, 13(2):157–180, 1986.
- [16] L. Cavaleri and P. Malanotte Rizzoli. Wind wave prediction in shallow water: Theory and applications. *Journal of Geophysical Research: Oceans*, 86:10961–10973, 1981.
- [17] X. Chao, N. J. Shankar, and S. S. Y. Wang. Development and application of oil spill model for singapore coastal waters, journal of hydraulic engineering. *Journal of Hydraulic Engineering, ASCE*, 129(7):495–503, 2003.
- [18] E. Clementi, P. Oddo, G. Korres, M. Drudi, and N. Pinardi. Coupled wave-ocean modelling system in the mediterranean sea. *13th International Workshop on Wave Hindcasting and 4th Coastal Hazards Symposium*, Alberta, Canada, 2013.

- [19] J.I. Collins. Prediction of shallow water spectra. *J. Geophys. Res.*, 77, 15:2693–2707, 1972.
- [20] G. Coppini, M. De Dominicis, G. Zodiatis, R. Lardner, N. Pinardi, R. Santoleri, S. Colella, F. Bignami, D. R. Hayes, D. Soloviev, G. Georgiou, and G. Kallos. Hindcast of oil-spill pollution during the lebanon crisis in the eastern mediterranean, julyaugust 2006. *Mar. Pollut. Bulletin.*, 62(1):140–153, 2011.
- [21] Working Group 3 COST 714. Measuring and analysing the directional spectrum of ocean waves.
- [22] P. Daniel, P. Josse, P. Dandin, V. Gouriou, M. Marchand, and C. Tiercelin. Forecasting the erika oil spills. *International Oil Spill Conference*, 2001, No.1:649–655, American Petroleum Institute, 2001.
- [23] M. De Dominicis, S. Falchetti, F. Trotta, N. Pinardi, L. Giacomelli, E. Napolitano, L. Fazioli, R. Sorgente, P. Haley, P. Lermusiaux, F. Martins, and M. Cocco. A relocatable ocean model in support of environmental emergencies - the costa concordia emergency case. *Geosciences Model Development*, in press.
- [24] M. De Dominicis, N. Pinardi, G. Zodiatis, and R. Archetti. Medslik-ii, a lagrangian marine surface oil spill model for short-term forecasting - part 2: Numerical simulations and validations. *Geosciences Model Development*, 6:1871–1888, 2013.
- [25] M. De Dominicis, N. Pinardi, G. Zodiatis, and R. Lardner. Medslik-ii, a lagrangian marine surface oil spill model for short-term forecasting - part 1: Theory. *Geosciences Model Development*, 6:1851–1869, 2013.
- [26] R. G. Dean and R. A. Dalrymple. *Water Wave Mechanics for Engineers and Scientists*. World Scientific Publishing Company Co. Pte. Ltd, 1991.
- [27] G.A.L. Delvigne and C.E. Sweeney. Natural dispersion of oil. *Oil and Chemical Pollution*, 4:281–310, 1988.
- [28] S. Dobricic and N. Pinardi. An oceanographic three-dimensional variational data assimilation scheme. *Ocean Modelling*, 22(3):89–105, 2008.
- [29] Y. Eldeberky. Nonlinear transformation of wave spectra in the nearshore zone. *Ph.D. thesis*, Delft University of Technology:Department of Civil Engineering, 1996.

- [30] Y. Eldeberky and J.A. Battjes. Parameterization of triad interactions in wave energy models. *Proc. Coastal Dynamics Conf. 1995*, Gdansk, Poland:140–148, 1995.
- [31] A.L. Fabrikant. Quasilinear theory of wind-wave generation. *Atmospheric and Oceanic Physics*, 12:524–526, 1976.
- [32] M. Fingas and B. Fieldhouse. Review water-in-oil emulsions: energy and work threshold as a function of temperature. *24th Arctic Marine Oilspill Program Technical Seminar*, pages Edmonton, Alberta, Environment Canada, 2006, 2006.
- [33] M.H. Freilich and R.T. Guza. Nonlinear effects on shoaling surface gravity waves. *Philosophical Transactions of the Royal Society of London*, 311:1–41, 1984.
- [34] Y. Goda. *Random Seas and Design of Maritime Structures - 3rd Ed.* World Scientific Publishing Company, 2010.
- [35] WAMDI group. The wam model – a third generation ocean wave prediction model. *J. Phys. Oceanogr.*, 18:1775–1810, 1988.
- [36] A. Guarnieri, N. Pinardi, P. Oddo, G. Bartoluzzi, and M. Ravaioli. Modelling baroclinic circulation with tidal components in the adriatic sea. *J. Geophys. Res. - Oceans*, 118:166–183, 2013.
- [37] E.R. Gundlach. Oil-holding capacities and removal coefficients for different shoreline types to computer simulate spills in coastal waters. *Proceedings of 1987 Oil Spill Conference*, pages 451–457, 1987.
- [38] H. Günther, W. Rosenthal, and K. Richter. Parametrical numerical wave prediction tested in wind situations varying in space and time. In A. Favre and Klaus Hasselmann, editors, *Turbulent Fluxes Through the Sea Surface, Wave Dynamics, and Prediction*, pages 607–616. Springer US, 1978.
- [39] K. Hasselmann. On the non-linear energy transfer in a gravity-wave spectrum. part 1. general theory. *Journal of Fluid Mechanics*, 12:481–500, 1962.
- [40] K. Hasselmann. On the spectral dissipation of ocean waves due to whitecapping. *Bound.-layer Meteor.*, 6:107–127, 1982.

- [41] K. Hasselmann, T.P. Barnett, E. Bouws, H. Carlson, D.E. Cartwright, K. Enke, J.A. Ewing, H. Giannap, D.E. Hasselmann, P. Kruseman, A. Meerburg, P. Muller, D.J. Olbers, K. Richter, W. Sell, and H. Walden. Measurements of windâ€šwave growth and swell decay during the joint north sea wave project (jonswap). *Dtsch. Hydrogr. Z. Suppl.*, 12:A8, 1973.
- [42] S. Hasselmann, K. Hasselmann, J.H. Allender, and T.P. Barnett. Computations and parameterizations of the nonlinear energy transfer in a gravity wave spectrum. part ii: Parameterizations of the nonlinear transfer for application in wave models. *J. Phys. Oceanogr.*, 15, 11:1378–1391, 1985.
- [43] L. Holthuijsen. *Waves in Oceanic and Coastal Waters*. Cambridge University Press, 2007.
- [44] H. S. Huntley, B. L. Lipphardt Jr, and A. D. Kirwan Jr. Lagrangian predictability assessed in the east china sea. *Ocean Modelling*, 36, 1,:163–178, 2011.
- [45] Z. I. Janjic. Nonlinear advection schemes and energy cascade on semi-staggered grids. *Mon. Weather Rev.*, 112, 1984.
- [46] P. Janssen. *THE INTERACTION OF OCEAN WAVES AND WIND*. Cambridge University Press, 2004.
- [47] P. A.E.M. Janssen. Progress in ocean wave forecasting. *Journal of Computational Physics*, 227:3572–3594, 2008.
- [48] P.A.E.M. Janssen. Quasilinear approximation for the spectrum of wind-generated water waves. *Journal of Fluid Mechanics*, 117:493–506, 1982.
- [49] P.A.E.M. Janssen. Wave induced stress and the drag of air flow over sea waves. *Journal of Physical Oceanography*, 19:745–754, 1989.
- [50] P.A.E.M. Janssen. Consequences of the effect of surface gravity waves on the mean air flow. *Int. Union of Theor. and Appl. Mech. (IUTAM)*, Sydney, Australia:193–198, 1991.
- [51] P.A.E.M. Janssen. Quasi-linear theory of wind-wave generation applied to wave forecasting. *Journal of Physical Oceanography*, 21:1631–1642, 1991.
- [52] P.A.E.M. Janssen. Nonlinear four-wave interactions and freak waves. *Journal of Physical Oceanography*, 33:863–884, 2003.

- [53] I.G. Jonsson. Wave boundary layers and friction factors. *Proc. 10th Int. Conf. Coastal Engineering*, ASCE:127–148, 1966.
- [54] K.K. Kahma and C.J. Calkoen. Reconciling discrepancies in the observed growth of wind-generated waves. *J. Phys. Oceanogr.*, 22:1389–1405, 1992.
- [55] J.M. Kaihatu and J.T. Kirby. Nonlinear transformation of waves in finite water depth. *Physics of Fluids*, 7:1903–1914, 1995.
- [56] G. Kallos, S. Nickovic, D. Jovic, O. Kakaliagou, A. Papadopoulos, N. Misirlis, L. Boukas, and N. Mimikou. The eta model operational forecasting system and its parallel implementation. *1st Workshop on Large-Scale Scientific Computations, Varna, Bulgaria*, 711, 1997.
- [57] G. Kallos, A. Papadopoulos, P. Katsafados, and S. Nickovic. Transatlantic saharan dust transport: Model simulation and results. *J. Geophys. Res.*, 111, 2006.
- [58] Kern E. Kenyon. Stokes drift for random gravity waves. *Jour. of Geophysical Research*, 74:6991–6994, 1969.
- [59] G.J. Komen, S. Hasselmann, and K. Hasselmann. On the existence of a fully developed wind-sea spectrum. *Journal of Physical Oceanography*, 14:1271–1285, 1984.
- [60] P. K. Kundu and I. M. Cohen. *Fluid Mechanics - 2nd Ed.* Academic Press, 1990.
- [61] Y. D. Lenn and T. K Chereskin. Observations of ekman currents in the southern ocean. *J. Phys. Oceanogr.*, 39:768–779, 2009.
- [62] Y. Liu, R. H. Weisberg, C. Hu, and L. Zheng. Trajectory forecast as a rapid response to the deepwater horizon oil spill, in monitoring and modeling the deepwater horizon oil spill: A record-breaking enterprise. *Geophys. Monogr. Ser.*, 195:153–165, 2011d.
- [63] Y. Liu and R.H. Weisberg. Evaluation of trajectory modeling in different dynamic regions using normalized cumulative lagrangian separation. *J. Geophys. Res.*, 116, 2011b.
- [64] W. Luo and J. Monbaliu. Effects of the bottom friction formulation on the energy-balance for gravity-waves in shallow-water. *Journal of Geophysical Research-Oceans*, 99(C9):18501–18511, 1994.

- [65] D. I. Mackay, I. A. Buistt, R. Mascarenhas, and S. Paterson. Oil spill processes and models. *Manuscript Report No. EE-8, Environment Canada, Ottawa, Ontario*, 1980a.
- [66] Gurvan Madec and the NEMO team. *Nemo Ocean Engine - version 3.4*. Technical report, 2012.
- [67] O.S. Madsen, Y.-K. Poon, and H.C. Graber. Spectral wave attenuation by bottom friction: Theory. *Proc. 21th Int. Conf. Coastal Engineering*, ASCE:492–504, 1988.
- [68] P.A. Madsen and O.R. Sørensen. Bound waves and triad interactions in shallow water. *Ocean Engineering*, 20, 4:359–388, 1993.
- [69] C. C. Mei, M. Stiassnie, and Dick K.-P. Yue. *Theory and Applications of Ocean Surface Waves - Part 1: Linear Aspects*. World Scientific Publishing Company Co. Pte. Ltd, 2005.
- [70] F. Mesinger. A blocking technique for representation of mountains in atmospheric models. *Riv. Meteorol. Aeronaut.*, 44, 1984.
- [71] F. Mesinger and A. Arakawa. *Numerical methods used in Atmospheric models*. GARP Publication Series No 17, 1976.
- [72] J. Miles. On the generation of surface waves by shear flows. *J. Fluid Mech.*, 3:185–204, 1957.
- [73] P. Oddo, M. Adani, N. Pinardi, C. Fratianni, M. Tonani, and D. Pettenuzzo. A nested atlantic-mediterranean sea general circulation model for operational forecasting. *Ocean Science*, 5(4):461, 2009.
- [74] P. Oddo, N. Pinardi, and M. Zavatarelli. A numerical study of the interannual variability of the adriatic sea. *Science of the Total Environment*, 353:39–56, 2005.
- [75] United States Environmental Protection Agency (EPA) Office of Emergency and Remedial Response (OSWE). *Understanding Oil Spills And Oil Spill Response*. United States Environmental Protection Agency (EPA), December 1999.
- [76] Delft University of Technology Environmental Fluid Mechanics Section. *SWAN – Scientific and Technical documentation*, version 40.91 edition, April 2012. available from <http://www.swan.tudelft.nl>.

- [77] WORLD METEOROLOGICAL ORGANIZATION. *Guide to Wave Analysis and Forecasting*. second edition, WMO-No. 702, 1998.
- [78] W.J. Pierson and L. Moskowitz. A proposed spectral form for fully developed wind seas based on the similarity theory of s.a. kitaigorodskii. *Journal of Geophysical Research*, 69, 24:5181–5190, 1964.
- [79] W. J. Plant. A relationship between wind stress and wave slope. *Journal of Geophysical Research: Oceans*, 87, Issue C3:1961–1967, 1982.
- [80] J. F. Price, R. A. Weller, and R. R. Schudlich. Wind-driven ocean currents and ekman transport. *Science*, 238:1534–1538, 1987.
- [81] J. M. Price, M. Reed, W. R. Howard, M. K. and Johnson, Z. G. Ji, C. F. Marshall, N. L. Guinasso, and G. B. Rainey. Preliminary assessment of an oil-spill trajectory model using satellite-tracked, oil-spill-simulating drifters. *Environ. Model. Softw.*, 21:258–270, 2006.
- [82] R. Proctor, A. J. Elliot, and R. A. Flather. Forecast and hindcast simulations of the braer oil spill. *Mar. Pollut. Bullet.*, 28(4):219–229, 1994.
- [83] A. Quarteroni and F. Saleri. *Calcolo Scientifico - Esercizi e problemi risolti con - MATLAB e Octave - 4a ed.* Springer-Verlag Italia, Milano, 2008.
- [84] A. Quarteroni, F. Saleri, and R. Sacco. *Matematica Numerica - 3a ed.* Springer-Verlag Italia, Milano, 2008.
- [85] C. Reed, M. Turner and A. Odulo. The role of wind and emulsification in modelling oil spill and surface drifter trajectories. *Spill. Sci. Technol. B.*, 1:143–157, 1994.
- [86] M. Reed, Å. Johansen, P. J. Brandvik, P. Daling, A. Lewis, R. Fiocco, D. Mackay, and R. Prentki. Oil spill modeling towards the close of the 20th century: Overview of the state of the art. *Spill Sci. Technol. Bull.*, 5:3–16, 1999.
- [87] M. R. Riazi and G. A. Al-Enezi. Modeling of the rate of oil spill disappearance from seawater for kuwaiti crude and its products. *Chemical Engineering Journal*, 73:161–172, 1999.
- [88] J. Rohrs, K. H. Christensen, L. R. Hole, G. Brostrom, M. Drivdal, and S Sundby. Observation-based evaluation of surface wave effects

- on currents and trajectory forecasts. *Ocean Dynamics*, 62,10-12:1519–1533, 2012.
- [89] B.G. Ruessink. Bound and free infragravity waves in the nearshore zone under breaking and non-breaking conditions. *Journal of Geophysical Research*, 103:795–805, 1998.
- [90] G. A. Sergy, C. C. GuÃlnette, E.H. Owens, R.C. Prince, and K. Lee. The svalbard shoreline oilspill field trials. *Proceedings of the 21st Arctic and Marine Oil Spill Program Technical Seminar*, AMOP, Edmonton, Alberta, Canada:873–889, 1998.
- [91] H.T. Shen and P.D. Yapa. Oil slick transport in rivers. *Journal of Hydraulic Engineering*, 114(5):529–543, 1988.
- [92] A. Sheremet, R.T. Guza, S. Elgar, and T.H.C. Herbers. Observations of nearshore infragravity waves. seaward and shoreward propagating components. *Journal of Geophysical Research*, 107 (C8):10, 2002.
- [93] W. Y. Shiu, M. Bobra, A. M. Bobra, A. Maijanen, L. Suntio, and D. Mackay. The water solubility of crude oils and petroleum products. *Oil and Chemical Pollution*, 7:57–84, 1990.
- [94] S. Simoncelli, N. Pinardi, P. Oddo, A. J. Mariano, G. Montanari, A. Rinaldi, and M. Deserti. Coastal rapid environmental assessment in the northern adriatic sea. *Dynamics of atmospheres and oceans*, 52(1):250–283, 2011.
- [95] R.L. Snyder, F.W. Dobson, J.A. Elliott, and R.B. Long. Array measurement of atmospheric pressure fluctuations above surface gravity waves. *Journal of Fluid Mechanics*, 102:1–59, 1981.
- [96] C. Spyrou, C. Mitsakou, G. Kallos, P. Louka, and G. Vlastou. An improved limited area model for describing the dust cycle in the atmosphere. *J. Geophys. Res.*, 115, 2010.
- [97] G. G. Stokes. On the theory of oscillatory waves. *Trans. Cambridge Phil. Soc.*, 8:441–455, 1847.
- [98] L. The WISE Group Cavaleri, J.-H.G.M. Alves, F. Ardhuin, A. Babanin, M. Banner, K. Belibassakis, M. Benoit, M. Donelan, J. Groeneweg, T.H.C. Herbers, P. Hwang, P.A.E.M. Janssen, T. Janssen, I.V. Lavrenov, R. Magne, J. Monbaliu, M. Onorato, V. Polnikov, D. Resio, W.E. Rogers, A. Sheremet, J. McKee Smith, H.L. Tolman, G. van

- Vledder, J. Wolf, and I. Young. Wave modelling - the state of the art. *Progress in Oceanography*, 75:603–674, 2007.
- [99] H.L Tolman. User manual and system documentation of wavewatch iii version 3.14. *NOAA/NWS/NCEP/MMAB Tech. Note*, 276:194 pp, 2009.
- [100] F. Trotta, S. Falchetti, M. Zavatarelli, and L. Giacomelli. Rapporto sulle caratteristiche del modello oceanografico rilocabile tessa con codice nemo. *Progetto Tessa, Attivita' 1.3*, Dipartimento di Fisica e Astronomia dell'Universita' di Bologna, Laboratorio SINCEM, via S.Alberto 163, 48100 Ravenna, 30-03-2013.
- [101] A.J. Van der Westhuysen. Advances in the spectral modelling of wind waves in the nearshore. *Ph.D. thesis*, Delft University of Technology:Department of Civil Engineering, The Netherlands, 2007.
- [102] A.J. Van der Westhuysen, M. Zijlema, and J. A. Battjes. Nonlinear saturation-based whitecapping dissipation in swan for deep and shallow water. *Coast. Engng.*, 54:151–170, 2007.
- [103] William W. S. Wei. *Time Series Analysis - Univariate and Multivariate Methods - Second Edition*. Pearson Education, Inc., 2006.
- [104] H. Xie, P. D. Yapa, and K. Nakata. Modeling emulsification after an oil spill in the sea. *Journal of Marine Systems, Elsevier*, 68:489–506, 2007.
- [105] Poojitha D. Y. Oil spill processes and modeling (state-of-the-art). *Proceedings of the 7th International Symposium on Environmental Hydraulics*, 2014.
- [106] L. Yan. An improved wind input source term for third generation ocean wave modelling. *Scientific report WR-No 87-8*, De Bilt, The Netherlands, 1987.
- [107] P.D. Yapa. Oil spill processes and model development. *Journal of Advanced Marine Technology, AMTEC, Tokyo, Japan*, pages 1–22, 1994.

Appendix A

Potential Velocity

In order to define the concept of *Potential Velocity* it is needed before to remind the *Line Integral* definition.

A.1 Line Integral

Let us consider an x - z plane and two points P_0 and P_1 and a vector $\vec{a}(x, z)$ defined over it as in figure A.1.

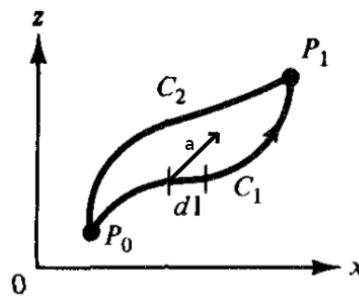


Fig. A.1: x - z plane, two points P_0 and P_1 , a vector \vec{a} and path C_1 and C_2 defined over it (modified from [26]).

Let's consider now the integral from P_0 to P_1 of the projection of the vector \vec{a} on the contour line C_1 denoting it as F :

$$F \equiv \int_{C_1(P_0, P_1)} \vec{a} \cdot \vec{dl} \quad (\text{A.1})$$

If the integral from P_0 to P_1 is calculated on the contour C_2 rather than on C_1 , a different value of F will be result.

But, if equation A.1 is rewritten as

$$F \equiv \int_{C_1(P_0, P_1)} dF \quad (\text{A.2})$$

where dF is the exact differential of F , then

$$F = F(P_1) - F(P_0) \quad (\text{A.3})$$

that is, F is only a function of the end points of the integration. Therefore, if we require that

$$\vec{a} \cdot \vec{dl} = dF \quad (\text{A.4})$$

independence of path is ensured.

For two dimensions, $\vec{a} = (a_x, a_z)$ and $\vec{dl} = dx\hat{i} + dz\hat{k}$ and

$$\vec{a} \cdot \vec{dl} = a_x dx + a_z dz \quad (\text{A.5})$$

while the total differential of F is

$$dF = \frac{\partial F}{\partial x} dx + \frac{\partial F}{\partial z} dz = \vec{\nabla} F \cdot \vec{dl} \quad (\text{A.6})$$

Hence, the condition of independence of path A.4 become

$$a_x dx + a_z dz = \frac{\partial F}{\partial x} dx + \frac{\partial F}{\partial z} dz \quad (\text{A.7})$$

which means

$$a_x = \frac{\partial F}{\partial x}, \quad a_z = \frac{\partial F}{\partial z}, \quad (\text{A.8})$$

or

$$\vec{a} = \vec{\nabla} F \quad (\text{A.9})$$

Then, it follows that

$$\frac{\partial a_x}{\partial x} - \frac{\partial a_z}{\partial z} = 0 \quad (\text{A.10})$$

or, in three dimensions,

$$\vec{\nabla} \times \vec{a} = 0 \quad (\text{A.11})$$

Therefore, in summary, independence of path of the line integral requires that the curl of \vec{a} must be zero.

A.2 Potential Velocity

Instead of the vector \vec{a} , let us consider the vector velocity \vec{u} given by

$$\vec{u}(\vec{x}, t) = u\hat{i} + v\hat{j} + w\hat{k} \quad (\text{A.12})$$

and let's define ϕ as the value of the line integral of \vec{u}

$$\phi = \oint_{C_1(P_0, P_1)} \vec{u} \cdot \vec{dl} \quad (\text{A.13})$$

The quantity $\vec{u} \cdot \vec{dl}$ is a measure of the fluid velocity in the direction of the contour at each point.

For the value of ϕ to be independent of path the terms in the integral must be an exact differential $d\phi$, which means that

$$u = \frac{\partial \phi}{\partial x} \quad (\text{A.14})$$

$$v = \frac{\partial \phi}{\partial y} \quad (\text{A.15})$$

$$z = \frac{\partial \phi}{\partial z} \quad (\text{A.16})$$

and therefore that the curl of \vec{u} (which is the physical quantity *vorticity* $\vec{\xi}$) must be zero, that is

$$\vec{\xi} = \vec{\nabla} \times \vec{u} = \left(\frac{\partial w}{\partial y} - \frac{\partial v}{\partial z} \right) \hat{i} + \left(\frac{\partial u}{\partial z} - \frac{\partial w}{\partial x} \right) \hat{j} + \left(\frac{\partial v}{\partial x} - \frac{\partial u}{\partial y} \right) \hat{k} = 0 \quad (\text{A.17})$$

If this condition apply, then it is possible to write

$$\vec{u} = \vec{\nabla} \phi \quad (\text{A.18})$$

that is, we can express the vector quantity \vec{u} by the gradient of the scalar function ϕ for a flow with no vorticity.

Appendix B

Kelvin Theorem

The Kelvin Circulation theorem states: ‘*In an inviscid, barotropic flow with conservative body forces, the Circulation around a closed curve moving with the fluid remains constant with time*’ [60].

Let us consider a moving closed curve C and the velocity vector \vec{u} defined over it as in figure A.1.

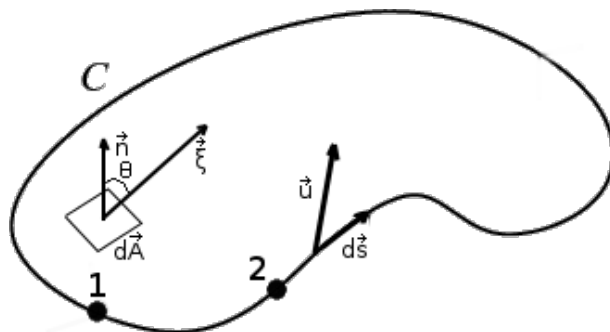


Fig. B.1: $x-z$ plane, two points P_0 and P_1 , a vector \vec{a} and path C_1 and C_2 defined over it (modified from [26]).

The physical quantity *Circulation* Γ for the close curve C is defined as

$$\Gamma = \oint_C \vec{u} \cdot d\vec{s} \quad (\text{B.1})$$

where $d\vec{s}$ is the infinitesimal vector displacement associated to each point composing C .

According to *Stokes' Theorem*, it is possible to write

$$\Gamma = \oint_C \vec{u} \cdot d\vec{s} = \int \int_A \vec{\nabla} \times \vec{u} \cdot d\vec{A} \quad (\text{B.2})$$

where A is the surface closed by the curve C (see figure B.1).

Then, it is possible to relate the *Circulation* Γ with the *vorticity* ξ (for the definition of vorticity see A) writing

$$\Gamma = \int \int_A \vec{\xi} \cdot d\vec{A} = \int \int_A |\vec{\xi}| \cos \theta |d\vec{A}| \quad (\text{B.3})$$

where θ is the angle between the vorticity vector $\vec{\xi}$ and the vector \vec{n} normal to the infinitesimal surface dA (see figure B.1).

The *vorticity* is therefore the *circulation* per unit area

$$[\xi] = \left[\frac{\Gamma}{A} \right] \quad (\text{B.4})$$

To derive the *Kelvin Theorem*, let us consider that from equation B.1 it is possible to write

$$\frac{D}{Dt}(d\Gamma) = \frac{D}{Dt}(\vec{u} \cdot d\vec{s}) \quad (\text{B.5})$$

$$= \frac{D\vec{u}}{Dt} \cdot d\vec{s} + \vec{u} \cdot \frac{D}{Dt}(d\vec{s}) \quad (\text{B.6})$$

$$= \frac{D\vec{u}}{Dt} \cdot d\vec{s} + \vec{u} \cdot d\vec{u} \quad (\text{B.7})$$

Now, integrating between the points 1 and 2 (see figure B.1), it will be

$$\frac{D}{Dt}(\Gamma_{1,2}) = \frac{D}{Dt} \int_1^2 \vec{u} \cdot d\vec{s} \quad (\text{B.8})$$

$$= \int_1^2 \frac{D\vec{u}}{Dt} \cdot d\vec{s} + \frac{\vec{u}^2}{2} \Big|_1^2 \quad (\text{B.9})$$

If the point 1 is equal to the point 2, i.e., $1 = 2$, then

$$\lim_{1 \rightarrow 2} \frac{D}{Dt}(\Gamma_{1,2}) = \oint \frac{D\vec{u}}{Dt} \cdot d\vec{s} \quad (\text{B.10})$$

Consider now a not rotating, inviscid (i.e., $\vec{\nabla} \cdot \vec{u} = 0$) fluid with constant density ρ_0 . Then, it is possible to write

$$\frac{D\vec{u}}{Dt} = -\vec{\nabla} \left(\frac{p}{\rho_0} + \varphi \right) \quad (\text{B.11})$$

where $\vec{\nabla}\varphi = g$.

Substituting equation B.11 into B.10 and integrating between the points 1 and 2 with the points $1 = 2$ we obtain

$$\lim_{1 \rightarrow 2} \frac{D}{Dt}(\Gamma_{1,2}) = 0 \quad (\text{B.12})$$

which means that the circulation Γ is constant in time if calculated around a closed curve moving with the fluid.

Appendix C

Stochastic Processes

This brief description of the *Stochastic Processes* theory is carried out following [103].

A *Stochastic Process* is a family of time indexed random variables $Z(s, t)$, where s belongs to a *sample-space* and t belongs to an index set.

For a fixed t , $Z(s, t)$ is a *random variable*.

For a given s , $Z(s, t)$, as a function of t , is called a *sample function* or *realization*.

The population that consists of all the possible realizations is called the *ensemble* in stochastic processes and time series analysis.

Thus, a *time series* is a realization or sample function from a certain stochastic process.

With proper understanding that a stochastic process $Z(s, t)$ is a set of time indexed random variables defined on a sample space, the variable s is usually suppressed and it is simply written $Z(s, t)$ as $Z(t)$ or Z_t , just as random variables are denoted by X rather than by $X(s)$.

Stationary Stochastic Processes: Consider a finite set of random variables $\{Z_{t_1}, Z_{t_2}, \dots, Z_{t_n}\}$ from a stochastic process $\{Z(t) : t = 0, 1, 2, \dots\}$. The

n -dimensional probability distribution function associated to the stochastic process is defined by

$$F_{Z_{t_1}, \dots, Z_{t_n}}(x_1, \dots, x_n) = Pr\{s : Z_{t_1} \leq x_1, \dots, Z_{t_n} \leq x_n\} \quad (\text{C.1})$$

A process is said to be *first-order Stationary* in distribution if its one-dimensional distribution function is time invariant, i.e., if

$$F_{Z_{t_1}}(x_1) = F_{Z_{t_1+k}}(x_1) \quad (\text{C.2})$$

for any integers t_1, k and $t_1 + k$. In general a process is said to be *n th-order Stationary* in distribution if

$$F_{Z_{t_1}, \dots, Z_{t_n}}(x_1, \dots, x_n) = F_{Z_{t_1+k}, \dots, Z_{t_n+k}}(x_1, \dots, x_n) \quad (\text{C.3})$$

for any n -tuple (t_1, \dots, t_n) , and k of integers.

A process is said to be *Strictly Stationary* if equation C.3 is true for any n .

The *mean function* of the process $\{Z(t) : t = 0, 1, 2, \dots\}$ is defined as

$$\mu_t = E(Z_t) \quad (\text{C.4})$$

where the subscript \bullet_t means that the mean is related to the generic Z_t random variable. Similarly, the *variance function* of the process is

$$\sigma_t^2 = E(Z_t - \mu_t)^2 \quad (\text{C.5})$$

and the *covariance* and *correlation function* are, respectively,

$$\gamma(t_1, t_2) = E(Z_{t_1} - \mu_{t_1})(Z_{t_2} - \mu_{t_2}) \quad (\text{C.6})$$

$$\rho(t_1, t_2) = \frac{\gamma(t_1, t_2)}{\sqrt{\sigma_{t_1}^2} \sqrt{\sigma_{t_2}^2}} \quad (\text{C.7})$$

For a strictly stationary process, since the distribution function is the same for all t , the mean function $\mu_t = \mu$ and the variance function $\sigma_t^2 = \sigma^2$ are a

constant, provided that $E(|Z_T|) < \infty$ and $E(|Z_t^2|) < \infty$. Furthermore, since $F_{Z_{t_1}, Z_{t_2}} = F_{Z_{t_1+k}, Z_{t_2+k}}$ for any integers t and k , we have, letting $t_1 = t - k$ and $t_2 = t$,

$$\gamma(t_1, t_2) = \gamma(t - k, t) = \gamma(t, t + k) \quad (\text{C.8})$$

and

$$\rho(t_1, t_2) = \rho(t - k, t) = \rho(t, t + k) \quad (\text{C.9})$$

Therefore, for a strictly stationary process with the first two moments finite, the covariance and the correlation between Z_t and Z_{t+k} depend only on the time lag k .

The Strictly Stationarity is a strong condition, that usually does not apply to real processes. Thus, in time series analysis, a weaker sense of stationarity in terms of the moments of the process is used.

A process is said to be n th-order *Weakly Stationary* if all its joint moments up to order n exist and are time invariant. Sometimes, the terms stationary in *the wide sense* or *Covariance Stationary* are also used to describe a second-order weakly stationary process, which has constant mean and variance, with the covariance and the correlation being functions of the time difference alone.

Therefore, the stationarity of a process greatly simplifies the description, since only the statistical characteristics for one moment in time are required (including the relationships with the random variables at all time intervals).

As we have seen, for a stationary process $\{Z_t\}$ the mean $E(Z_t) = \mu$ and variance $Var(Z_t) = E(Z_t - \mu)^2 = \sigma^2$ are constant and covariances $Cov(Z_t, Z_s)$ are functions only of the time difference $k = |t - s|$. Hence, it is possible to write

$$\gamma_k = Cov(z_t, Z_t + k) = E(Z_t - \mu)(Z_{t+k} - \mu) \quad (\text{C.10})$$

and the correlation between Z_t and Z_{t+k} as

$$\rho_k = \frac{Cov(Z_t, Z_{t+k})}{\sqrt{Var(Z_t)}\sqrt{Var(Z_{t+k})}} = \frac{\gamma_k}{\gamma_0} \quad (\text{C.11})$$

where $Var(Z_t) = Var(Z_{t+k}) = \gamma_0$. As functions of k , γ_k is called *autocovariance* function and ρ_k is called the *autocorrelation* function in time series analysis because they represent the covariance and the correlation between Z_t and Z_{t+k} from the same process, separated only by k time lags. It can be showed that the autocovariance function and the the autocorrelation function of stationary processes have the following properties:

1. $\gamma_0 = Var(Z_t)$; $\rho_0 = 1$.
2. $|\gamma_k| \leq \gamma_0$; $|\rho_k| \leq 1$.
3. $\gamma_k = \gamma_{-k}$; $\rho_k = \rho_{-k}$.

Gaussian Stochastic Processes: If all (joint) probability density functions of a process (stationary or not) are Gaussian, the process is called a *Gaussian process*.

A stationary, Gaussian process is even simpler to describe: only the mean and the covariances for one moment in time are required (because they are identical at all other times). The covariance is only a function of the time interval k , thus

$$\gamma(t_1, t_2) = \gamma(t - k, t) = \gamma(t, t + k) = \gamma_k \tag{C.12}$$

Ergodic Stochastic Processes: A stationary time series is characterized by its means μ , variance σ^2 and autocorrelation ρ_k . The exact values of these parameters can be calculated if the ensemble of all the possible realizations is known. Otherwise, they can be estimated if multiple independent realizations are available. In most application, time series constitute only a single realization, which makes it impossible to calculate the ensemble average.

With only a single realization, a natural estimator for the mean $\mu = E(Z_t)$ of a stationary process is the sample mean

$$\bar{Z} = \frac{1}{n} \sum_{t=1}^n Z_t \tag{C.13}$$

which is the time average of n observations. If Z_t is a continuous random variable, it follows that

$$\bar{Z} = \frac{1}{T} \int_{t_0=0}^T Z_t \quad (\text{C.14})$$

where T is the duration of the process.

\bar{Z} is an *unbiased* estimator for μ . Indeed

$$E(\bar{Z}) = \frac{1}{n} \sum_{t=1}^n E(Z_t) = \frac{1}{n} \cdot n\mu = \mu \quad (\text{C.15})$$

A stationary process is said to be *Ergodic* for the mean if it is true that

$$\lim_{n \rightarrow \infty} \frac{1}{n} \sum_{t=1}^n Z_t = \mu \quad (\text{C.16})$$

or, for continuous random variables,

$$\lim_{n \rightarrow \infty} \frac{1}{T} \int_{t_0=0}^T Z_t = \mu \quad (\text{C.17})$$